

2012 NSF/REU

**RESEARCH EXPERIENCE
FOR UNDERGRADUATES
IN PHYSICS**



**UNIVERSITY OF NOTRE DAME
STUDENT RESEARCH PAPERS**

VOLUME 23



**REU DIRECTOR
UMESH GARG, PH.D.**

REU Student Research Papers – Summer 2012
University of Notre Dame – Department of Physics

Student	Research Title	Page No.
Amy Applegate Georgian Court College	Determining the Orbital Period of the Cataclysmic Variable CSS1204 Using Data from the Vatican Advanced Technology Telescope	1
Vincent Burns University of Notre Dame	Analysis of High Ions in Optically Thick Quasar Absorbers	9
Rachael Creager University of Notre Dame	Analysis of a Potential Tracking Algorithm for the SLHC Upgrade	19
Erika Escobar UCLA	Using the Atmospheric Pressure Plasma Jet to Assess the Effects of Plasma on DNA Molecules	33
Joanna Flores University of California Santa Cruz	Using the Theory of Multiple Intelligences to Understand Guided Inquiry	43
Cathleen Fry Tennessee Tech University	Extracting Optical Model Parameters for $^{116}\text{Sn}(d,d')$ at the 200 MeV	53
Martin Gostisha University of Wisconsin-Whitewater	Simulations of a Galaxy Model to Probe Outflow Interactions in a Filamentary Structure	61
Jordan Hernandez Tarleton State University	Using a Theoretical Model for the Energy of Ice VI and VII	71
Cedric Hill Morehouse College	Project GRAND	81
Joseph Hlevyack Loyola University Chicago	Small-Angle Neutron Scattering (SANS) Studies of Superconducting UPT_3 's Vortice Lattice	91
Tyler Knowles Ripon College	Using the Theory of Multiple Intelligences to Understand Guided Inquiry	43
Katrina Magno University of Notre Dame	Study of Cataclysmic Variable B7 in NGC 6791: From the Ground and from Space	101
Luis Morales Indiana University South Bend	St. George Recoil Mass Separator Time of Flight and Position Sensitive Detector	111

Student	Research Title	Page No.
Michael Pope Arizona State University	Identification of Naturally Occurring Radioactive Material in Sand	121
Terri Poxon-Pearson American University	Exploring the Neutron Channel of Carbon Burning at Stellar Energies	131
Mike Robbe University of Notre Dame	ASIC Data Acquisition System; Implementation of HINP16C on SAND	141
Lindsay Sonderhouse Reed College	Magnetic Properties of GaAs/Fe Radial Hetrostructured Nanowires	151
Christopher Steiner University of Notre Dame	Constructing a Scanning Tunneling Microscope for the Study of Superconductivity	161
Annie Stephenson University of Notre Dame	Galaxy outflow and Filamentary Interaction	171
Michael Swift Rice University	Analysis of a Potential Tracking Algorithm for the SLHC Upgrade	19

**Determining the Orbital Period of the Cataclysmic
Variable CSS1204 Using Data from the Vatican
Advanced Technology Telescope**

Amy Applegate

2012 NSF/REU Program
Physics Department, University of Notre Dame

Advisor: Dr. Peter Garnavich

Abstract: *Using time-resolved photometry from three nights of observing at the Vatican Advanced Technology Telescope (VATT), we obtained light curves of the cataclysmic variable (CV) CSS1204 (RA.11:11:26.87 Dec.+57:12:38.9(J2000)). From these observations, we calculated the power spectrum of CSS1204 and determined the orbital period of the binary. We determined the orbital period for CSS1204 to be 0.8876 hours. Using the orbital period along with the pre-determined superhump period ($p=0.9370$ h), we can infer the mass ratio of the primary and secondary stars in this CV. We calculated a mass ratio of 0.458 using the fractional superhump excess for the minimum superhump period (P_{SH}) which was used in Kato et al. 2009. CSS1204 is unusual in that its period is approximately 25 minutes below the period minimum for hydrogen-rich CVs. The research outlined in this paper will be included in a forthcoming journal article about this star.*

Keywords: *CSS1204, cataclysmic variable, orbital period, VATT*

Introduction

“Cataclysmic variables (CVs) are compact binary systems in which the surface gas of a secondary star overflows and is accreted by a more massive white dwarf” (qtd. in Uemura, et al 2001). A disk consisting of infalling matter forms around the primary star due to the angular momentum that needs to be conserved. In the accretion disk, viscosity occurs and as a result, the disk material loses its angular momentum and eventually is accreted on the white dwarf star. When the density and temperature of the hydrogen layer in the accretion disk around the white dwarf rises to a considerable amount, an event known as a cataclysmic outburst (or superoutburst) will take place. During outbursts and superoutbursts, the system becomes much brighter. When observing a CV during a superoutburst, an additional modulation will appear in the light curve of the star, called a superhump. This event is caused by the precession of the accretion disc and it can occur approximately every 20-300 days depending on the CV itself. The orbital periods of CVs are typically only several hours long with an observed period minimum close to 78 minutes. Very few CVs have orbital periods between 2-3 hours. This duration of time is known as the period gap.

CSS120422:111127+571239 (more commonly known as SBS 1108+574) is classified as a CV like the one mentioned above. It was first observed by the Catalina Real-Time Transient Survey (CRTS) during an outburst. As a result of later observations from the Japanese-run network, VSNET and Peter Garnavich, the binary star in CSS1204 was specifically classified as a SU UMa star. Garnavich, et al (2012) reported spectra showing strong Hydrogen emission along with the expected abundance of Helium emission present. Before this discovery, it was assumed that CSS1204 was a AM CVn star which are ultrashort-period CVs with no amounts of hydrogen in their spectra. “Stars which show both superoutbursts and superhumps are referred to as SU UMa stars” (Hellier, 2001). “Superhump oscillations with a period of 0.93 hours” were observed from CSS1204 (Garnavich, et al 2012). Superhumps are caused by the gravitational interaction between the disk and the secondary star. When the disk becomes asymmetric and precesses, it causes fluctuations in brightness which usually last slightly longer than the orbital period of the CV.

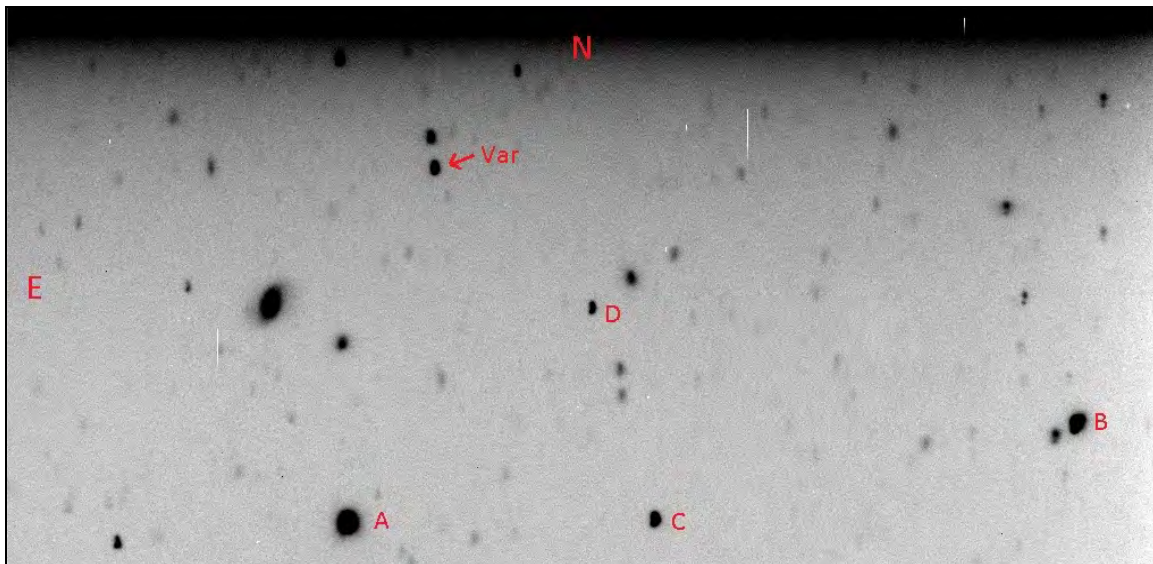


Figure 1. A summed “superCSS1204” FITS image showing the variable star and the four nearby comparison stars. Star A is the comparison star used in the aperture photometry. Var is the CV CSS1204.

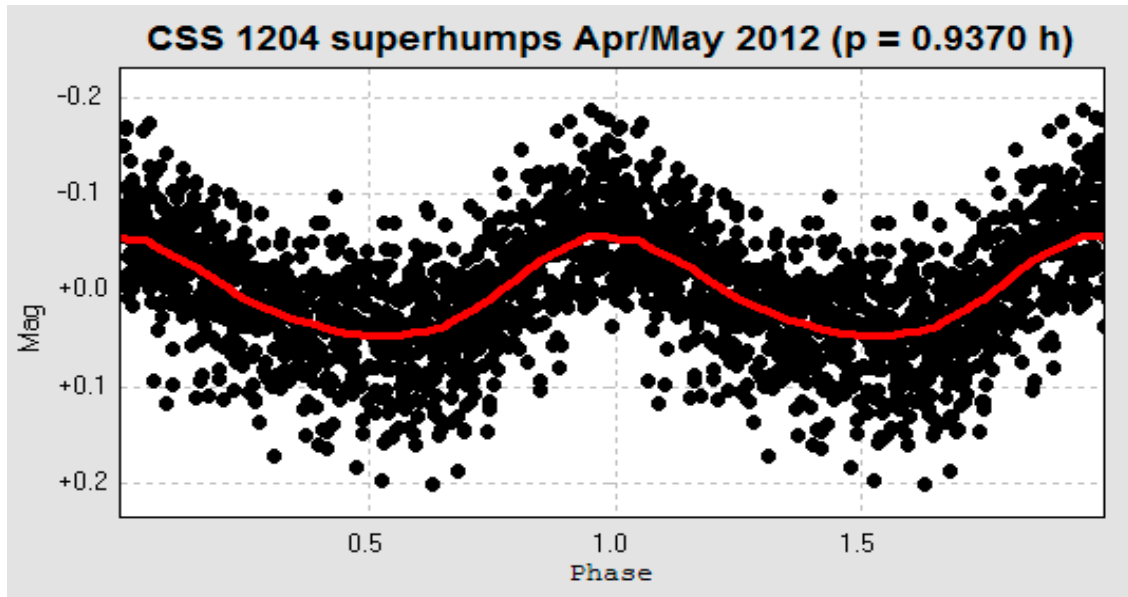


Figure 2. This image¹ shows the Magnitude vs. Phase plot for the superhump period of CSS1204.

The purpose of this paper is to describe the process and results from analyzing the power spectrum of CSS1204, in order to determine the orbital period. The superhump period for the CV CSS1204 is already known, but an orbital period in the quiescent state has yet to be determined. Knowing the orbital period for CSS1204 along with the pre-determined superhump period will allow us to derive the mass ratio of the primary white dwarf to the secondary star. If our orbital period is close to the superhump period determined by VSNET, then there will be a large mass ratio between the two components in the CV, but if our period is much shorter than the superhump period, the mass ratio of the primary and secondary stars will be small. The mass ratio of this CV contains clues as to the nature of the secondary “donor” star. Comparing the superhump period to the true orbital period of CSS1204 is the only method that will allow us to discover these clues.

¹ This plot of the superhump period for CSS1204 was created by Univ. of Notre Dame School of Law student, Colin Littlefield.

Materials and Methods

Situated atop Mt. Graham in Safford, Arizona, the VATT is operated by the Vatican Observatory in partnership with the University of Arizona. Its primary mirror consists of a 1.83-m f/1.0 mirror. The location of the VATT atop Mt. Graham provides one of the best areas in the U.S. for seeing even without the use of adaptive optics. Observations of CSS1204 were recorded through the Blue (FWHM-94nm) and Red (FWHM-138nm) filters within the visible light spectrum. The CCD (Charge Coupled Device) used in the VATT is a STA0500A back illuminated 4k CCD. On the third night of observation, a thunderstorm passed over Mt. Graham creating bad seeing so as a result, CSS1204 was not observed.

Image Reduction and Analysis Facility (IRAF) is a software system that we utilized to prepare the images taken from the VATT. To extract chip [2] data from the original mosaic files, we used the *imcopy* package for each night's pixel data. Once the chip [2] data was extracted from the original mosaic files, bias images (exposures taken when the camera's shutter is left shut) were combined using the *imcombine* package. Bias images are important in the image reduction process because they eliminate readout noise from exposure to exposure and allows for better measurements of the star photometry. This created a "supersmallbias" which we subtracted from the CSS1204 FITS files using the *imarith* package.

Using the IRAF package, *qphot*, we performed aperture photometry on all of the biased CSS1204 FITS images. Photometry is the use of an electronic detector to measure the amount of flux from an object in a given region of the spectrum. The atmosphere absorbs and scatters some light from the target star, the flux of the target star will change depending on the amount of atmosphere along the line-of-sight from Earth, so to lessen the impact the atmosphere has on the

flux of the target star, we need to compare it to a few nearby stars. We wanted to ensure that the variation in magnitude we were seeing was strictly from the target star and not due to the variation in seeing conditions from night to night, so we subtracted the magnitude of the brightest comparison star (Comparison star A) with the most constant flux from the magnitude of our target star. To do this, we configured the parameters in *qphot* accordingly, created MAG files from each star, subtracted the Comp 1 star MAG file from the variable MAG file, and then subtracted the mean of the magnitudes as well. It should be known that the last two FITS images from night 2 were not included in the corresponding MAG files because during the time that these exposures were being taken, a glitch occurred in the telescope causing it to change coordinates.

Interactive Data Language (IDL) is a programming language used to analyze large quantities of data. Using this program language, we used the program *power.pro* created by Peter Garnavich and created the program *n1power.pro* to run in conjunction. The program *power.pro* calculated the power spectrum of the star with a low frequency of 0.1 cycles/hour and a high frequency of 10 cycles/hour out of 10,000.0 frequencies. We compiled *n1power.pro* to plot the magnitude difference of CSS1204 vs. the phase (cycle). To reduce the noise present in the plot, we applied a 3-pixel *boxcar smooth* function to the data.

Data

Figure 3 is a light curve which shows the relationship between the relative magnitude and the phase of CSS1204. The phase is measured in cycles or time (hours) per period. As the stars orbit their center of mass, the observed flux from the system will change as some features come into

view and others become hidden. Since the orbital period is stable, these changes in brightness should repeat themselves during every orbit.

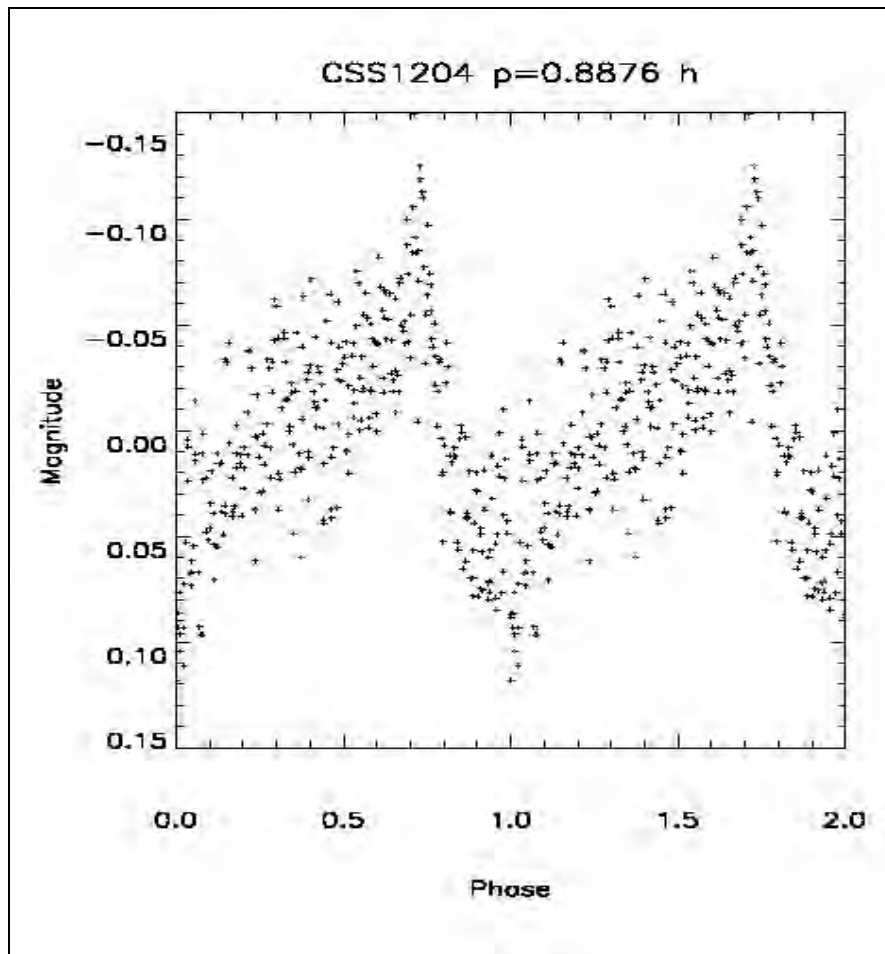


Figure 3. This image shows the Magnitude vs. Phase plot we created for CSS1204. Two phases (cycles) are shown for clarity.

Results and Analysis

After three nights of observing the CV CSS1204 at the VATT, we determined that the orbital period was 0.8876 hours in duration. Looking at this value as well as the superhump period (0.9370 h) one can see that they are close in comparison. To determine the mass ratio of the

components in CSS1204, we used the fractional superhump excess for the minimum superhump period (P_{SH}) which was used in Kato et al. 2009

$$\varepsilon = 0.25q^2 + 0.16q \quad (1),$$

where q represents the mass ratio of the secondary star to the primary star and $\varepsilon = \left(\frac{P_{SH}}{P_O} \right) - 1$; P_{SH} represents the superhump period, and P_O represents the orbital period. The calculated mass ratio was 0.25175 or 25.2%. This makes the empirical assumption that the secondary star is approximately $1/4^{\text{th}}$ the size of the primary star.

Conclusion

Using time-resolved photometry from three nights of observing at the Vatican Advanced Technology Telescope, we calculated the true orbital period and the mass ratio of the cataclysmic variable, CSS120422:111127+571239. From these values, one can see that the components in this CV are distanced extremely close to each other-even closer to each other than the distance of Mercury and our Sun. The research outlined in this paper will be included in a forthcoming article about this star.

References

- Garnavich, P., et al 2012, The Astronomer's Telegram
- Hellier, C. 2001, Cataclysmic Variable Stars: How and Why they Vary. Praxis Publishing. Chichester, UK.
- Kato, T., et al 2009, arXiv:0905.1757v2.
- Uemura, M., et al 2001, Astronomical Society of Japan, 1

Analysis of High Ions in Optically Thick Quasar Absorbers

Vincent Burns

2012 NSF/REU Program
Physics Department, University of Notre Dame

Advisor: Professor Nicolas Lehner

Abstract

Optically thick absorbers, a class of extragalactic gas clouds that includes damped Ly α absorbers and Lyman limit systems and appears in the absorption spectra of quasars, provide insight into the interactions of galaxies with the nearby intergalactic medium. The ionized metal species of C IV, Si IV, and O VI are of particular interest due to their ability to probe a wide temperature range of ionized gas within the galactic halo. Using QSO spectra from the High Resolution Echelle Spectrometer on the Keck 10 m telescope, a comprehensive search was undertaken for optically thick absorbers to supplement previous surveys, resulting in the largest sample of high ions in high redshift absorbers yet constructed. The velocity ranges and total column densities of these ions were measured and tabulated and a grading system implemented for OVI absorption. Preliminary analysis of the survey indicates a larger dispersion of total column densities and column density ratios, a larger average column density ratio of C IV to Si IV, and a smaller average column density ratio of C IV to O VI for high redshift absorbers than previously found in the Milky Way. Additionally, the presence of absorbers with O VI column density greater than 10^{15} cm^{-2} suggests the presence of high redshift starburst galaxies, i.e. galaxies with over ten times more active star formation than the Milky Way.

Introduction

Galaxies are found to exhibit star formation throughout their evolution, requiring a constant influx of gas. The source of this influx is the intergalactic medium (IGM), a reservoir of gas encompassing the space between galaxies. The relationship between galaxies and the IGM is complex. Supernovae and the creation of new massive stars blow gas out of the galaxy into the IGM, enriching it with metals. Simultaneously, this enriched material is recycled back into the galaxy, fueling further star-formation. However, the outflow and accretion of gas and

their feedback effects on star formation are not well understood, especially at high redshifts of $1.5 < z < 4$, representing a period of nine to twelve billion years ago when star formation rates in galaxies were about 10 to 100 times greater than in the present universe.

One method of studying the Galaxy-IGM interface at high redshifts (high- z) is analyzing absorption spectra of background quasars created by optically thick absorbers. These absorbers are characterized by the large optical depth of their Ly α absorption line and are further categorized by their neutral hydrogen column density (N_{HI}) into two groups: damped Ly α absorbers (DLAs), which have $\log(N_{\text{HI}}) \geq 20.3$, and Lyman limit systems (LLSs) with $16 < \log(N_{\text{HI}}) < 20.3$. DLAs and LLSs exhibit a multiphase structure, containing overlapping neutral, weakly ionized, and strongly ionized gas, and have been found in previous studies to be associated with galactic (and, in the case of DLAs, proto-galactic) halos (Lehner et al. 2009).

While the neutral component of DLAs and LLSs has been studied extensively, the properties of their ionized component have not. The ionized gas could be especially important for understanding galaxy-IGM interactions because the missing metals at high- z are likely in this gas phase (Fox et al. 2007a,b), and because extent of different metal ions in the absorber have been shown to be important to constrain the behavior of galactic outflow, accretion, and feedback (Fox et al. 2007a,c, 2009, Lehner et al. 2008). Therefore, highly ionized metals or high ions are the best way to probe ionized gas in DLAs and LLSs. The range of ionization energies of high ions makes them effective indicators of the temperature and ionization mechanism of the gas, important properties for understanding the behavior of DLAs and LLSs. The high ions chosen for study in this survey are Si IV, C IV, and O VI. Si IV and C IV are ubiquitous in DLAs and LLS and are generally uncontaminated because they are not in the Ly α forest, a term used to describe the Ly α lines that contaminate the smaller wavelengths of spectra. O VI is in

the Ly α forest, making it more difficult to detect, but is of particular interest because its high ionization potential requires the mechanism of collisional ionization for its production (Si IV and C IV can both be photoionized) and its abundance can be used to calculate the amount of ionized hydrogen (H II) in the DLA or LLS because, unlike H I, H II cannot be directly observed.

The following study is a preliminary step in a larger attempt to comprehensively survey and characterize optically thick absorbers in order to better understand the behavior of gas in the IGM-galaxy interface at high redshift. Absorbers were systematically searched for in QSO spectra, the basic properties of the high ions Si IV, C IV, and O VI in these absorbers were measured, and basic analysis was conducted on the sample as a whole.

Data Sample, Reduction, and Analysis

The spectra used in this study come from observations made by the High Resolution Echelle Spectrometer (HIRES) at the Keck I 10-m Telescope, and retrieved from the Keck Observatory Archive at the NASA Exoplanet Science Institute. The high spectral resolutions (6-8 km/s) and signal-to-noise ($S/N > 20$ with many $S/N > 50$) of this sample mean highly reliable parameters can be estimated. The Keck/HIRES spectra cover wavelength ranges from 3000 to 10000 Å, but not continuously. At the redshifts of interest, the high ion doublet absorption lines of Si IV, C IV, and O VI found in the rich, ultraviolet section of the spectrum are shifted into the Keck/HIRES's wavelength range, allowing for consistent coverage (see Table 1). Due to the high- z of the background QSO, contamination is a problem for a substantial part of the sample, since gas clouds along the line of sight to the QSO all leave absorption lines in the spectrum. This is especially a problem for detecting O VI, which is found within the Ly α forest.

The database includes 100 spectra, of which 71 were analyzed for this study, resulting in the identification of 211 high redshift absorbers, the largest such compilation of its kind. The

Table 1: High ion sample sizes

<i>Ion</i>	λ (\AA)	<i>I. P.</i> (eV)	z_{ground}	<i>Sample Size</i>	<i>Samples with Errors</i>
Si IV	1393.8, 1402.8	33.5 – 45.1	1.2	204(105)	166(87)
C IV	1548.2, 1550.8	47.9 – 73.5	0.9	197(100)	168(82)
O VI	1031.9, 1037.6	113.9 – 138.1	1.9	145(62)	113(46)

Notes: I.P is the ionization potential range for the ion. z_{ground} is the redshift above which lines can be seen from the ground at $>3000 \text{\AA}$. Samples with errors excludes ions for which a lower or upper limit were estimated due to saturation or a non-detection respectively. Numbers in parentheses are the subset identified by the author.

sample size of each ion is summarized in Table 1. The identification of absorbers within the quasar spectra was conducted using normalized spectra formatted by Professor John O’Meara. Professor O’Meara identified 106 of the absorbers by searching for DLAs and super LLSs ($\log[\text{N}_{\text{HI}}] > 19$). This sample was supplemented by the author, who identified 105 absorbers by searching for strong Ly α absorption lines, the signature of strong H I absorbers such as a DLA or LLS. These absorbers were confirmed by over-plotting the high ion doublets to check for similar velocity profiles. In several cases, multiple DLAs or LLSs were identified within each spectrum. Despite the different sampling methods, no noticeable difference exists between the two samples.

For each absorption line, an IDL program was used to measure the parameters of velocity range (the velocities of ions within the absorber), total column density (the number of atoms of an ion per square centimeter within the absorber), and equivalent width (a measure of the strength of the absorption line). These values were measured via the apparent optical depth (AOD) method described by Savage and Sembach (Lehner et al. 2010). The AOD method requires fitting the continuum with a Legendre polynomial near the absorption lines of interest. In this study, a low degree polynomial (usually <3) was used because the spectra were already normalized over the entire observed wavelength range. This fit is critical for obtaining accurate measurements in the AOD method since changes in the continuum fit can substantially change the apparent optical depth (Lehner et al. 2010). Generally, a fit was found within 400 km/s of

the absorption line, but contamination sometimes required a larger velocity range to establish the continuum, possibly introducing non-negligible error into the measurements.

Following the fit of the continuum, the velocity range was identified by the minimum and maximum velocities to which the absorption line extended for each ion (the same velocity range was used for both doublets of each ion, but could be different among the ions). (To plot the spectra's intensity as a function of velocity, the program set a zero point at the wavelength of the desired ion). To measure the total column density, the apparent column densities per unit velocity $N_a(v)$ of the absorption lines was measured via $N_a(v) = 3.768 \times 10^{14} \ln[1/F_{\text{obs}}(v)] / (f \cdot \lambda)$ $\text{cm}^{-2} (\text{km/s})^{-1}$, where $F_{\text{obs}}(v)$ is the normalized flux of the absorption line as a function of velocity and f is the oscillator strength of absorption. Total column densities (N) were then obtained by integrating $N_a(v)$ over the velocity range specified. In cases of saturation where $F_{\text{obs}}(v)$ reaches zero, a lower limit value for N was measured by the program, and in the absence of a detection, a 3σ upper limit was measured for N . Finally, the equivalent width of the line was measured by integrating the area of the absorption line over the velocity range.

These results were tabulated in files, which were then read by a program written by the author. The program recorded the velocity ranges and combined the total column density measurements for each ion to calculate a final value for N using the following methodology:

- If N_{strong} and N_{weak} agreed, their average was calculated.
- If either N_{weak} or N_{strong} was an upper or lower limit or contained contamination, the other line's column density was used exclusively.
- If both N_{weak} and N_{strong} were either upper or lower limits, the strong or weak line's column density was used respectively.

- In the case of two contaminated lines, the less contaminated line's column density was used and was appropriately flagged.

Subsequently, the total column density ratios between C IV and Si IV and C IV and O VI were calculated, ratios that could potentially trace the ionization mechanisms at the galaxy-IGM interface. No work has yet been done with the equivalent width measurements. In addition to the measurements, a grade was recorded for the quality of the O VI absorption lines on a scale of A – F, such that absorbers with uncontaminated lines and excellent agreement received an A.

Preliminary Results

The major aim of this survey was accumulating and organizing data in such a manner as to facilitate future analysis. Nevertheless, some preliminary efforts can be made to characterize the properties of the DLAs and LLSs, especially in comparing their properties to those measured in the Milky Way. The subsequent data for the Milky Way is taken from the sample of 29 extragalactic lines of sight found in Savage and Wakker 2009, a sample which excludes limits.

A first step is to compare the distribution of the total column densities of the high ions, the logarithms of which are plotted for the high- z absorbers in Figure 1. The distribution of all of the ions is logarithmic-normal and total column density increases as ionization energy increases, a trend that is mirrored in the Milky Way data. The most substantial difference between the two datasets is the size of the standard deviation for the DLAs and LLSs, which is double for C IV and O VI and almost triple for Si IV as compared to the Milky Way. Though the high- z sample is almost a degree of magnitude greater than the Milky Way sample, the difference is great enough to suggest a larger overall variation in column densities at high- z . Additionally, N_{mean} is different in all three ions; Si IV's mean is 0.30 less, C IV's mean is 0.24 less, and O VI's mean is 0.09 greater for DLAs and LLSs than for the Milky Way. Since O VI is

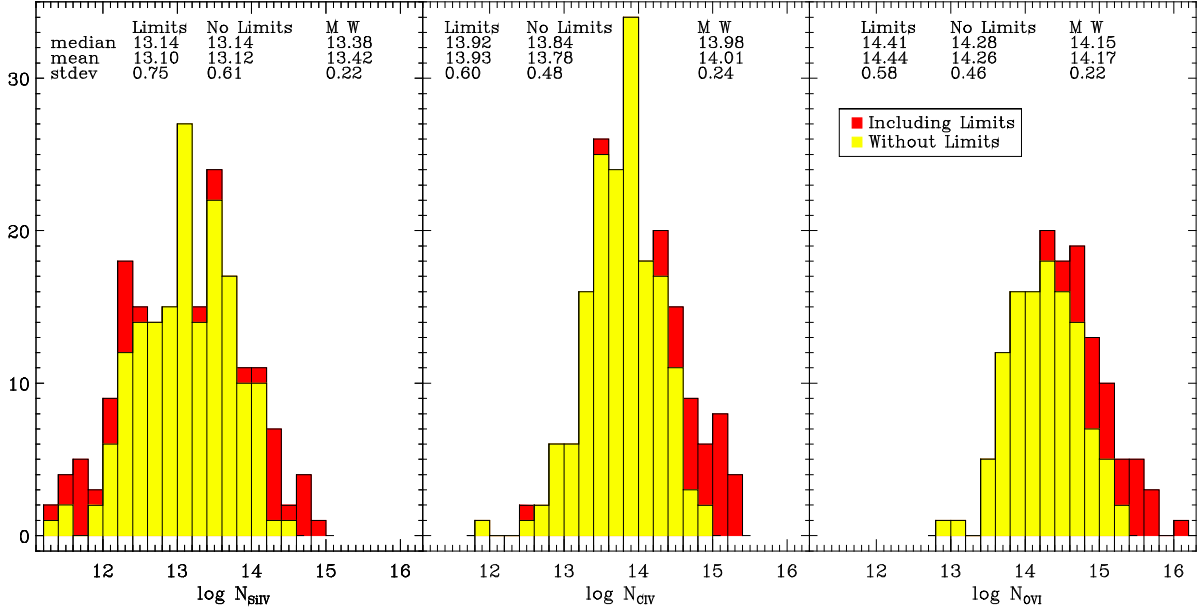


Figure 1: Distribution of the logarithms of Si IV, C IV, and O VI total column densities in DLAs and LLSs at high-z. The red data are the entire sample, while the yellow data are the sample excluding limits. Statistics for the dataset, the subset without limits, and the Milky Way (taken from Savage and Wakker 2009) are drawn at the top of the plots.

believed to trace hot ($\sim 10^5 - 10^6$ K), gas while Si IV and C IV are believed generally to trace warm ($\sim 10^4$ K) gas, more hot gas appears to be present in high-z galaxies and their halos. This is further supported if one considers that for many absorbers, $\log[N_{\text{O VI}}] > 14.8$. These high O VI column densities are unseen in the Milky Way, but can be observed in local starburst galaxies at least up to $\log[N_{\text{O VI}}] \sim 15$. The presence of such large $N_{\text{O VI}}$ values indicates a large amount of hot gas, which is likely produced by strong feedback within the protogalaxies. Therefore, protogalaxies can be far more active than local galaxies, with star formation rates that are over 10 times greater in order to produce such a large amount of hot ionized gas.

Another way of comparing optically thick absorbers and the Milky Way is their total column density ionic ratios. This comparison is depicted in Figure 2, in which the logarithms of the ratios $N_{\text{C IV}} / N_{\text{Si IV}}$ and $N_{\text{C IV}} / N_{\text{O VI}}$ are plotted, along with the mean values for the Milky Way and the high-z absorbers, both with and without limits. The high-z absorbers have a lesser mean value for $\log[N_{\text{C IV}} / N_{\text{O VI}}]$ (-0.52) and a greater mean value for $[N_{\text{C IV}} / N_{\text{Si IV}}]$ (0.83) as

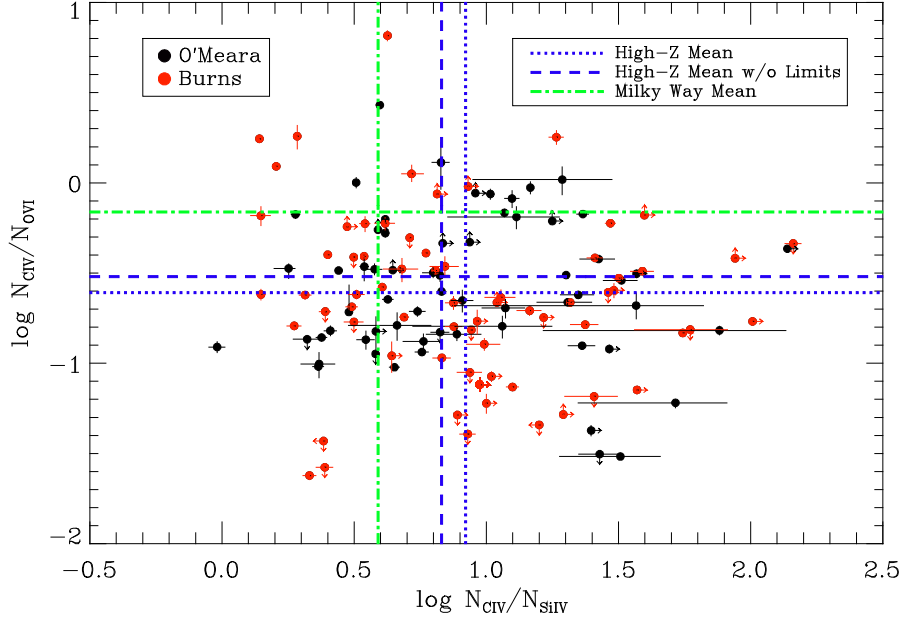


Figure 2: Plot of $\log[N_{\text{C IV}} / N_{\text{Si IV}}]$ and $\log[N_{\text{C IV}} / N_{\text{O VI}}]$. Errors are plotted as bars and limits are indicated by arrows. The mean values with and without limits for high-z are drawn in blue, while the mean value for the Milky Way is in green. Orange points are absorbers identified by the author, while black points were identified by Professor O'Meara.

compared to the Milky Way (-0.16 and 0.59), meaning DLAs and LLSs tend to have relatively more O VI and C IV than galaxies in the Milky Way, suggesting again the presence of more hot gas at high redshift in the galaxy-IGM interface.

A final preliminary analysis can be undertaken involving the velocity ranges of the high ions, which are shown in Figure 3. The line plotted on the graph is $y = x$, so the closer a point is to the line, the more similar the velocity ranges of the two ions. Most of the data are below the line for the $\delta v_{\text{Si IV}}$ versus $\delta v_{\text{C IV}}$ graph, implying that generally $\delta v_{\text{Si IV}} < \delta v_{\text{C IV}}$. When $\delta v_{\text{C IV}}$ is compared to $\delta v_{\text{O VI}}$, the data are more scattered, indicating that hot gas is observed over a larger velocity interval than cooler gas. It should be noted that the O VI sample likely includes absorbers that are contaminated by the Ly α forest, especially over large velocity intervals.

Further Research

This survey is a preliminary step in a larger research effort to gain a better understanding of the interactions of the IGM and galaxies at high-z. The most important result is the compilation of a comprehensive sample of DLAs and LLSs and an organized database of the

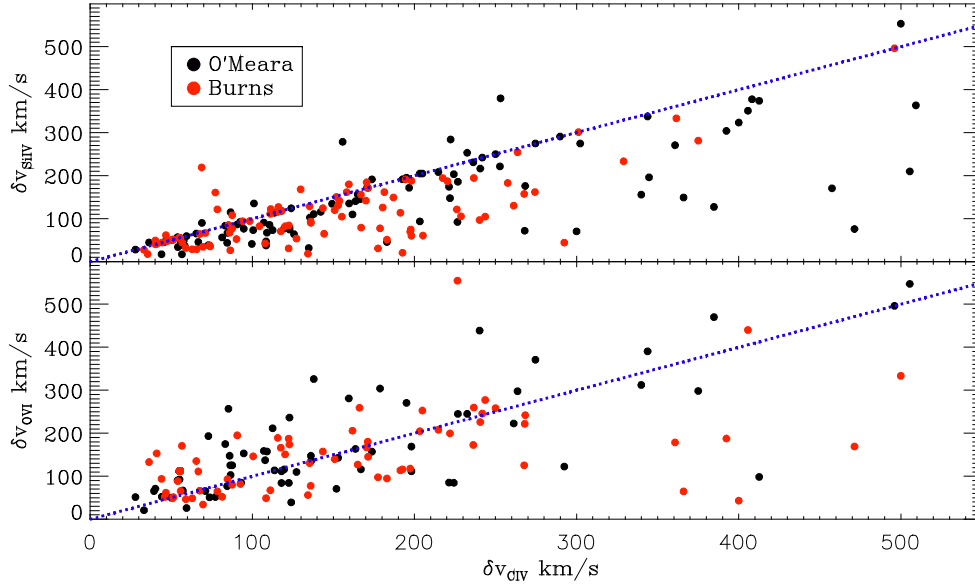


Figure 3: The $\delta v_{\text{Si IV}}$ and $\delta v_{\text{O VI}}$ as a function of $\delta v_{\text{C IV}}$. The line plots a 1:1 ratio. No errors were found for the measurements.

properties of their key high ions. The sample includes a degree of magnitude more O VI lines than any other previous study, a notable accomplishment. Nevertheless, much work lies ahead. Over 25 percent of the QSO spectra need to be analyzed. $N_{\text{H I}}$ measurements of the author's sample need to be estimated to identify DLAs versus LLSs. Metallicities need to be measured to estimate the amount of ionized gas. Profile-fitting needs to be undertaken to determine the different phases and their properties in each DLA and LLS. Results need to be compared to theoretical models to constrain the ionization mechanisms. The work will require much more effort, but this survey is an essential first step.

Acknowledgements

I would like to thank my advisor, Professor Lehner, for the opportunity to undertake this research and for his investment of time in ensuring that I understood the overall focus of the project. Special thanks to Michelle Consiglio for her useful advice. I am indebted to the generosity of the Glynn Family for supporting my research, and Dr. Umesh Garg, Heather Christensen, and the University of Notre Dame REU program for integrating me into the department.

References

- Fox, A., Ledoux, C., et al., 2007a, A&A, 473, 791
- Fox, A., Petitjean, P., et al., 2007b, A&A, 465, 171
- Fox, A., Petitjean, P., et al., 2007c, ApJ, 668, L15
- Fox, A., Prochaska, J. X., et al., 2009, A&A, 503, 731
- Lehner N., Howk, J. C., et al., 2008, MNRAS, 390, 2
- Lehner N., Prochaska, J. X., et al., 2009, ApJ, 694, 734
- Lehner, N., Zech, W., et al., 2011, ApJ, 727, 46
- Savage, B., & Wakker, B., 2009, ApJ, 702, 1472

Analysis of a Potential Tracking Algorithm for the SLHC Upgrade

Rachael Creager

Michael Swift

2012 NSF/REU Program

Physics Department, University of Notre Dame

Advisors:

Professor Michael Hildreth

Professor Kevin Lannon

3 August 2012

ABSTRACT

This work studies a triggering algorithm for the proposed 2020 upgrade to the Compact Muon Solenoid (CMS), one of the main detectors in the Large Hadron Collider (LHC) in Geneva, Switzerland. This upgrade will begin the era of the Super Large Hadron Collider (SLHC). The luminosity of the collider will increase by roughly a factor of 10, allowing for observation of extremely rare events. The large number of interactions, however, would overwhelm the current trigger system, making it impossible to select interesting events from the background. The SLHC will thus include an upgrade to the silicon tracker for CMS, which will use high-speed electronics to track particles in the lower layers of the detector. By reconstructing a particle's trajectory in the detector's magnetic field, the Level-1 trigger identifies events containing high-energy tracks to be processed by the software trigger. This work focuses on the optimization of the tracking algorithm for the Level-1 trigger using simulated collision data. Specifically, we seek to increase efficiency of track finding while simultaneously avoiding "fake" tracks (those which do not correspond to an actual particle). We show that this algorithm successfully maintains this balance, and would make a good foundation for the SLHC Level-1 trigger.

1. WHAT IS THE LARGE HADRON COLLIDER?

Located about 100 meters underground in Geneva, Switzerland, the Large Hadron Collider (LHC) is the largest and most powerful particle accelerator in the world. The LHC consists of three main parts: the 27-kilometer circular accelerator tunnel, four different detectors, and the Worldwide LHC Computing Grid[?]. By colliding protons or heavy ions, physicists use the LHC to study some of the most fundamental questions in particle physics. The LHC is designed to accelerate protons up to an average energy of 7 TeV, or about 7500 times the rest mass of a proton. This will result in a maximum collision energy of 14 TeV. However, reaching a high energy is not enough to guarantee results; the particle beams must also be very tightly packed to increase the probability of collision. The LHC is currently designed to reach a maximum luminosity (or particles per unit area per unit time) of $10^{34} \text{ cm}^{-2} \text{ s}^{-1}$ [?]. The current LHC design has produced important results, especially the recent discovery of a Higgs-like particle.

2. WHAT IS THE COMPACT MUON SOLENOID?

The Compact Muon Solenoid (CMS) is one of the two major detectors at the LHC. CMS gets its name from the large superconducting solenoid magnet it uses to generate a 3.8 T magnetic field in the detector. CMS is 21 meters long, 15 meters in diameter, and weighs about 12500 tonnes[?]. It is divided into five layers: the solenoid layer and the four different detector layers. The innermost layer, the silicon tracker, is the focus of our study. The tracker is made of layers of silicon strip and pixel detectors arranged into barrels with endcaps. All particles can pass through the silicon tracker, but it is used to track the curved paths of charged particles. Therefore, the silicon detector cannot track photons or other neutral particles. The second layer, the Electromagnetic Calorimeter (ECAL), is made of lead tungstate (PbWO_4) crystals, which produce a small amount of light when any type of particle passes through them. This light is then detected by silicon avalanche photodiodes (APDs) in the barrel and by vacuum phototriodes (VPTs) in the endcaps. Because photons, electrons, and positrons cannot pass through the ECAL, it is designed specifically to

track these particles. The third layer, the Hadron Calorimeter (HCAL), consists of brass plates with scintillator sheets sandwiched between them. When hadrons pass through the HCAL, they interact with the nuclei in the detector and produce charged particles. The HCAL is used to detect protons, pions, and neutrons, which are stopped at this layer. The fourth layer is the solenoid magnet, which creates the magnetic field necessary to calculate the momentum of charged particles in CMS. The final detector layer is the muon detectors, which consists of three different types of detectors: drift tubes (DT), cathode strip chambers (CSC), and resistive plate chambers (RPC). Since all other particles have been stopped before reaching these detectors, muons are the only type of particles tracked at this layer.

CMS uses a two-part trigger system to determine which events to record for further analysis. The first part, the Level-1 trigger, reduces the readout rate from about 40 MHz to 100 kHz. This trigger is currently implemented in the hardware of the HCAL, ECAL, and muon detectors. The second part of the trigger system, the High Level Trigger (HLT), uses a computer farm to reduce the readout rate further from about 100 kHz to 300 Hz.

3. SLHC UPGRADE

In about 2020, the LHC will be shut down for a period of time in order to perform the SLHC upgrade. After the upgrade, the luminosity of the collider will increase by about a factor of 10[?]. This will lead to a dramatic increase in the number of collisions per crossing. The CMS trigger system is not designed to handle this level of collisions, which would overwhelm the current HLT. To deal with this, the upgraded Level-1 silicon trigger must be able to more effectively reduce the number of events to be processed by the software trigger. Currently, the silicon tracker cannot read out information quickly enough to be used by the Level-1 trigger. When the LHC is shut down for the upgrade, however, the silicon tracker must be replaced due to radiation damage. This is the perfect opportunity to replace the silicon tracker with a more advanced tracker. Specifically, the proposed design for the silicon tracker would be able to read out quickly enough to be used by the Level-1 trigger.

In the current CMS detector, the Level-1 trigger does not include any form of track reconstruction[?]. The algorithm we are analyzing, however, does include basic tracking. This has the potential to improve the triggering dramatically by incorporating the particle's transverse momentum, or p_T . Particles from background events tend to have low p_T while particles from interesting events tend to have high p_T . Many of these background events come from *pileup*, events resulting from glancing collisions of particles in the detector. Track reconstruction thus allows our algorithm to weed out a much higher percentage of the background than is possible with the current Level-1 trigger.

4. STUBS AND MOMENTUM CALCULATION

When a particle of charge q travels perpendicular to a magnetic field B at velocity v , it experiences a force Bqv perpendicular to its motion. This force moves the particle along a circular path of radius r (called the radius of curvature). We can describe this motion by the following equation[?]:

$$Bqv = \frac{mv^2}{r}$$

We can use this to obtain the following equation for the transverse momentum of a particle (p_T):

$$p_T = Bqr$$

Since all the particles we are dealing with have charge $\pm e$, we can further simplify this equation. By converting from SI units to relativistic units, we produce the following:

$$p_T = 0.3Br$$

Where B is given in Tesla, r in meters, and p_T in GeV/c. Since the strength of the magnetic field is set at 3.8 T, we need only find the radius of curvature r to calculate p_T .

One way to calculate the radius of curvature for a particle is by using "stubs". The figure below is a basic diagram of the detector:

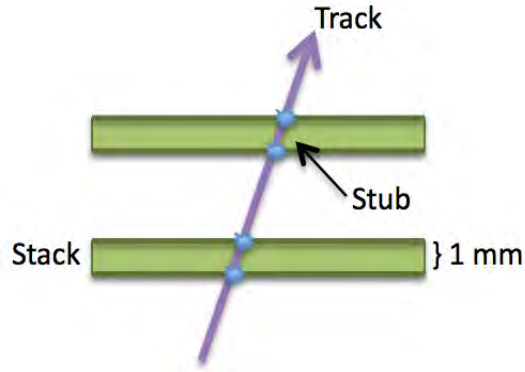


Figure 1. Detector Terminology

Each layer of the detector consists of a “stack”, a pair of two sensors separated by about 1 mm of silicon. A particle passing through the detector is recorded by both sensors. We call such a pair of hits a “stub”. The relative positions of the hits gives a direction for the stub. We can use this direction to calculate the transverse momentum, p_T , of the stub.

We tested out two methods of calculating r from the stubs. Locally, radius of curvature is given by $r = \left| \frac{ds}{d\phi} \right|$. This is done by approximating the change in arclength and angle of the stub. We also tested a calculation which uses the global position of the hits within the detector and the fact that the track must have begun at the origin of the detector.

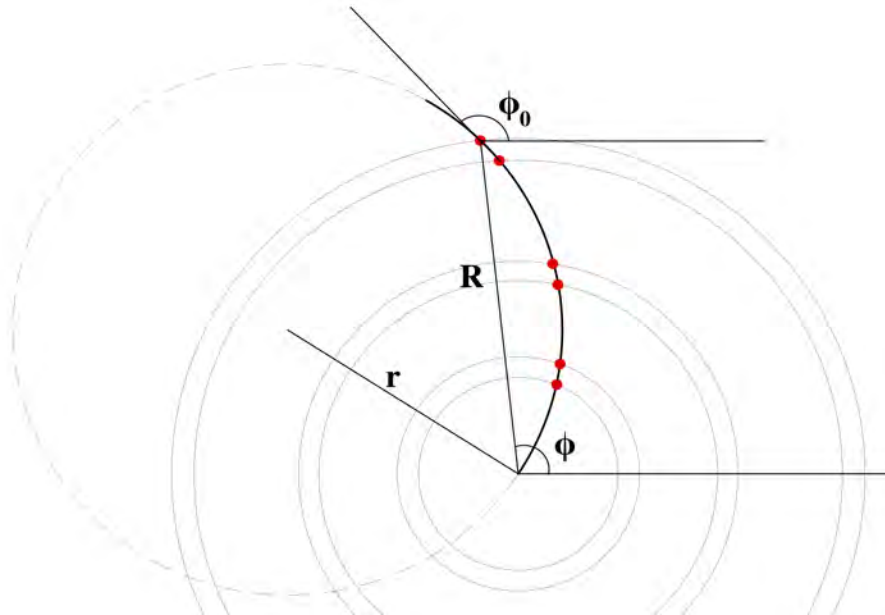


Figure 2. Geometry of the Radius of Curvature Calculation

This leads to

$$r = \frac{R/2}{\sin(\phi - \phi_0)}$$

Where R is the radius of the detector, ϕ is the angular position of the stub within the detector, and ϕ_0 is the angular direction of the stub. We hoped that this formula would give better accuracy in stub p_T than the local formula, since it incorporates more information about the track. However, the overall performance of the two different formulas was very similar. Since the separation between the hits in a stub is so small, the errors in stub p_T are too high to use stub p_T alone for triggering.

5. LIMITATIONS ON THE ACCURACY OF STUB p_T MEASUREMENTS

To investigate the source of p_T error, we looked at the plots of the transverse momentum (p_T) of stubs from a set of 50000 muons all with $p_T = 2$ GeV:

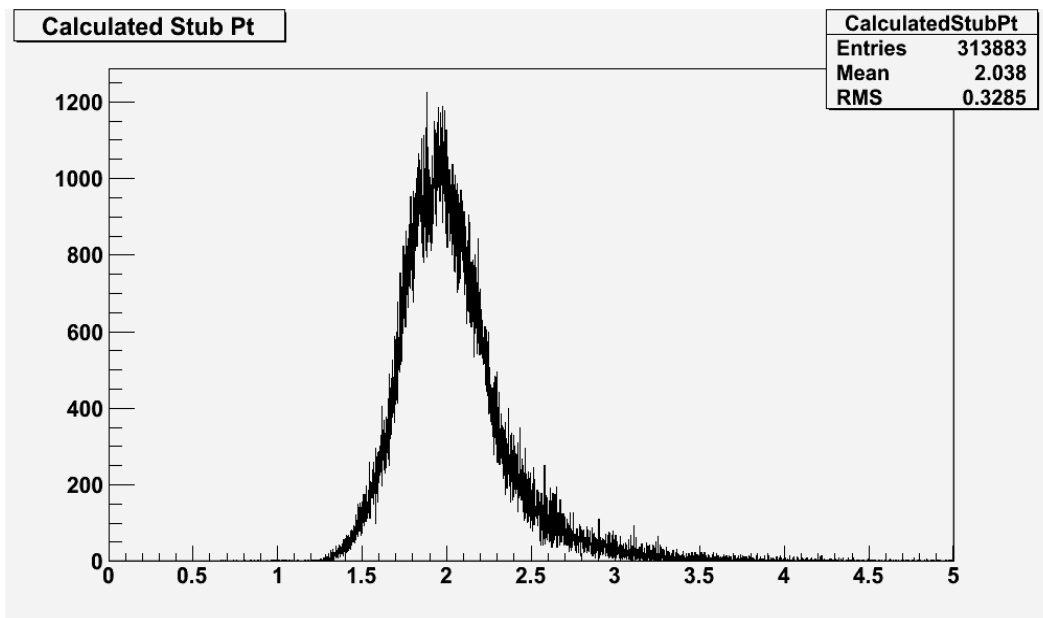


Figure 3. Calculated Stub Pt, Random ϕ

We decided to limit the momentum measurements to a small region of the detector (small η and ϕ range). Instead of finding a smooth distribution over a small range, we found several distinct peaks in momentum measurement.

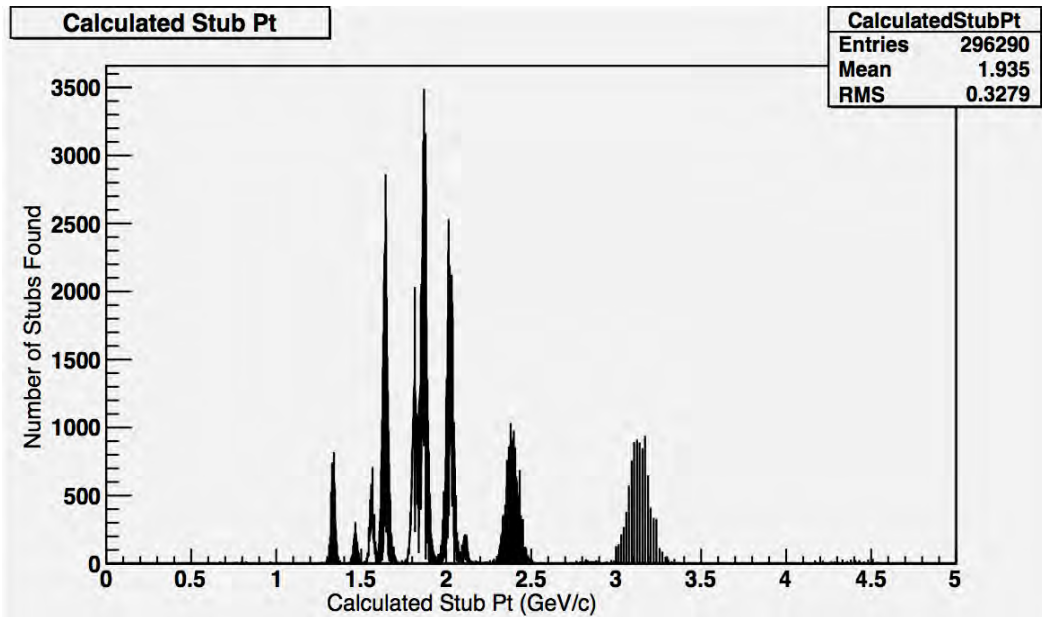


Figure 4. Calculated Stub Pt, Fixed ϕ

Looking at the ϕ dependence of the stub p_T , we found a pattern we called “cat scratches”. The cat-scratch pattern is the cause of the peaks in the p_T spectrum: a small ϕ slice overlaps with approximately three of these cat scratches per layer, giving a few discrete p_T values.

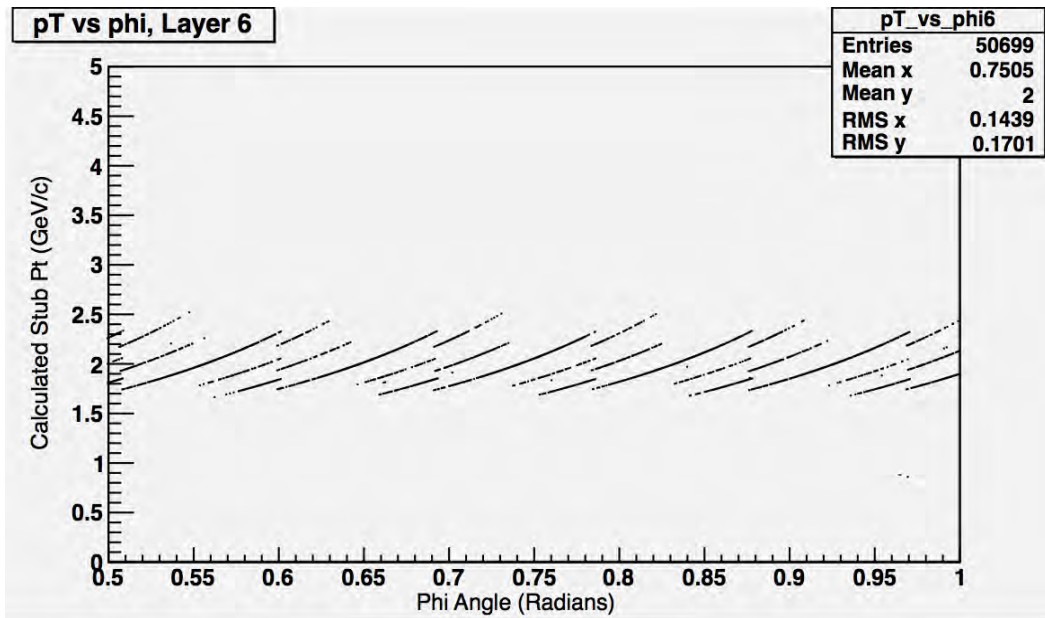


Figure 5. Cat Scratch, Random ϕ , Layer 6

But what causes the cat scratch phenomenon? We look the global formula for p_T calculation:

$$p_T = \frac{(0.3)(3.8)(R/2)}{\sin(\phi - \phi_0)}$$

Using this formula, we hypothesized that the cat-scratch shape is due to the geometry and pixilation of the detector. The width of the pixel detectors is $100 \mu\text{m}$, and stacks are only 1 mm thick. Thus the resolution in the direction of a stub is poor, and only a few discrete ϕ_0 values will be measured, instead of a smooth continuum. For each possible ϕ_0 , then, $\sin(\phi - \phi_0)$ varies like $\sin(\phi)$. Across the angular width of one detector, this is approximately linear, causing a linear trend in the cat scratch plot. The distance R from the center is highest at the edges of the detector and lowest in the middle, giving an overall curve to the pattern. There is one such pattern for each detector and each possible ϕ it measures.

To test this hypothesis, we went back to the directed beam. Instead of plotting the p_T of the stubs from every layer, we decided to focus only on the sixth layer. There were 3 distinct p_T values measured in this layer:

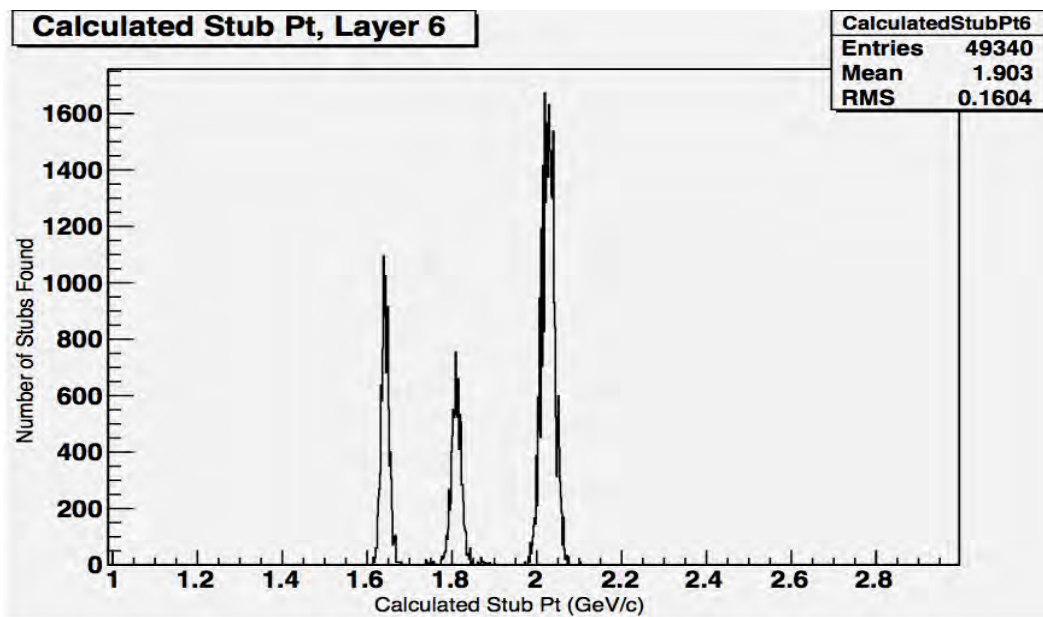


Figure 6. Calculated Stub p_T , Fixed ϕ , Layer 6

We found that each of these peaks correspond to one ϕ_0 value, confirming our hypothesis. The directional resolution of individual stubs is quite poor, and there is significant discretization of the directional measurements. Thus much of the error in stub p_T measurements is likely due to the low precision in the measurement of stub direction.

6. FULL TRACK RECONSTRUCTION

Because of the high error in stub p_T calculation, it is not suitable for initial track reconstruction. Therefore, the algorithm uses the position of the stubs to reconstruct the particles' trajectories. Please refer to the following diagram:

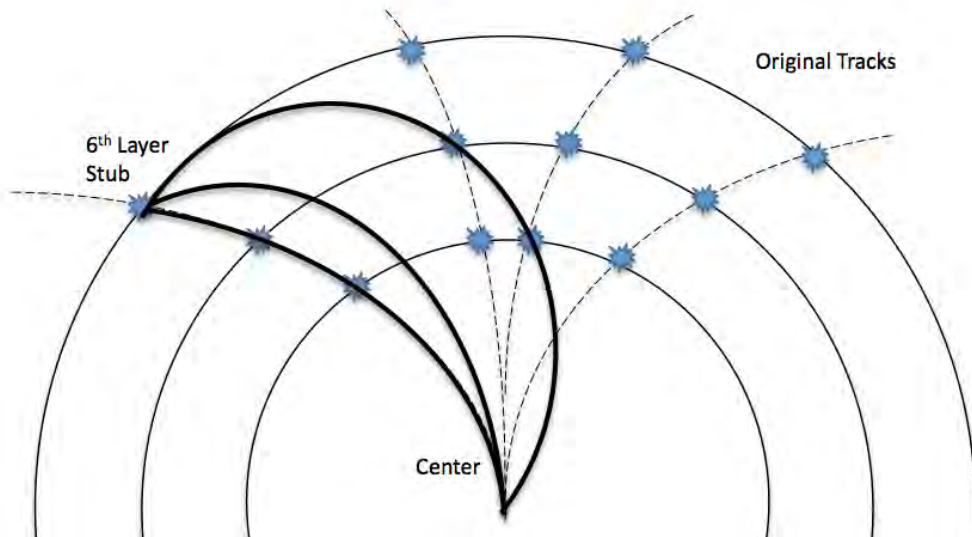


Figure 7. Track Reconstruction

The algorithm works by first identifying the stubs in the sixth layer. We made the assumption that any particle that makes it to the sixth (outermost) layer of the detector began its path at the center and left stubs in each of the five lower layers. To determine the momentum of the particle that made the track, the algorithm searches through different ranges of p_T and looks for stubs along a trajectory consistent with that p_T and sixth layer stub, represented by the thick lines in the diagram. To check these locations, the p_T ranges are converted into ϕ ranges using the layer radii and the p_T calculation formula. We call these ranges “ ϕ windows”. The width of the ϕ windows depends on the range in p_T it is checking.

In this algorithm, p_T windows can be defined in two ways: equal separation in p_T and equal separation in curvature (the inverse of radius of curvature). We decided to check ϕ windows of equal p_T width in the low p_T range and windows of equal curvature width in the high p_T range. Since low p_T tracks are more curved, it is easier to distinguish between tracks of different p_T . Therefore, we use smaller p_T windows in the low range. High p_T tracks are more straight, so it takes a greater difference in p_T to tell them apart. Therefore, we use wider p_T bins in the high range.

If the algorithm finds stubs in each layer for a particular ϕ window, then we say that p_T range corresponds to a “found” track. All of the found tracks for a particular sixth layer stub are stored for further analysis.

Although most particles fall in the middle of the ϕ windows, a stub which is found at the border between two ϕ windows will not be found properly by the algorithm. To account for this, we added an percent overlap value called “slop”. A high value of slop will allow the algorithm to pick up all particles that would otherwise be missed, but will also cause the algorithm to pick up particles which do not actually correspond to that ϕ window.

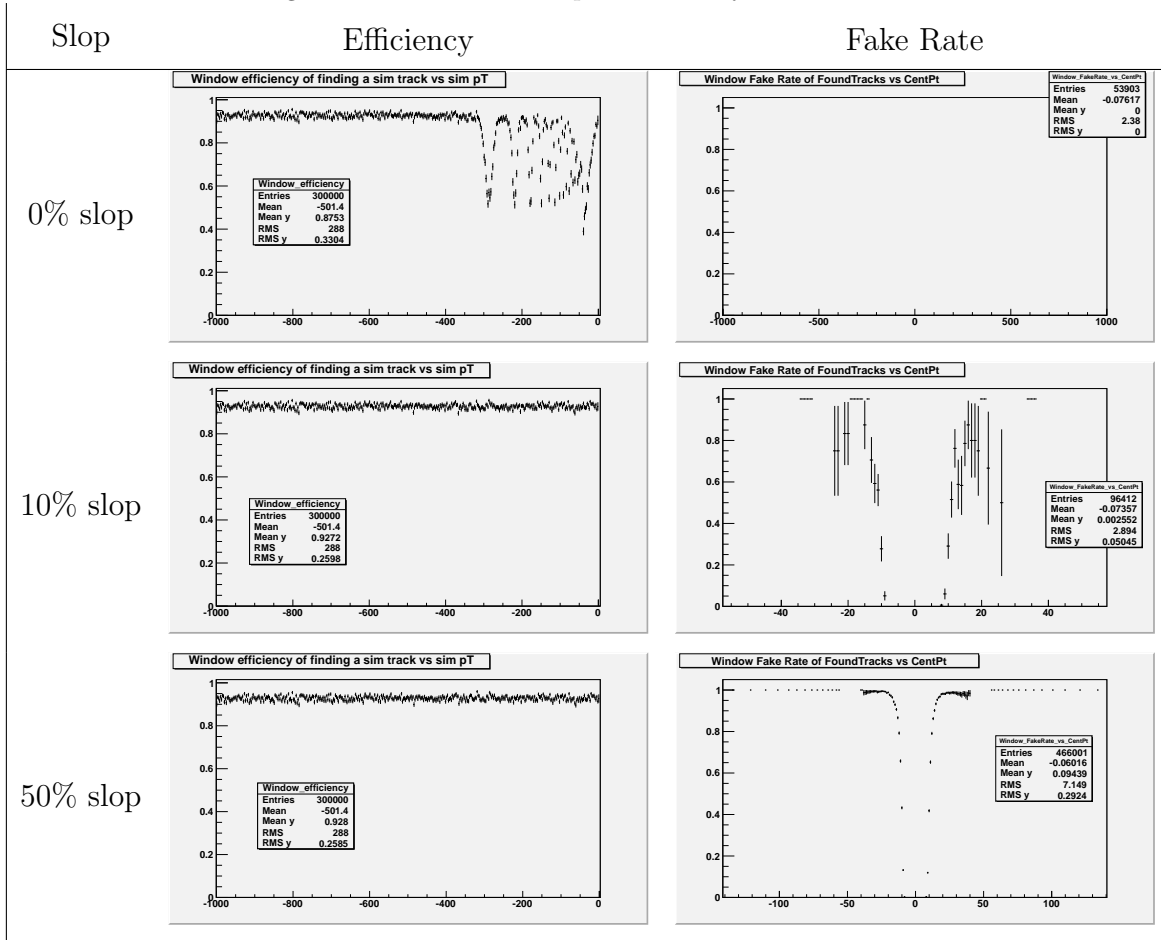
7. EFFICIENCIES AND FAKE RATES

Any triggering algorithm must strike a balance between efficiency and fake rate. Efficiency describes the rate at which the trigger correctly identifies a track. Conversely, the fake rate is the rate at which the trigger incorrectly reconstructs a track. An ideal trigger would pass all interesting events while rejecting all uninteresting ones. Unfortunately, changes which increase efficiency tend to increase fake rate as well, and vice versa. In our analysis of the code, we developed a system to measure these parameters, and used it to tune the track finding algorithm.

We declare a particle “found” if the algorithm reconstructed a track with p_T and ϕ close to the actual values of the particle. The width of this window is p_T dependent, based on the typical spreading for single-track events. If the algorithm found a close track for a high percentage of the particles, we say it has good efficiency.

To measure the fake rate, we invert the process. A track is considered “real” if its p_T and ϕ values are close enough to those of an actual particle. If not, it is labeled a “fake”.

Figure 8. The Effect of Slop on Efficiency and Fake Rate



The above figure shows the effect of changing slop on the efficiency and fake rate of the algorithm. The efficiency plots show the percentage of muons which were found by our algorithm in 300,000 single-track events. With zero slop, tracks near the edges of p_T bins have reduced efficiency, as discussed above. Increasing slop to 10% gives fairly uniform efficiency of about 93% across the tested p_T range. Further increasing slop to 50% has a negligible effect on the efficiency. Fake rate was tested a sample of 240 events, each consisting of 100 pileup interactions. With 0% slop, the algorithm found no fake tracks, but

fakes started to appear as slop was increased, with higher rates for higher slop. This is a good illustration of the trade-off between efficiency and fake rate.

8. CONCLUSION AND FURTHER WORK

This algorithm provides a good basis for the design of a Level-1 tracking trigger. Various adjustable parameters such as the ϕ windows and slop can be changed to optimize the algorithm. Our values for these parameters lead to high efficiencies and low fake rates.

This is a very big project and there is much still to be done. Minor tweaks to the current algorithm, such as changing the implementation of slop or stub finding, might help performance. The algorithm could incorporate stub p_T in addition to stub position when looking for tracks. The performance of the algorithm should be evaluated for non-muon particles such as electrons or pions. The algorithm could also be tested with other proposed upgrade geometries. Finally, since the Level-1 Trigger will be implemented in FPGA hardware, further work will need to investigate the feasibility of coding the algorithm directly into high-speed electronics.

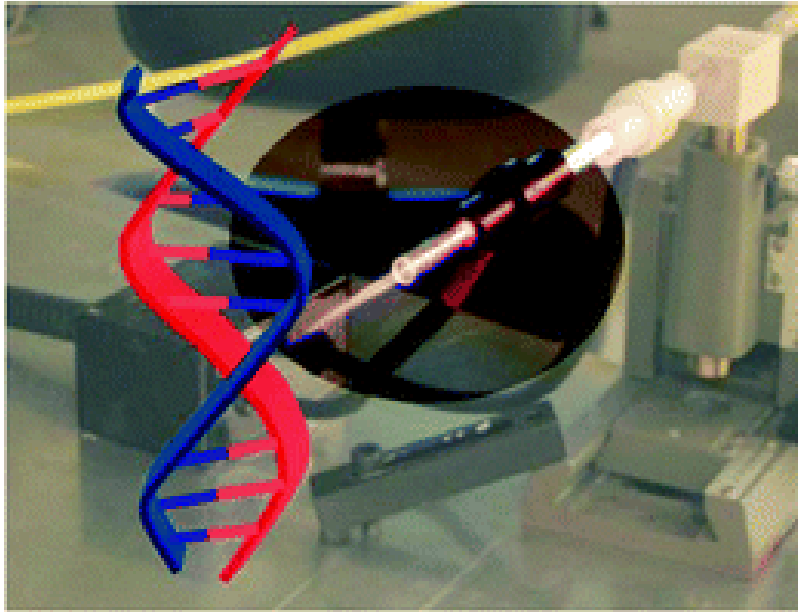
ACKNOWLEDGEMENTS

We would like to thank Professor Lannon and Professor Hildreth for their guidance and support throughout the summer. We would also like to thank Professor Garg for his care and dedication to the Notre Dame REU Program. Additionally, we would like to thank Kevin McDermott and the other REU and Notre Dame students who have contributed to this project. Finally, we would like to thank NSF and the Glynn Family Honors Program for making this experience possible.

REFERENCES

- [1] CMS Collaboration, “CMS Physics: Technical Design Report.” Vol. 1. *European Organization for Nuclear Research*, 2 Feb. 2006. Web. 31 July 2012.
- [2] Merino, Beatriz, and de la Cruz, Clara, “Detectors at the LHC: ATLAS and CMS”. *Universidad Complutense Madrid-Spain*, n.d. Web. 31 July 2012.
- [3] Jones, Gron, et al., “Measurement of Particle Momentum.” *High School Teachers at CERN*, 2005. Web. 31 July 2012.
- [4] sLHC Specification Committee, “sLHC.” *European Organization for Nuclear Research*, n.d. Web. 31 July 2012.
- [5] *What is the LHC?* Science and Technology Facilities Council, 2012. Web. 31 July 2012.

Using the Atmospheric Pressure Plasma Jet to Assess the Effects of Plasma on DNA Molecules



Erika Escobar

2012 NSF/ REU Program

Physics Department, University of Notre Dame

Radiation Laboratory

Advisor: Dr. Sylwia Ptasinska

Abstract

Nonthermal atmospheric pressure plasma has much potential for medical applications. The atmospheric pressure plasma jet (APPJ) contains almost equal amounts of positive and negative charges. Ongoing research has been done to test whether plasma can be used to destroy DNA molecules belonging to tumorigenic cells or even cancer cells themselves, which could provide an alternative method to treat this disease. In this research we focused on the possible biomedical application of the APPJ, where we used plasma ignited in helium (He) gas flow to cause strand breaks in DNA. However, the mechanism by which plasma destroys DNA is not yet understood. In this study we assessed the effects of helium plasma on DNA as compared to helium gas flow. We also investigated the effects of distance between the quartz tube of the plasma source and the DNA sample. In this study we found that plasma does indeed alter DNA. We came to this conclusion through qualitative interpretations using a standard gel electrophoresis technique on DNA samples treated with the APPJ.

Introduction

Nonthermal Atmospheric Pressure Plasma and its Applications

Nonthermal atmospheric pressure plasma is composed of UV light, radicals, positive and negative charges traveling in a flow of gas in a plasma jet. One reason for why the APPJ is advantageous is because even though the electrons and other species which are generated might be hot due to their high kinetic energy, the overall gas is at room temperature. This property of the APPJ can later be used to treat living tissue, which could be harmed if the temperature is elevated. Nonthermal atmospheric pressure plasmas can be used for biomedical applications such as in dentistry in which it is used for teeth bleaching, (Lee 2009) and in material processing such as cleaning of surfaces. (Belkind 2008)

In the case of microplasmas, they have been found to be able to “inactivate microorganisms and destroy biomolecules,” such as DNA and proteins. Hence, plasma has gained the function of a “bactericidal” agent and “decontamination technology to address contamination of surgical instruments.” (Felipe Iza, 2008)

Still, other studies have found that plasma can be used to destroy tumors. (Kim 2010) Researchers hope that in the future plasma can be used to eradicate cancer cells. Because of this, the Ptasinska lab will later experiment with cancer cells aside from the DNA molecules. However, the problem that scientists are facing in regards to using plasma in the clinic in the immediate future is that the mechanism by which plasma works on DNA and other biological molecules is unknown. Plasma can generate a wide array of species and therefore the manner by which plasma attacks DNA can occur through various different reaction pathways. Plasma can generate “excited atoms and molecules, charged particles, electrons, and UV light,” all of which can have different effects on the DNA molecule. (Sylwia Ptasinska, 2010) Knowing this, electrophoresis can serve as a way to find if plasma can break chemical bonds in the plasmid DNA.

Plasmids

Throughout this study we want to know the effects of plasma on plasmid pUC18 DNA. A plasmid is a double-stranded bacterial DNA supercoiled in shape. pUC18 DNA is an artificial E. coli plasmid. Plasmid DNA can be broken in different ways that can be visualized and quantified in the gel. A double-strand break (DSB) occurs when both DNA strands in the plasmid are cut while a single-stranded break (SSB) occurs when only one of the DNA strands is broken.

Materials and Methods

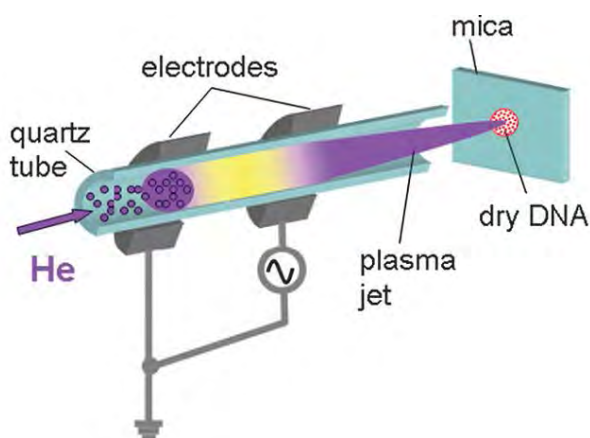


Figure 1: The APPJ consists of a quartz tube of 6mm outer diameter and 4mm inner diameter, surrounded by two metal electrodes.

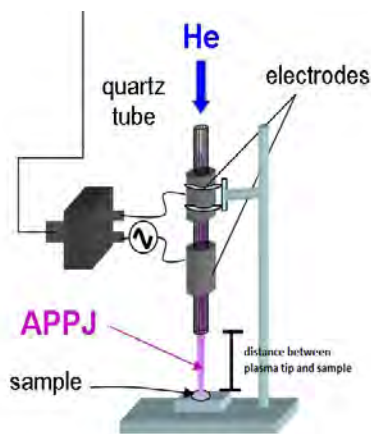


Figure 2: A close up of the APPJ treating a sample of DNA in aqueous solution.

The Atmospheric Pressure Plasma Jet

The APPJ source contains two tubular metal electrodes separated by a 3 cm gap through which a discharge current occurs when one of the electrodes is connected to the HV power supply. Inside the electrodes lies a quartz cylindrical tube through which helium flows. To generate the plasma, we choose a specific shape of wave pulse, the frequency of pulses and the rate of helium gas flow. These parameters have been optimized and chosen in such a manner to form the most stable and long APPJ plasma. Once we have decided upon these parameters, the plasma is launched through the open end of the quartz cylindrical tube into the sample.

Wet DNA Experiments

10 μ L of DNA solution were placed in wells (20 μ L maximum fit) in boron silicate glass. The experimental set-up followed the parameters delineated in the chart below.

There were three different types of controls in these experiments. The gas flow control did not have plasma treatment as only helium gas would come in contact with the sample. This allows us to disregard the possibility that helium itself could be doing the DNA damage rather than just the plasma. Another control was the well control, in which DNA was not treated with either plasma or gas flow. The third control was the tube control, which was made by acquiring DNA directly from its storage microcentrifuge tube.

Sample	Type of treatment	Plate distance from plasma source (cm)	Helium Gas Flow Rate (L/min)	Frequency (kHz)	Time Duration (seconds)
1	Plasma	15	4.02	2.5	20
2	Plasma	14	4.02	2.5	20
3	Plasma	13	4.02	2.5	20
4	Plasma	12	4.02	2.5	20
5	Plasma	11	4.02	2.5	20
6	Gas flow, no plasma	11	4.02	2.5	20
7	Well control	N/A	N/A	N/A	N/A
8	Tube control	N/A	N/A	N/A	N/A

Another experiment was done to determine the effect of different time durations of treatment on wet samples placed 6cm from the quartz tube. The samples were prepared with the same procedure as previously stated for wet samples. The table below summarizes the parameters used in this approach.

Sample	Type of Treatment	Plate Distance from plasma source (cm)	Helium Gas Flow Rate (L/min)	Frequency (kHz)	Time Duration (seconds)
1	Plasma	6	4.02	2.5	10
2	Plasma	6	4.02	2.5	20
3	Plasma	6	4.02	2.5	30
4	Plasma	6	4.02	2.5	40
5	Plasma	6	4.02	2.5	50
6	Plasma	6	4.02	2.5	60
7	Well control	N/A	N/A	N/A	N/A
8	Tube control	N/A	N/A	N/A	N/A

Gel Electrophoresis

After each sample is treated with the APPJ it is placed in a microcentrifuge tube with 2 μ L of Loading Dye. Up to 15 μ L of distilled water are added to the well to make sure that no DNA remains in the boron silicate well. The samples are then loaded on a gel and placed on the Bio Rad electrophoresis chamber with 10X TBE to run at 70V for three hours.

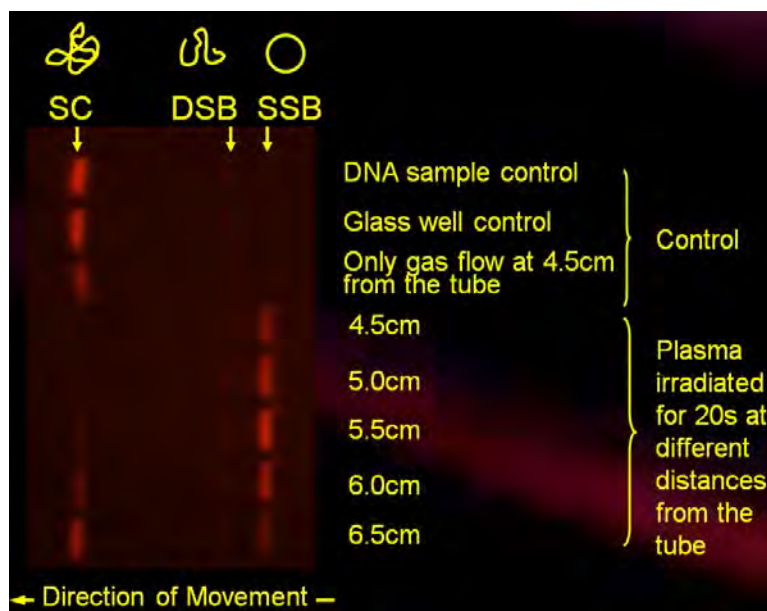


Figure 3: An example of a gel electrophoresis under the UV analyzer.

Gel electrophoresis consists of a positive and a negative electrode placed in opposite ends of a chamber. Once the voltage runs across them, they separate molecules according to charge and size. DNA is negatively charged and therefore runs towards the positive electrode. Because the agarose matrix gel is porous, smaller fragments will travel faster than the larger fragments. SC travels faster because it behaves like a ball of yarn, going through the gel matrix with ease. Meanwhile, the DSB adopts a linear conformation, which makes it harder to go through the gel than a sphere and so it travels less than the SC. The slowest is SSB, since it adopts a hoop conformation, which lacks the ease of going through the gel that the SC and the DSB have.

Note that in this example the DNA sample control and the glass well control, both of which are untreated, are not damaged. Furthermore, strand break yields of DNA increases with decreasing distance from the plasma jet tip. The electric field within the gel electrophoresis chamber will separate the SC, SSB, and DSB DNA from each other. These separations will be visible as bands when the gel is viewed under UV light.

Image Analysis

Gel is placed inside Bio Rad Trans UV analyzer using the program Origin One, which also provides numerical values for the intensity of the bands and hence provides a numerical

quantity of the amount of DNA in the sample. Before the samples are loaded on the gel, the gel is made with 60mL 10X TBE mixed 0.48g agarose powder, boiled, left to cool down to 65°C, and then 3µL of SYBR Green are added. The SYBR Green will make the bands fluoresce under the UV light of the gel imager.

Results

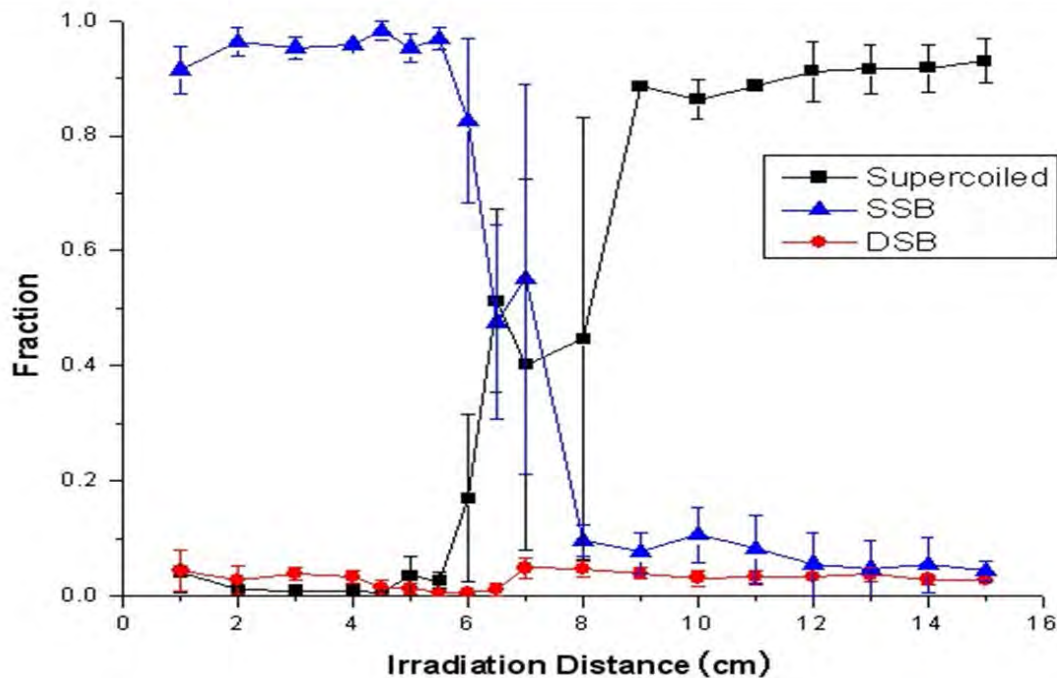


Figure 4: DNA strand breakage as a function of distance (cm) between the APPJ source and the sample.

Figure 4 shows the results of the experiments in which we test the different distances from the plasma source. For the SC bands, the graph demonstrates that there is less supercoiled DNA at a closer distance to the plasma source, but as the distance from the source increases, the supercoiled DNA presence is increased. Figure 4 also shows that the DSB do not change much as a function of distance, whilst SSB are present in higher yield closer to the quartz tube than when it is at a larger distance. Furthermore, the graph suggests that the region of most damage occurs up to 5-8cm distance from the quartz tube. SSB yield is highest at the shorter distances from 0-6cm, while for these same distances the supercoiled DNA has the smallest yield. Hence, the closer the sample is to the plasma source, the more SSB damage. DSB damage, on the other

hand, is not influenced by distance to the quartz tube nor does it seem to be affected much by the APPJ.

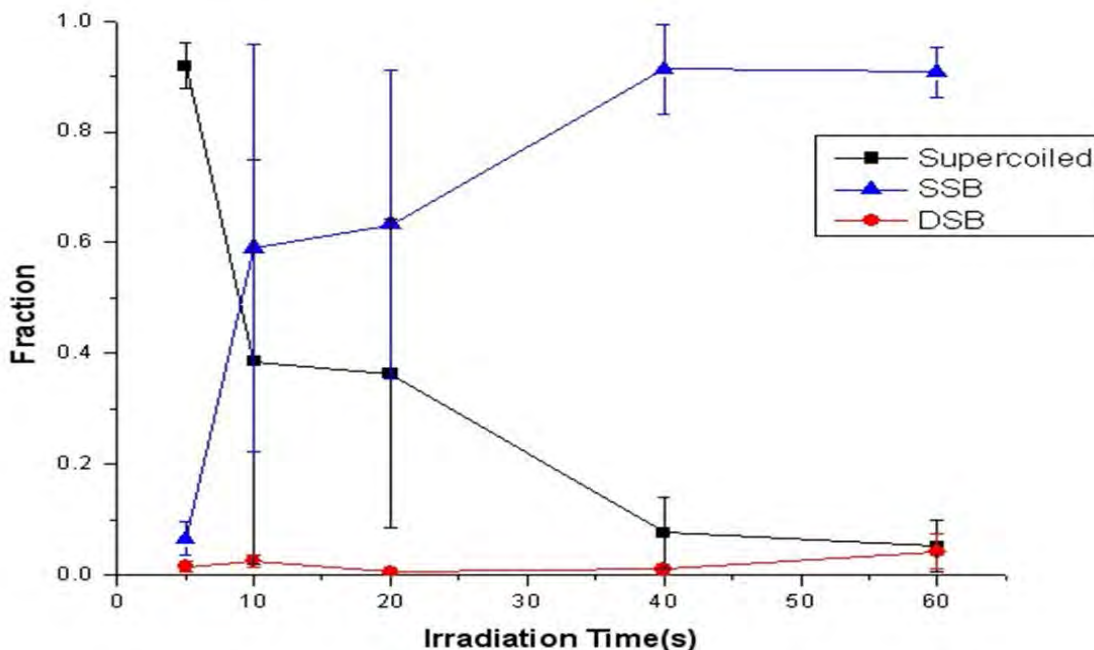


Figure 5: DNA strand breakage as a function of irradiation time.

Figure 5 shows the results for the different exposure time with the samples at 6 cm away from the quartz tube. As the graph shows, the presence of supercoiled bands decreases with increased time exposure of the sample to the plasma. Meanwhile, the presence of SSB bands increases as time increases. Lastly, the DSB bands do not change much between the 0 and 60 second time spans. As Figure 5 suggests, the more time that the sample is treated by the plasma, the more SSB will occur.

Discussion and Conclusion

Some factors to note are the large error bars in Figures 4 and 5. One reason for these error bars is instability of the plasma jet at the tip. Due to the nature of plasma the length of the APPJ can vary about 1 cm. This can influence the amount of DNA strand breakage as compared from one sample to the other.

Using the APPJ, we have found that the optimal distance for the most SSB of DNA is at the plasma jet tip while the longer that we treat the sample, the more SSB damage there will be. However, we have noted that APPJ does not induce DSB damage.

Currently, the Ptasinska lab is also studying the effects of the APPJ on dry DNA samples. These experiments differ from the wet sample trials discussed in this paper in that the DNA is placed in a mica slide and the sample is left to dry before being treated. For these experiments, the APPJ is placed in a horizontal position. These experiments will help understand the direct effects of plasma on DNA without an aqueous environment.

Another question that the Ptasinska lab will focus on is the effects of fullerenes on the DNA. A fullerene is a C_{60} molecule whose extensive conjugation could be a sink for the radicals in plasma. (Thakral, 2006) Because of this, the Ptasinska lab will investigate whether fullerenes protect DNA from APPJ-induced damage. Knowing this information would help gain more knowledge about the roles of fullerenes in the medical field.

Lastly, the Ptasinska lab will also assess the effects of the APPJ directly on cancer cells. This research will help build new frontiers in the chiasm between plasma physics and medical applications to cure cancer and other ailments.

Acknowledgements

I would like to thank the University of Notre Dame, in particular Dr. Umesh Garg, and the National Science Foundation for providing me the opportunity to conduct this research as part of the 2012 Research Experience for Undergraduates. Thank you to my wonderful mentor Dr. Sylwia Ptasinska, graduate student Xu Han, post doc Matej Klas, Joseph Levri, and the rest of the lab for all their help and guidance. This has been a great experience and thanks to the rest of the REU participants for sharing it with me.

References

- Belkind, A. and Gershman S. (2008) Plasma Cleaning of Surfaces. *Vacuum Technology and Coating*.
- Felipe Iza, et al. (2008). Microplasmas: Sources, Particle Kinetics, and Biomedical Applications. *Plasma Processes and Polymers*, 322- 344
- Jae Young Kim, et al. (2010) A flexible cold microplasma jet using biocompatible dielectric tubes for cancer therapy. *Applied Physics Letters*, 96, pp. 96-98
- Lee, Hyun Woo et al. (2009) Tooth bleaching with nonthermal atmospheric pressure plasma. *JOE* (587- 591)
- Molchan, I. et al. (2009) The concept of plasma cleaning in glow discharge spectrometry. *Journal of Analytical Atomic Spectrometry*. (734-741)
- Sylwia Ptasinska, et al. (2010) DNA strand scission induced by a non-thermal atmospheric pressure plasma jet. *Physical Chemistry Chemical Physics*, 12, (7779- 7781)
- Agnieszka Stypczynska, et al. (2010) The influence of amino acids on DNA damage induced by cold plasma radiation. *Physics Letters*, 500(4-6), pp. 313- 317
- Seema Thakral, et al. (2006) Fullerenes: An introduction and overview of their biological properties. *Indian Journal of Pharmaceutical Sciences*, 68, pp. 13-19

Images:

Title Page Figure- Sylwia Ptasinska, et al. (2010) DNA strand scission induced by a non-thermal atmospheric pressure plasma jet. *Physical Chemistry Chemical Physics*, 12, (7779- 7781)

Figure 1: Sylwia Ptasinska, et al. (2009) The effect of a cold atmospheric pressure plasma jet on DNA. *Journal of Physics: Conference Series* 194 (2009) 152029

Figure 2: Agnieszka Stypczynska, *Experimental Investigations of Radiation Induced DNA Damage*. PhD thesis, The Open University, Milton Keynes, UK, 2011. Pg. 4

Using the Theory of Multiple Intelligences to Understand Guided Inquiry

Joanna Flores
Tyler Knowles

2012 NSF/REU Program
Physics Department, University of Notre Dame

Advisor: H. Gordon Berry, Ph.D.

Abstract

We show how guided inquiry in a science classroom theoretically covers Howard Gardner's Theory of Multiple Intelligences. We propose that the success of guided inquiry may rest on this breadth of accessibility to these eight intelligences.

Introduction

During the summer of 2012, we observed four workshops at the University of Notre Dame concerning guided inquiry and modeling instruction for middle and high school teachers. Our observations are the basis for our definitions and the connections made in this paper, and thus may not be found in direct literature.

The Theory of Multiple Intelligences

Howard Gardner introduced his Theory of Multiple Intelligences in 1983, and it has been widely utilized as a descriptive tool in educational circles. Currently, Gardner has identified eight different kinds of intelligences; these are mathematical (the ability to recognize patterns and understand relationships between objects, especially numbers), linguistic (the ability to understand and creatively utilize written and oral language), bodily-kinesthetic (the ability to use the body to create a representation and to handle objects), musical (the ability to create or repeat musical compositions), naturalistic (the ability to categorize objects or ideas), spatial (the ability to visualize representations of objects and procedures), interpersonal (the ability to discern others' emotions), and intrapersonal (the ability to discern one's own emotions) (for more detail, see Gardner's *Frames of Mind*, 1983 and *Multiple Intelligences in Theory and in Practice*, 1993).

Defining Guided Inquiry

Guided inquiry is the process by which students learn through interaction with data, technology, and each other instead of direct instruction. “Stand and deliver” or lecture instruction is rarely effective. The quickest way to transport information is through lecture; however, it is also the quickest way to lose the attention of the students in a classroom. In contrast, one premise of guided inquiry is to ensure the engagement of all students. Through guided inquiry, students are led to their own conclusions using personal experiences - that is, students are being taught how to think and how to solve problems.

Guided inquiry classrooms may also make extensive use of personal whiteboards. The whiteboards can be a medium for group problem-solving and also for reporting data to the rest of the class. Laboratory experiments in a guided inquiry or modeling classroom involve students collecting data without a set procedure. Students are required to create their own procedure and report results without having known the desired result. Science notebooks are another resource for guided inquiry because they allow students to make personal records of what has been learned. Through the inquiry process students are asked questions on multiple levels, including their concrete knowledge, their ability to analyze, and their creativity in synthesis. Finally, when presenting information and discussing the implications of the current model, Socratic seminars promote the inclusion of all student ideas. Taken together, all of these teaching methods promote student learning in the best possible manner, because each student learns differently and is able to see the material presented in a variety of ways.

Connecting Guided Inquiry to Multiple Intelligences

Mathematical Intelligence

Mathematically intelligent students will be able to effectively analyze data: once data have been collected, students have to analyze it and determine the trend. This is especially valuable because students are not given the expected outcome, and therefore have to reason their own way toward a conclusion. Often, the data can be most eloquently expressed in a table, chart, or graph, the creation of which also requires students to draw upon their knowledge of mathematical relationships and definitions.

By working in a group to prepare a whiteboard, students with strong mathematical intelligence can guide those whose mathematical intelligence is not as strong in the process of forming a hypothesis about data trends. This gives students a chance to ask each other questions and check understanding before having to present to a larger group or the entire class. Mathematically intelligent students will also be able to perform a group self-check of numerical answers to aid in confidence during the presentation.

Once data is shared throughout the classroom, the teacher is responsible to lead the students to a data set that most closely resembles the canonical scientific principle being investigated, or to a general consensus combining the results of the entire class.

Mathematically intelligent students will aid in this process by comparing different data representations and looking for unit consistency. Afterwards, depending on the relationship to be established, students can be asked to derive their own mathematical model of the situation, including any formulas that may be useful in expressing the relationship. Here again, students

will have to use mathematical intelligence. Strong mathematical students then have the opportunity to lead those struggling with the mathematical principles of a derivation.

Linguistic Intelligence

With whiteboards, linguistically intelligent students are able to present their work through storytelling. Their creation of this story, which is an interpretation of data, will allow these students to better recall what they have learned. These stories will also help other classmates understand the material.

Lab notebooks are also a way for linguistic students to present their materials through storytelling. The notebook is a personal place for these students to begin to incorporate the new vocabulary. As these students utilize this vocabulary, they are able to help less-linguistically intelligent students learn to use the words correctly. They also learn to effectively describe experimental designs and write acceptable lab reports. Since scientific reading and writing is a specific type of language, students with linguistic intelligence will grasp and model this language fairly quickly when challenged to do so. Again, these types of students are able to help those who do not possess the capabilities of this new science language.

Through Socratic seminars, linguistically intelligent students can become great leaders and role models in leading discussions. Their participation can encourage shy students, who are unlikely to respond to teacher-lead discussions, to participate in discussions. The linguistically prepared explanations are more accessible than teacher explanations for students who are grappling with the concept, again increasing student comprehension.

Bodily-Kinesthetic Intelligence

Kinesthetically intelligent students enjoy hands-on projects rather than writing reports. Simply

the act of gathering into different groups for labs and presentations will make these students more comfortable in a guided inquiry classroom. Labs increase information retention in kinesthetically intelligent students because they can recall bodily movements in the experiments and the process of creating the experimental set-up. Mock demonstrations can be performed by these students during whiteboard presentations or during seminars. This type of presentation is beneficial for conceptual understanding via dramatization with hand gestures and other types of bodily movement. When kinesthetically intelligent students volunteer to dramatize a concept, other students in the classroom are more likely to participate as well.

Though kinesthetically intelligent students may not be strong writers, the science notebooks become their personal record of their actions, reinforcing the concept to be grasped. Once the concept is understood and these students have written it in their own words, they are able to help other students who still struggle with the concept. Not only that, but these students can use the lab notebook to record their ideas about new or unique dramatizations for the concepts.

Musical Intelligence

Musically intelligent students will learn a concept more thoroughly if given a song or rhyme relating to the topic at hand. During bodily presentations, as described above, these students may offer songs or “raps” to help synchronize the movements and remember the order of a process. Even if the teacher has a rhyme or rap from the past, musically intelligent students should be encouraged to create such tools for themselves and the current class. These students can lead the class in these activities and thereby increase participation of students who otherwise might not participate. The combination of actions and music can solidify the concept

and encourage artistic creativity for all students.

Naturalistic Intelligence

Naturalistically intelligent students will excel at object classification in lab. When given the opportunity, these students are able to help their fellow classmates distinguish the differences between objects, and perhaps consider classifications that were otherwise unnoticed.

Naturalistically intelligent students have a stronger capability of noticing the differences and similarities between presented whiteboards. Though students' work may look similar, differences of significant figures, units, and data trends will be noticed. These students can then lead discussions for the class about the importance of a common scientific language for describing data. Naturalistically intelligent students can help the class as a whole come to an understanding that even replicated data can vary within the precision of the measurements.

Through Socratic seminars, naturalistically intelligent students are able to help the group articulate trends. In turn, each student should then be able to explain the concept in his or her science notebook in a way that is personally meaningful. These students can also record unique classifications that have not been addressed in class, and help others make charts, graphs, and other types of organizational tools.

Spatial Intelligence

Although perhaps not initially obvious, some students use their spatial intelligence to picture (in their mind or in a drawing) how an experiment or procedure will work and what the outcome will be. This is especially true if the experiment is one that is readily visible or is a thought experiment.

More obvious is the use of technical drawings in the science notebooks. Spatially intelligent students find it helpful and useful to make drawings where they can put down what they see, helping them to interpret details that they may otherwise have missed. Spatially intelligent students are also able to critique drawings by students who are not as spatially intelligent, helping to promote drawing and interpretation skills.

Similarly, spatially intelligent students find diagrams and drawings on whiteboards easy to understand and interpret. A spatially intelligent student is also able to answer questions about how or why a representation was made the way it was, and should be asked to justify personal representations made in science notebooks. Modeling good justifications will strengthen the class' acuity in producing scientific drawings.

Interpersonal Intelligence

Due to the large amount of group and class interaction in a guided inquiry classroom, interpersonally intelligent students are indispensable. Although it may appear that interpersonal skills would not be useful in understanding science, interpersonal skills in one student will check for understanding in other students. Properly utilized, interpersonal skills will also help to bring out those students who do not often speak or who prefer to work alone instead of in a collaborative group.

In their science notebooks, interpersonal students are encouraged to record observations about the ways in which their groups worked well together or did not work well together. This can give more insight not only into which members are working and which are not, but also into who understands the material and who does not.

During whiteboard presentations, interpersonal students are helpful in mediating and directing discussion. As much as possible, since students are supposed to guide the question sessions, these students should be allowed to find commonalities between groups and prevent disagreements. Interpersonal students can also help cross check understanding across groups and not just within their own.

Intrapersonal Intelligence

Intrapersonally intelligent students need time to reflect on what they have learned in order for the concepts to solidify. Whiteboard presentations and seminars allow time for this to take place. These students are likely to connect what they are learning in the classroom with concepts in their everyday lives, and so can help other students learn the concepts by sharing these connections. Because of the nature of intrapersonally intelligent students, the science notebook is indispensable- it is the record of the students own thoughts on the concepts presented and learned.

Conclusion

Guided inquiry practices are closely tied to all eight multiple intelligences in Gardner' theory. Therefore, we propose that the success of guided inquiry rests on this breadth of accessibility for the different types of students found in classrooms. Since this is a theoretical framework, future research includes studying this link in controlled classroom settings. Further curriculum adaptations should continue to consider elements accessible to all student intelligences, especially those who needs have not been met in traditional classrooms and through traditional teaching methods.

References

NISMEC. *Chemistry Modeling (Intermediate Level) Workshop for SBCSC + Indiana High School Teachers*. University of Notre Dame, 9-29 July, 2012.

NISMEC. *Developmental Biology Modeling Workshop for SBCSC + Indiana High School Teachers*. University of Notre Dame, 18-29 June 2012.

NISMEC. *The Guided Inquiry Science Teacher Institute for SBCSC Intermediate Center Teachers 2012 Workshop 1A*. University of Notre Dame, 11-15 June 2012.

NISMEC. *The Guided Inquiry Science Teacher Institute for SBCSC Intermediate Center Teachers 2012 Workshop 1B*. University of Notre Dame, 12-14 July 2012.

Acknowledgements

First and foremost, we would like to thank our Research Experience for Undergraduates (“REU”) advisor, Dr. H. Gordon Berry, for providing guidance and the opportunity to conduct this research. We also thank the University of Notre Dame Department of Physics for sponsoring the REU in the summer of 2012, including the director Dr. Umesh Garg. We gratefully thank the National Science Foundation and the Notre Dame Department of Physics for funding this program. We also thank the Northern Indiana Science, Mathematics and Engineering Collaborative (NISMEC) for providing funding for the workshops that we observed and in which we participated. Finally, we thank the Notre Dame Department of Physics staff (especially administrative assistants Susan Baxmeyer and Heather Christensen) and physics faculty for hosting and enriching the REU experience.

Extracting Optical Model Parameters for
 $^{116}\text{Sn}(d,d')$ at the 200 MeV

Cathleen Fry

NSF/REU Program

Physics Department, University of Notre Dame

Advisor: Umesh Garg

Abstract

Nuclear incompressibility is an important ingredient of the equation of state of nuclear matter. Isoscalar Giant Monopole Resonance (ISGMR), a compressional mode oscillation of the nucleus, serves as an experimental tool in extracting the nuclear incompressibility of the nucleus. In order to make measurements on the ISGMR strength distributions in the nuclei far from stability, experiments have to be done in the inverse kinematics. This is now made possible with the advent of new radioactive ion beam facilities. ^2H can serve as a target probe in such reactions. However there are no available Optical Model Parameters (OMP) for this probe at the energies required to study ISGMR. With this in mind an experiment was performed with 100 MeV/A ^2H beam at Research Center for Nuclear Physics (RCNP). Elastic scattering data were obtained for ^{116}Sn over a wide range of angles. The OMP extracted from the analysis of these elastic cross-sections are presented.

Introduction

Incompressibility of nuclear matter plays a significant role in defining the equation of state of infinite nuclear matter. It is critical to understanding many nuclear and astrophysical phenomena such as collective excitations and supernova explosions. The Isoscalar Giant Monopole Resonance (ISGMR) provides a way to experimentally determine nuclear incompressibility.

An important term in the determination of incompressibility is the asymmetry term, K_τ , which is associated with $\frac{N-Z}{A}$ [5, 4]. This term is crucial in determining the radii of neutron stars [1]. Radioactive ion beam facilities provide the ability to vary this quantity more using a wider range of isotopes. These experiments must be performed using inverse kinematics.

To preferentially excite the ISGMR, an isoscalar particle, such as ^2H or ^4He must be used. An effective way to do these inverse-kinematics measurements is to employ “active target-TPC” systems (such as MAYA [3]) whereby the constituent gas acts both as the target and the detector. However, pure ^4He is found to be unstable at the high voltages required for the operation of such systems, necessitating addition of some “impurity” gases (typically at 5% level) which creates a lot of background in the final spectra. On the other hand, very little is known about the elastic and inelastic scattering of ^2H particles at the energies (100-200 MeV/A) expected for the rare-isotope beams from facilities like RIKEN (in Japan) and FRIB (in the US). This experiment was performed to study the feasibility of using ^2H as a probe to

study the ISGMR. To analyze this inelastic scattering, optical model parameters must first be obtained. These parameters are extracted from elastic scattering measurements.

In the optical model, the scattering potential is of the form

$$V(r) = U(r) + iW(r) + U_{SO} + iW_{SO} + U_{coul}(r)$$

This analysis uses a hybrid model, where the real central potential is calculated using a single folding model, which treats the incoming deuteron as a point particle and the sums the interaction over the entire target nucleus treated as a two parameter fermi distribution. The imaginary part of the potential is taken to be of the Woods-Saxon form. For both the real and imaginary part of the spin-orbit potential, the Woods-Saxon form is used. The real part describes elastic scattering and the imaginary part accounts for the loss of flux into non-elastic channels. This model is called the optical model because an analogy can be made to light propagation in a semi-transparent medium with a complex index of refraction.

Experiment

The experiment was performed at ring cyclotron facility of the Research Center for Nuclear Physics, Osaka University. ^2H was accelerated to 197 MeV at the ring cyclotron facility. Elastically scattered particles were detected in the high resolution magnetic spectrometer, Grand Raiden, in a focal plane detection system comprised of two position-sensitive multiwire drift chambers

and two scintillators. These are used to make particle identification and reconstruct trajectories using the ion optics of Grand Raiden, instrumental background can be completely eliminated because the scattered particles are focused both horizontally and vertically, as demonstrated in figure 1.

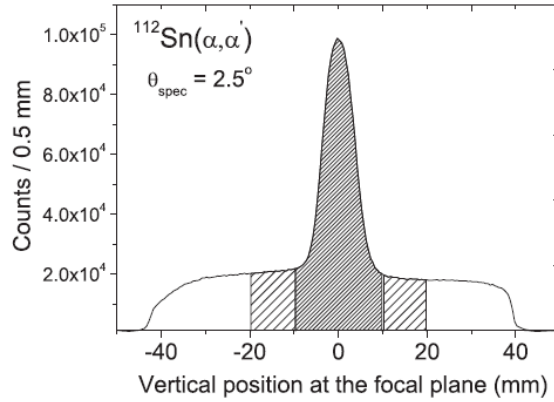


Figure 1: Vertical peak spectrum taken at 2.5° . The central peak is true events plus background and the off center hatched regions represent only background events [5].

Analysis

The potentials were calculated using single folding form factors for the real central potential and a Woods-Saxon form for the imaginary term. Both the real and imaginary spin-orbit potentials are taken to be of the Woods-Saxon form. The single folding form factors were calculated using the programs DOLF and SDOLF. Optical model parameters were then extracted using

	Depth (MeV)	r_0 (fm)	a (fm)
Real central	20.68		
Imaginary central	11.71	1.18	0.543
Real SO	2.26	0.98	0.752
Imaginary spin orbit	0.30	1.05	0.507

ECIS97 [2]. These parameters will then be checked by fitting low lying inelastic scattering states. This procedure will also be performed on targets of ^{58}Ni , ^{90}Zr , and ^{208}Pb .

The fit extracted for the elastic scattering data is shown below in 2.

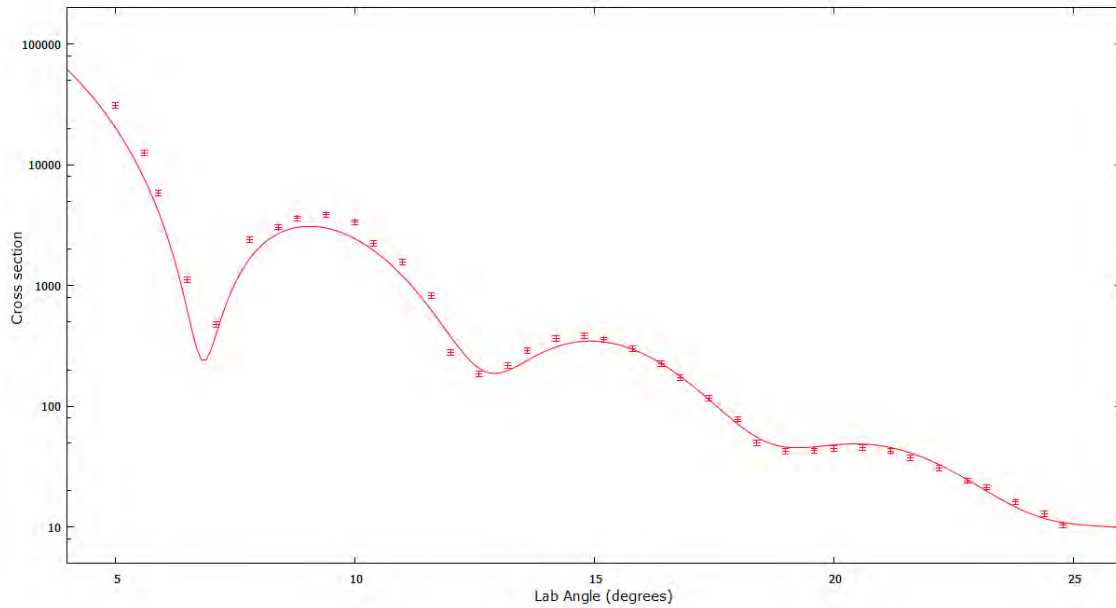


Figure 2: Elastic scattering data and fit with OMP

The preliminary calculations and data for the 2^+ state are presented in

figure 3. Since the shape matches well, we suspect that there is an issue in the normalization factor.

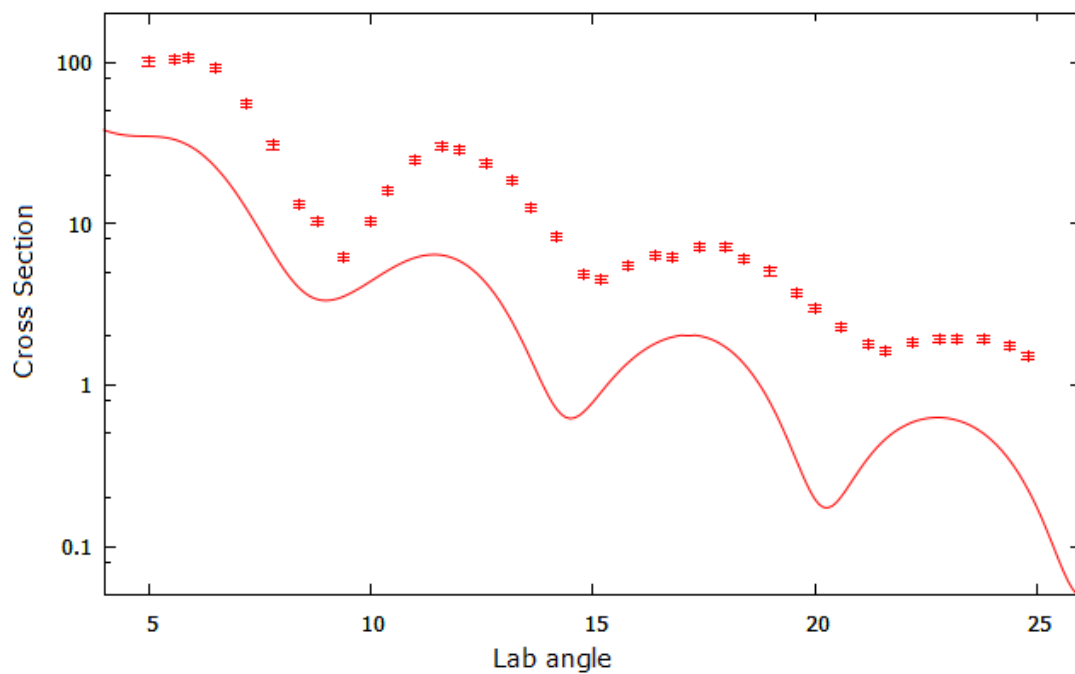


Figure 3: Elastic scattering data and fit with OMP

Acknowledgements

This work was supported in part by the National Science Foundation (Grant No. PHY-1062819). Many thanks to Dr. Garg for coordinating this REU program, being a patient advisor, and providing me with the opportunity to visit RCNP. The physics department of Tennessee Technological University is also acknowledged in helping make this trip possible. I would also like to thank Darshana Patel and James Matta for teaching me how to use the analysis programs and fielding my many questions. Thanks to the whole Notre Dame physics department for hosting this REU program.

References

- [1] J. M. Lattimer and M. Prakash, Phys. Rep. 333, 121 (2000).
- [2] J. Raynal, unpublished
- [3] P.Gangnant, C.Spitaels, G.Fremont, P.Bourgault, J.F.Libin report Ganil 27.2002
- [4] T. Li et al., Phys. Rev. Lett. 99, 162503
- [5] T. Li et al., Phys. Rev. C 81, 034309

Simulations of a Galaxy Model to Probe Outflow Interactions in a Filamentary Structure

Martin Gostisha

2012 NSF/REU Program
Physics Department, University of Notre Dame

Advisor: Dr. Lara Arielle Phillips

Abstract

Filaments are some of the largest known structures in the universe, containing around half of the baryons in the universe and providing scientists with a fossil record of galaxy evolution. Large-scale simulations done in the past have successfully reproduced the broad characteristics of this cosmic, filamentary web. We look to improve upon this by looking at interactions between galaxies and the filament by implementing collimated galactic outflows and other ejecta in this environment. Looking at mass interactions between the galaxies and the intergalactic medium (IGM) when the galactic outflows are collimated and the galaxies have a preferred orientation is crucial to gaining a clearer picture of the enrichment history of these filaments. Once completed, this study will improve upon our knowledge of the circulation of baryons in the IGM, a poorly understood phenomenon in cosmology.

To set up this simulation, the sample galaxy that we embed in a filamentary environment must be detailed enough so that we are able to probe outflow interactions, but not overly intricate, as this would introduce too much computational overhead into the simulation. More focus was placed on the mass exchanges of the galaxy, rather than the galaxy itself, as it is not as important to what is to be studied. The galaxy will next be placed in the filamentary environment, and the mass outflows will be tracked to understand help to understand how interactions occur in this environment.

Introduction

Large-scale simulations done in the past have modeled galaxies as clumps of dark matter, mainly with spherical outflows. The galaxies are formed when the dark matter particles reach the Jeans density and then are able to start collapsing to form galaxies. If the simulation has high enough resolution, some stellar particles can be formed via similar processes. The feedback from the galaxies in these simulations is in the form of spherical outflows from the galaxies, rather than collimated outflows that have been discovered in observational studies recently. Our study aims to look not at the galaxies themselves, but rather study the interactions of collimated outflows from galaxies with preferred orientations. Looking at collimated outflows allows us to more precisely study just where the mass leaving the galaxy is going and what type of interactions is involved when it is ejected.

Galaxy Parameters

The parameters of the galaxy itself were not overly important due to the nature of our study, which is looking at mass interactions outside of the galaxy itself. With this being said, the shape and mass were the most important features of the sample galaxy. We assumed a mass of $3 \times 10^{12} M_{\odot}$ inside of a spherical galaxy with a radius of 15 kpc. Since the mass distribution inside the galaxy itself is not crucial to the study, we assumed that the galaxy had a uniform density throughout. When the galaxy is placed into a filamentary environment, it will accumulate matter via gravitational inflow from the mass in the environment. Since the environment surrounding the galaxy while it is in development has no matter, there is no mass

inflow into the galaxy. To compensate for this, we added an inflow stream to regulate the new mass change. The inflow is assumed to inject mass into the galaxy at a rate of $100\text{-}200 M_{\odot} \text{ yr}^{-1}$. The above parameters are generally in agreement with the properties of IRAS 13120-5453 [2].

Simulation Parameters

The sample galaxy created for this study, as described above, needed to be put into some sort of environment to track mass flows. To the development of the simulation, the galaxy was put into a 10^6 kpc^3 box. The simulation allowed for 1 kpc spatial resolution, giving the environment 1,000,000 cubic elements. The galaxy was placed at the center of the box, which had no external matter added to it. Simulation of the mass flows was done over a 100 Myr timescale, with time steps of 5 Myr, creating 20 individual simulation steps. In each step, a new inflow element was added and distributed throughout the galaxy and collimated, central outflows as well as supernova driven outflows were calculated. The outflow processes are described below.

Collimated Outflows

The characteristics for the AGN-driven collimated outflows were taken from both past theoretical and observational studies of galaxies at low redshift. A recent study by Martin et. al. looking at the physical properties of gas inflows at outflows of galaxies in the redshift region $0.4 < z < 1.4$ [1] as well as a paper by Sturm et. al. studying massive molecular outflows in ultra luminous infrared galaxies (ULIRGs)

[2] was used to determine the properties of the collimated outflows in our simulation. Martin et. al. found a correlation between the velocity of the outflows and the opening angle of the outflows, stating that higher velocities of outflows showed smaller opening angles than the outflow possessed. Although they did not give a direct relation between the velocity and the opening angle, this was important when altering the outflow parameters for our simulation. Using the properties of IRAS 13120-5453 mentioned above, we assume the velocity of the ejected material associated with the collimated outflow matter to be 600 km s^{-1} . The opening half-angle is then set to 12° , and changes linearly with the velocity, increasing by 4° for every 100 km s^{-1} decrease in outflow velocity. This relation between opening angle and velocity is purely an assumption, Martin et al. only said that they see a relation in their observational data and did not give a mathematical relation [1]. To simplify the complicated structure of the observed collimated outflows for the simulation, four jets of material are ejected from the galaxy instead of a solid conic outflow, where the outflow mass is distributed evenly between the four jets. The outflow rate was assumed to be $130 M_\odot \text{ yr}^{-1}$, in agreement with that of the outflow rate of IRAS 13120-5453 observed by Sturm et. al.

Supernova Driven Outflows

Supernova driven outflows, while not as dominant as collimated outflows, still eject mass from the galaxy at a significant rate. The supernova driven outflows are modeled by picking a point inside the confines of the galaxy, and blowing a randomly chosen mass between $1-6 M_\odot$ evenly into the 26 bins surrounding the

location of the SN. The rate at which supernovae explode was assumed to once every 100 years. While the mass in the simulated galaxy was evenly distributed, the location of the supernova explosion was still assumed to happen in the “disk” region 95% of the time, as this more accurately models the ratio of the location of supernova explosions in a typical galaxy. Other than this constraint, the location of the supernova explosions was randomly selected. Since the ejected mass from the supernova would only add a negligible amount of mass to the interior mass of the galaxy, only supernova explosions that happened at the edge of the galaxy, therefore blowing mass outside of the galaxy, were studied.

Results

The initial results of the outflows leaving the galaxy are shown in Figures 1 and 2 (below). Figure one shows the collimated outflows at velocity $v=600 \text{ km s}^{-1}$ and opening angle $\theta=12^\circ$. Figure 2 shows the same galaxy, but with slower outflows ($v=300 \text{ km s}^{-1}$) resulting in an increased opening angle ($\theta=24^\circ$). The two plots show the differences in where the material goes when leaving the galaxy as the velocity of the outflow decreases.

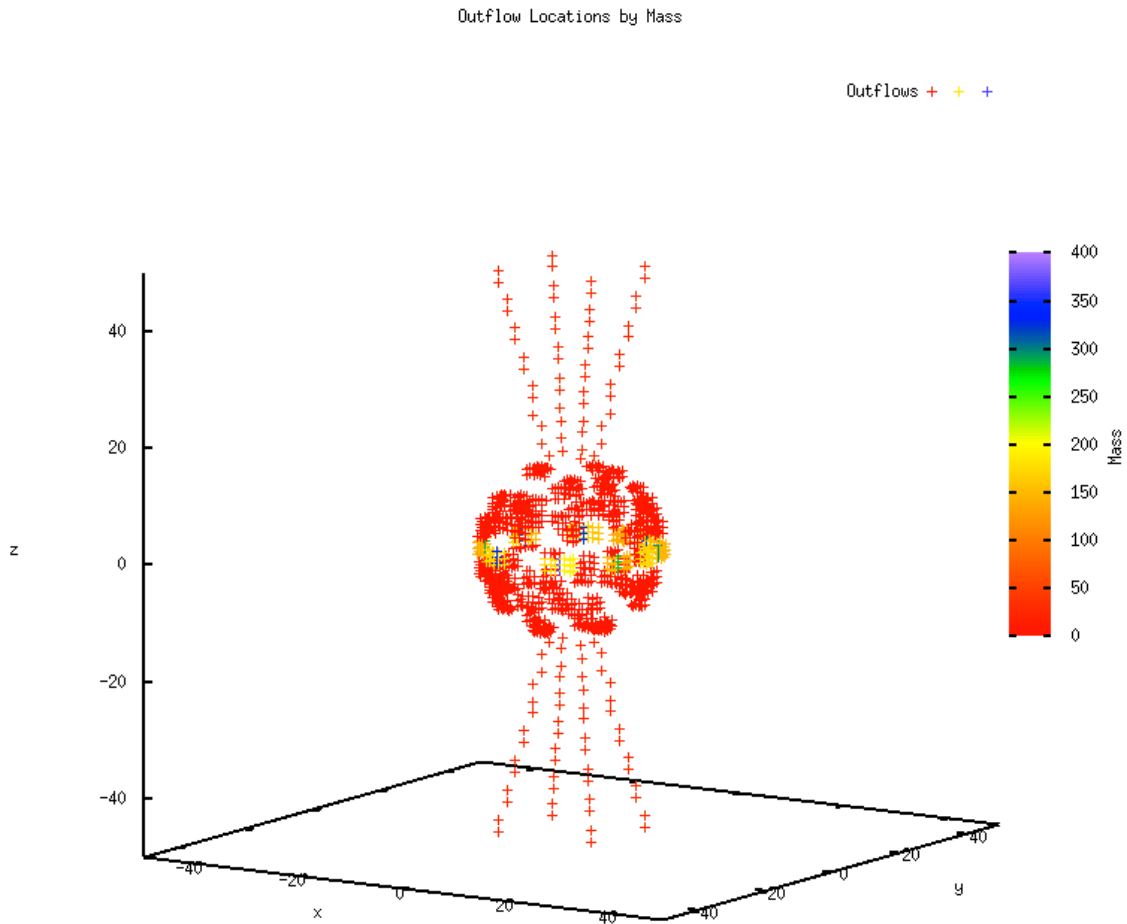


Figure 1. - The figure shows only the mass outside of the galaxy. This galaxy has collimated outflows with velocity $v=600 \text{ km s}^{-1}$ and an opening angle $\theta=12^\circ$.

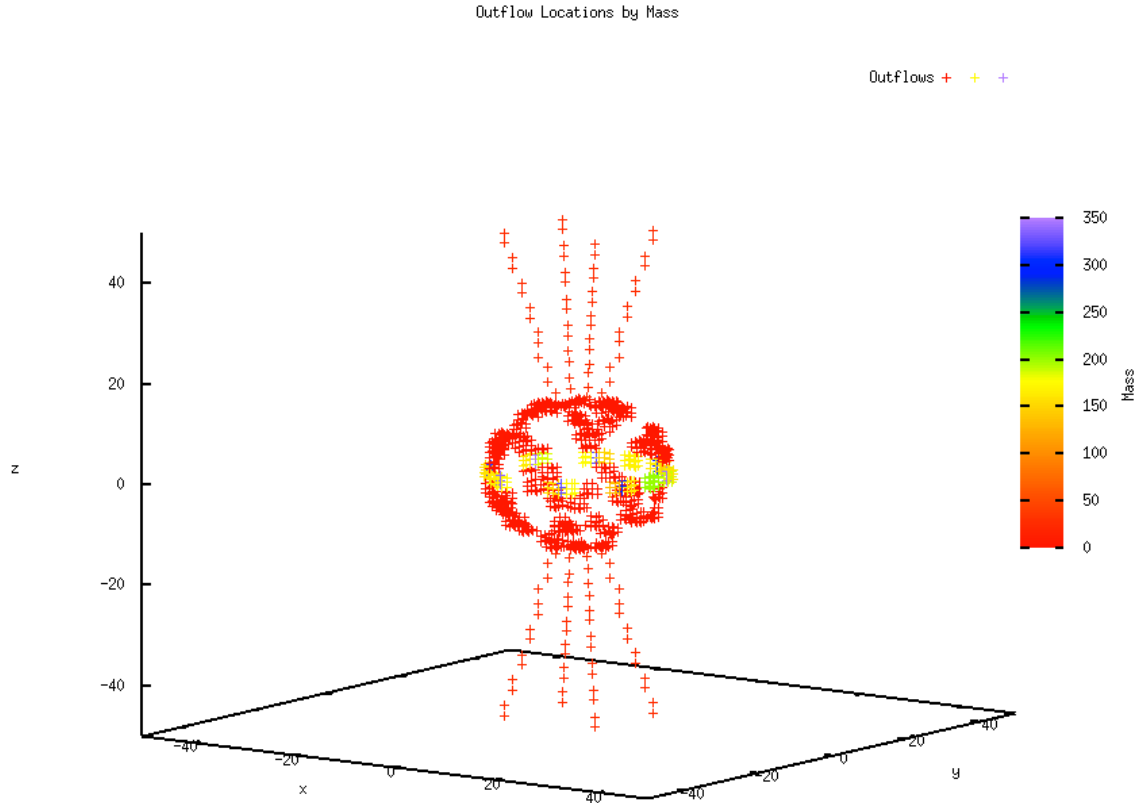


Figure 2. – This figure is the same as Figure 1, but with the collimated outflows at a velocity $v=300$ km s^{-1} and opening angle $\theta=24^\circ$.

Conclusions

The fact that this study is in its infancy means that there is a lot of work to be done before meaningful conclusions can be made about how different outflows from galaxies effect the enrichment of the large-scale environment it is located in. The first major addition to the sample galaxy will be more accurate collimated outflows. This will include filling a complete region entrained within the outflow instead of modeling it using four jets of material at the edge of the outflow. In addition, a more concrete relation between outflow velocity and opening angle will increase the

accuracy of where this baryonic matter goes once it has escaped the galaxy. A mechanism also needs to be added by which the material from the outflow is interacting with the rest of the filamentary environment and therefore will slow down as it gets further away from its host galaxy. The supernova driven outflows are currently static once they occur, meaning that they don't move away from the galaxy once they explode. This is another big step to add to the simulation to increase the accuracy pertaining to where the matter goes after leaving the host galaxy. Energetics of the different outflows are also not accounted for in the simulation, and looking at the energy injected into the environment by these outflows will be important to revealing other processes occur when mass with significant kinetic energy is expelled from a galaxy. Lastly, once the galaxy is ready to be placed into a filamentary environment, results of the broad study about mass interactions in this environment will be ready to be analyzed.

Using a Theoretical Model for the Energy of Ice VI and VII

Jordan Hernandez

2012 NSF/REU Project

Department of Physics

University of Notre Dame

Advisor: Dr. Kathie E. Newman

Abstract

Solid water, ice, is found in at least ten different crystalline forms as a function of temperature and pressure. My research was to study the transition between Ice VI and Ice VII, building upon a former REU student's framework and the Stillinger-Weber model of Monoatomic water, developed by Molinero and Moore. The previous student, Dawn King, had shown that the experimental Ice VI and VII crystalline structures could be represented on one lattice structure, the "King" lattice. Using this lattice I used the Stillinger-Weber model to calculate the energy of the two forms of ice. I explored how the energy changed as a function of internal parameters, but was unsuccessful in finding believable trends when the dimensions of the unit cell were varied. Further work needs to be done on the ability to do statistical calculations by using the Monte Carlo simulation.

1. Introduction

Ice exist in at least 10 different crystalline forms. The basis of this research was to find out, in general, more about the process in when ice goes from one state to the other by varying the temperature or the pressure. After I mastered the basic condensed matter concepts (e.g., Lennard-Jones potential, Bravais lattice and basis, Space groups...), then the real challenge came as to find out why and how Ice VI goes to Ice VII just by raising the pressure. Both Ice VI and VII are self-clathrate, meaning that there are sub-lattices within the crystal structure which penetrate each other but never touch. Using Dawn King's framework of both Ice forms I can, by using Fortran, study the energetics of both forms.

- 1) There is precisely one hydrogen atom on each hydrogen bond.
- 2) There are precisely two hydrogen atoms near each oxygen atom.

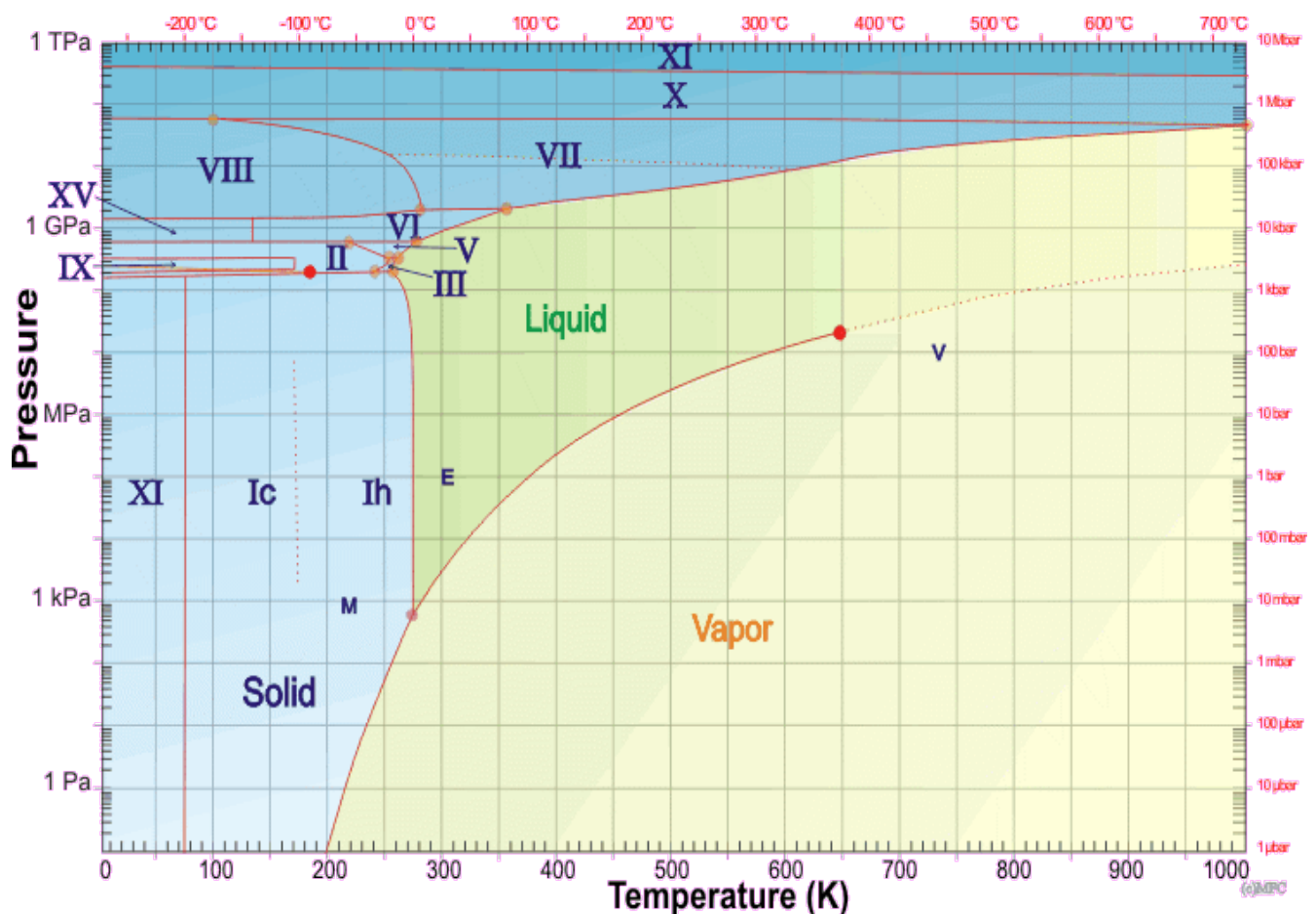


Figure 1: A phase diagram of water. There are at least 16 known states of solid states. “E”, “M”, and “V” represent the standard temperature and pressure of Earth, Mars, and Venus. [3]

2. The King Model for the Ice VI and VII Structures

King noticed that it was possible to represent Ice VI and VII (see Figs. 2 and 3, respectively) on one underlying lattice of $4 \times 4 \times 8$ points. Two unit cells of Ice VI fit on this lattice, compared with 1 unit cell for Ice VII. Each water molecule is represented by a point; in Fig. 2, there are 20 molecules, compared with 16 in Ice VI.

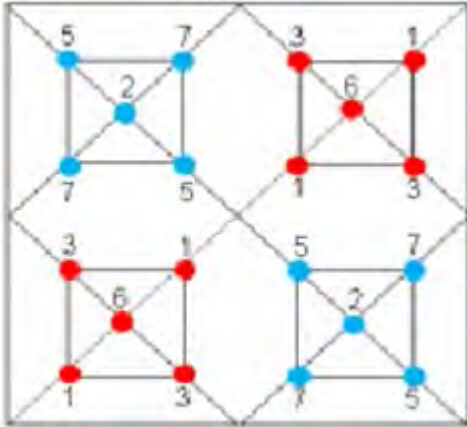


Figure 2: Is a projection on the xy -plane, of possible Ice VI configurations. The number represents the heights in z -axis on a scale of $c/8$. Each configurations has 4 degenerate states and 4 nearest-neighbors.

Ice VI has two distinguishable groups that never touch each other but penetrate each other along the xy axis, and form chains along the z -axis. The lattice unit cell of Ice VI is a body-centered tetragonal (bct) Bravais lattice with dimensions $a = 6.27 \pm 0.01 \text{ \AA}$ and $c = 5.79 \pm 0.01 \text{ \AA}$.

Ice VII, like Ice VI, has two distinct groups that never touch; but instead of being separated on the xy -plane they overlap each other into one, periodic, lattice structure. It has a face-centered cubic (fcc) Bravais lattice of dimensions $a = 3.30$

$\pm 0.01 \text{ \AA}$. It is the fact that we do not know why, when adding pressure, Ice VI goes into this unique form that is Ice VII, which drives the basis of this research.

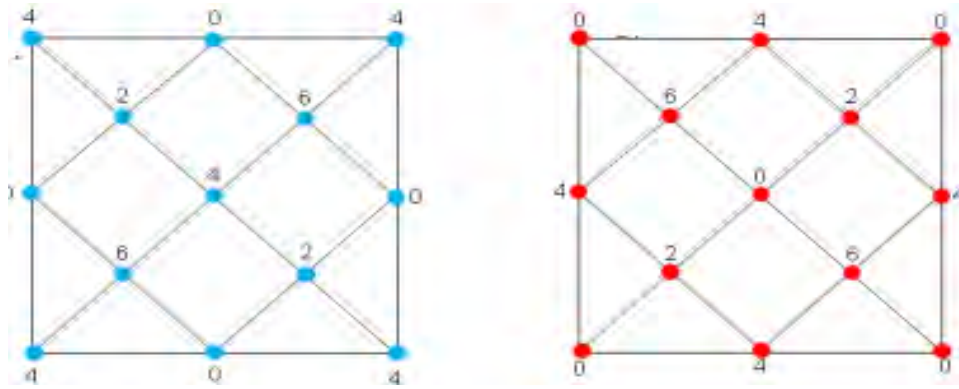


Figure: 3 shows the two groups that overlap each other but never touch (self-clathrate). This is a projection of the sub-lattices on the xy-plane. The numbers represent the heights on the z-axis on a scale of $c/8$.

3. The Energy

The SW potential was developed for semiconductors with tetrahedral bonding.

It contains both 2- and 3-body terms, where λ is a parameter that tunes the tetrahedral penalty.

Molinero and Moore realized that ice networks could be understood in terms of tetrahedral bonding and adapted the SW potential for “Monoatomic Water.” Their model represents water molecules as points, as was done by Dawn King for the King lattice.

$$E = \sum_i \sum_{j>i} \varphi_2(r_{ij}) + \sum_i \sum_{j \neq i} \sum_{k>j} \varphi_3(r_{ij}, r_{ik}, \theta_{ijk})$$

$$\varphi_2(r) = A\epsilon \left[B \left(\frac{\sigma}{r} \right)^p - \left(\frac{\sigma}{r} \right)^q \right] \exp\left(\frac{\sigma}{r - a\sigma} \right)$$

$$\varphi_3(r, s, \theta) = \lambda\epsilon [\cos \theta - \cos \theta_0]^2 \exp\left(\frac{\gamma\sigma}{r - a\sigma} \right) \exp\left(\frac{\gamma\sigma}{s - a\sigma} \right)$$

The equation above represents the Stillinger-Weber Potential [2], where λ is a parameter that tunes the tetrahedral penalty. In other words, the higher lambda is, the more tetrahedral the structure is. The Stillinger-Weber potential is great to use when wanting to apply the Monte Carlo simulation between Si-Ge phase transition[4]. Now we want to take this potential and try to apply the same Monte Carlo simulation to this phase transition, but first the potential must be compared to experimental results.

Ice VI		Ice VII	
A	B	A	B
a: $[\frac{1}{2} \frac{1}{2} \frac{1}{2}]$	a: $[0 \ 0 \ 0]$	a: $[0 \ 0 \ 0]$	a: $[\frac{1}{2} \frac{1}{2} \frac{1}{2}]$
disappears	disappears	d: $[\frac{1}{2} \frac{1}{2} 0]$ $[0 \frac{1}{2} \frac{1}{2}]$ $[\frac{1}{2} 0 \frac{1}{2}]$	d: $[00 \frac{1}{2}]$ $[\frac{1}{2} 00]$ $[0 \frac{1}{2} 0]$
g: $[\frac{1}{2}, \frac{1}{2} + x, \frac{1}{2} + \bar{z}]$ $[\frac{1}{2}, \frac{1}{2} + \bar{x}, \frac{1}{2} + \bar{z}]$ $[\frac{1}{2} + x, \frac{1}{2}, \frac{1}{2} + z]$ $[\frac{1}{2} + \bar{x}, \frac{1}{2}, \frac{1}{2} + z]$		b: $[\frac{1}{4} \frac{1}{4} \frac{1}{4}]$ $[\frac{3}{4}, \frac{3}{4}, \frac{1}{4}]$ $[\frac{3}{4}, \frac{1}{4}, \frac{3}{4}]$ $[\frac{1}{4}, \frac{3}{4}, \frac{3}{4}]$	
	$[0 \ x \ z]$ $[0 \ \bar{x} \ z]$ $[x \ 0 \ \bar{z}]$ $[\bar{x} \ 0 \ \bar{z}]$		c: $[\frac{3}{4} \frac{3}{4} \frac{3}{4}]$ $[\frac{1}{4} \frac{1}{4} \frac{3}{4}]$ $[\frac{1}{4} \frac{3}{4} \frac{1}{4}]$ $[\frac{3}{4} \frac{1}{4} \frac{1}{4}]$

Table I: Space group positions for Ice VI and Ice VII. The units are (a,a,c) for body-centered tetragonal VI and (a,a,a) for face-centered cubic VII and internal parameters $x=0.21$ and $z=-0.1$.

4. Results

Using Dawn's Model we set up the structure, using Fortran, and calculate the nearest-neighbor energies using the Stillinger-Weber model.

For Ice VI we hold 'a' and 'c' constant at values:

$$a = 8.87 \text{ Angstroms [1]}$$

$$c = 5.79 \text{ Angstroms [1]}$$

then we vary 'x' and 'z' to obtain the values, **Fig. 5 and Fig.6**, which give the minimum energy (these are the values you see in the caption of Figure 4).

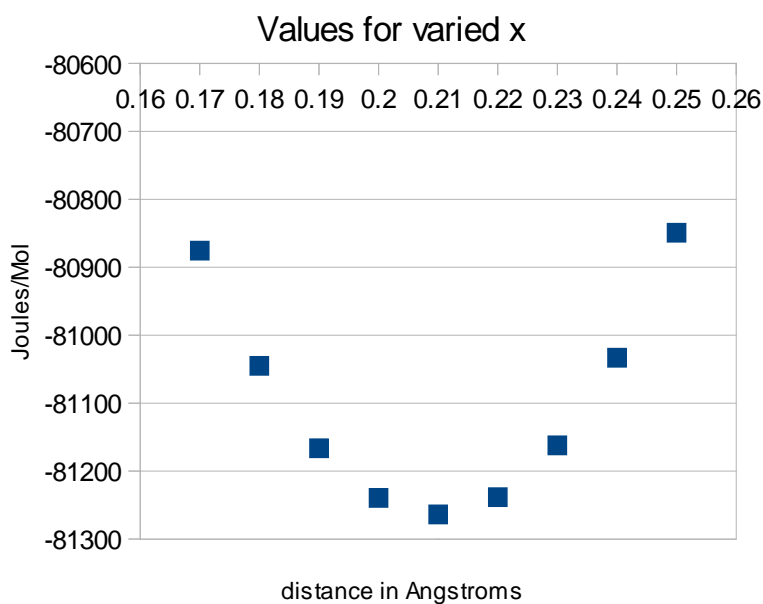
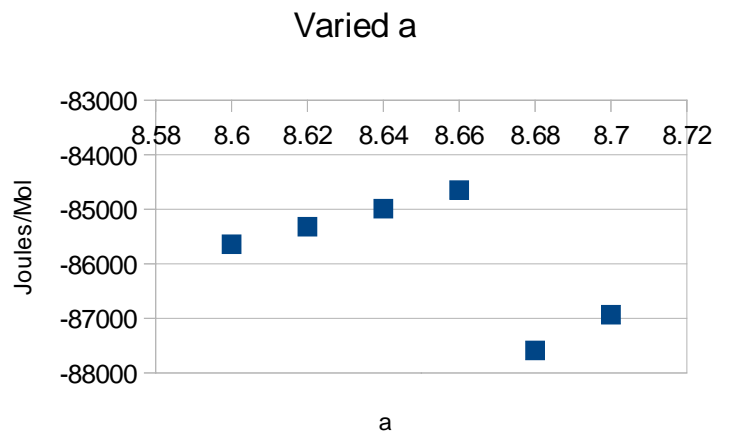
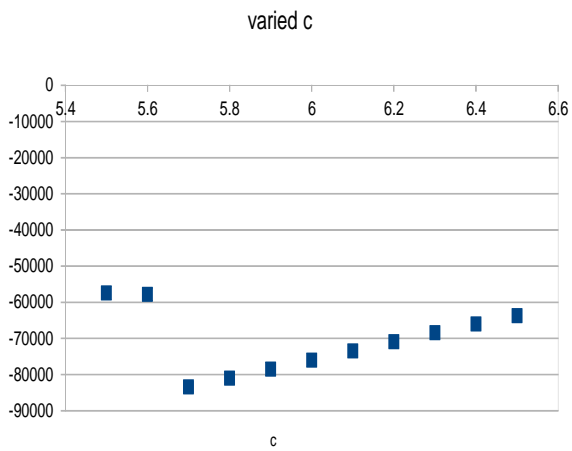
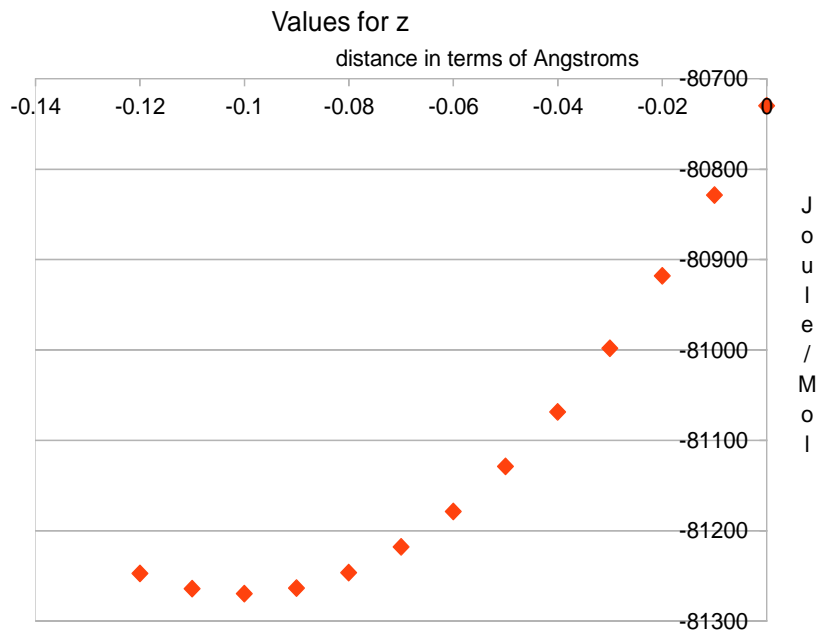


Figure 5: The Graph shows the Minimum of the internal parameter 'x' value found by the Stillinger-Weber Model.



Is there a mistake in the Fortran code? Or are we seeing a limitation in the Stillinger-Weber model for ice? Without knowing the answer to these questions, we cannot determine whether this model works for these structures and whether future researcher can use the Monte Carlo method to study trajectories and see how the Ice VI structure changes to Ice VII.

[1] http://physics.nd.edu/assets/25212/king_dawn_modeling_phase_trans.pdf

[2] V. Molinero and E.B. Moore, "Water Modeled As an Intermediate Element between Carbon and Silicon," J.Phys. Chem B113, 4008-4016 (2009).

[3] <http://www.btinternet.com/~martin.chaplin/phase.html> .

[4] M. Laradji and D.P. Landau, "Structural Properties of Si, Ge alloys: A Monte Carlo simulation with the Stillinger-Weber potential," Phy. Rev. B 51,8 (1995).

References

- [1] Martin, C. L., Shapely, A. E., et al. 2012
- [2] Sturm, E., et al. 2011, ApJ, 733, L16+

Project GRAND

Cedric Hill

2012 NSF/REU Program
Physics Department, University of Notre Dame

Advisor: Dr. John Poirier

Abstract

Project GRAND is an extensive air shower array of proportional wire chambers. It has 64 stations in a 100m x 100m area; each station has eight planes of proportional wire chambers with a 50 mm steel absorber plate above the bottom two planes. This arrangement of planes, each 1.25 square meters of area, allow an angular measurement for each track to 0.25 degrees in each of two projections. The steel absorber plate allows a measurement of the identity of each muon track to 96% accuracy. Two data-taking triggers allow data to be simultaneously taken for extensive air showers (multiple coincidence station hits) at about 1 Hz and single muons (single tracks of identified muons) at 2000 Hz. This summer, I used data from Project GRAND to look at a few gamma ray burst events, as well as forbush decreases.

Cosmic ray astrophysics investigates particles (or rays) that arrive at the earth's surface from the sun and beyond. Project GRAND is an extensive detector array which studies these rays in two energy bands depending on the trigger selected: the primary band (solar), from 30 to 300 GeV and secondary band (extrasolar), from 100 to 100 000 TeV. The original goal of this array is to study stellar point sources of gamma rays with sub-second precision. This study requires: good angular resolution, good particle identification, and sufficient running time to gather statistics. This project has pioneered the use of tracking detectors (proportional wire chambers) in cosmic ray research; tracking detectors have the advantage of providing superior angular resolution and instantaneous particle identification. These PWC tracking detectors are ideal for studying our latest research goals: to look for the highest-energy particles generated by our Sun. The GRAND array is located in a 100 m x 100 m field adjacent to the Notre Dame campus at 222 m elevation, 86° W and 42° N. The 64 stations are arranged in an 8 x 8 grid with 14 m separation between stations. The electronics trailer at the center of the field is a former astronaut debriefing and isolation chamber, and was obtained from NASA government surplus. The southwest quadrant was the first constructed; these stations were placed 0.6 m into the ground for natural cooling in the summer. The cooling works well, but moisture problems suggested the placement of the remainder of the array above ground with added insulation. Each station is enclosed by a 2.4 m x 2.4 m x 0.9 m high hut. Inside are eight planes of proportional wire chambers (PWCs) and a 50 mm thick steel absorber plate. The chambers have been surveyed to a precision of 0.1 deg. The temperature of the huts is controlled with heaters to keep them > 17 deg C in the winter; dehumidifiers control the humidity < 55%. The eight planes are arranged in xy

pairs; the pairs are separated vertically by 200 mm and are 1.2 sq-m in area. The top three pairs measure the xz and yz angle of the track; the pair below the 50 mm steel absorber plate are used for muon identification. Muons are distinguished from electrons by demanding that a muon track be single hits in each of the 3 pairs above the steel plus the pair below, all of which are aligned. This simple algorithm is 96% accurate for muons. Muon identification is performed for each track.

George Charpak received the Nobel prize for inventing the PWC detector which is used extensively in other fields of physics and medicine; Project GRAND has pioneered its adaptation for cosmic ray arrays. Construction design utilizes mass production techniques to economically manufacture precision detectors. The cells in each plane are 14 mm wide and 1100 mm long separated 9.5 mm from the high voltage planes. The PWCs are filled with a gas mixture of 80% argon and 20% carbon dioxide and operate at 2600 V. The huts contain 8 PWC planes. A plane has 80 cells; each cell has an amplifier, shift register memory, and summer whose outputs are used for coincidence input to form a self-trigger for the station. A station trigger causes the status of its 640 cells to be stored in local shift register memory. The trigger is comprised of an x-OR-y signal from each pair of planes; the top 3 PWC pair of signals are placed in 3-fold coincidence. This 3-fold coincidence records over 99% of the cosmic ray tracks and introduces < 1% noise.

The trailer receives a timing signal from each hut which triggered on a track. A coincidence circuit is set for N simultaneous huts, where N can be set to 1, 2, 3, etc. A coincidence causes a train of clock pulses to be sent to all the stations which clocks the data serially from their shift register memory to the trailer. The data from all the stations are read out to the online computer in the trailer in a total of 70 microseconds. The time

of the trigger, accurate to 1 millisecond, is recorded along with the rest of the trigger's data. The data acquisition system "computer" records the data. There is a single muon trigger (lower energy band). The search for one-and-only-one-hit pattern in each of the 8 planes of a station; the successful wire coordinates are stored in memory. The computer stores 900 tracks in memory and then writes them to a disk. Single muon data are stored at a rate of 960 muons per sec; each disk holds several months of data. With $N=3$ shower data (higher energy band), the data acquisition system takes data for cosmic ray showers.

One of the things that we focused on this summer were gamma ray bursts, or GRB's. Gamma ray bursts are flashes of gamma rays associated with extremely energetic explosions that have been observed in distant galaxies. They are the brightest electromagnetic event known to occur in the universe and the most powerful explosions since the Big Bang. Now, satellites detect about one per day. It is unknown what causes gamma ray bursts but it is believed that they are associated with supernovae. One burst releases more energy than the sun will in its entire life. The initial burst of gamma rays is followed by slowly fading emission at longer wavelengths created by collisions between the burst ejecta and interstellar gas. This fading emission is called the afterglow. Early searches for this afterglow were unsuccessful, largely due to the difficulties in observing a burst's position at longer wavelengths immediately after the initial burst. When we talk about gamma ray bursts, we classify them as long bursts or short bursts. Long bursts, which are greater than 2 seconds, constitute the majority of the population and have the brightest afterglows. Most long bursts have been linked to a galaxy with rapid formation associating them with the deaths of massive stars. These are lower energy events and are also studied more. A unique gamma ray burst was seen on March 28, 2011. The burst

lasted more than two and a half months and originated from a small galaxy at redshift $z = 0.3534$. The event is interpreted as a supermassive black hole devouring a star and emitting its beams of radiation towards Earth. It was in the center of a small galaxy in the Draco constellation, which is 3.8 billion light years away. It was caused by the tidal disruption of a roughly solar-mass star and probably came when a star wandered too close to the central black hole in the galaxy, and was gravitationally torn apart and swallowed by it. Timing considerations suggest that it was a white dwarf. Short bursts, which are less than 2 seconds, with a mean duration of 0.2 seconds, account for 30% of gamma ray bursts. These are higher energy events and have no links to massive stars or supernovae. The true nature of these events remain unknown although it has been hypothesized that they originate from the mergers of binary neutron stars (neutron stars with a black hole). The mean duration suggests a source of very small physical diameter in stellar terms (less than 0.2 light seconds or 5% of the sun's diameter). This suggests a very compact object as the source. A small fraction of short gamma ray bursts are probably produced by giant flares from soft gamma repeaters in nearby galaxies. We had a list of 7 gamma ray bursts that we wanted to study, which were gathered by former REU student Sarah Krug. She got these events from the Swift (a mission that finds hundreds of flashes each year; three telescopes study each burst from start to finish looking for their origin) website and she also recorded right ascension, declination, and time for the events. Then she wrote a program that told her if it was visible in Grand's 63 degree viewing angle. We wanted to analyze these events this summer to search for coincidences between the time and angle-position of each of these bursts. Our search strategy was to start with events of short duration (higher energy), high fluence (brightness), and angles within our viewing

cone. We want to get everything 'right' on the first look, see if we get a coincidence of S/dS greater than or equal to 3 sigma (Signal/error-on-signal) and stop there if true. If not, go to 2nd best event and if the two together are greater than or equal to 3 sigma, stop there, etc. through the 7th event. Our problem was the timing. When dealing with such short events, we needed to be able to measure seconds as accurately as milliseconds. We had a clock that coincides with WWVB in Colorado and absolutely accurate with hours, minutes and seconds and we have a megahertz clock that is accurate to milliseconds but its starting point is arbitrary. So we were trying to find a way to match up these two clocks but this problem proved to be tougher than we anticipated and we were not able to get results from it.

Another thing that we wanted to study was Forbush decreases. A Forbush decrease is a sudden drop or rapid decrease in the cosmic ray intensity following a coronal mass ejection. It occurs due to the magnetic field of the plasma solar wind sweeping some of the galactic cosmic rays away from Earth. Scott Forbush was an American physicist who studied cosmic rays in the 1930s and 1940s. Forbush decreases reach Earth within a few days after the coronal mass ejection, and the decrease takes place over the course of a few hours. Over the following several days, the solar cosmic ray intensity gradually returns to normal. A coronal mass ejection is a massive burst of solar wind and magnetic fields rising above the solar corona or being released into space. Coronal mass ejections release huge quantities of matter and electromagnetic radiation into space above the sun's surface, either near the corona or farther into the planet system or beyond. The ejected material is a plasma consisting primarily of electrons and protons. The plasma released by the CME blocks cosmic rays from reaching Earth and that is what causes the decrease

in the data. The magnitude of a Forbush decrease depends on the size of the coronal mass ejection, the strength of the magnetic fields in the coronal mass ejection, the proximity of the coronal mass ejection to the Earth. A Forbush decrease is sometimes defined as being a decrease of at least 10% of galactic cosmic rays on Earth, but ranges from about 3% to 20%. Recently, there were two solar flares that showed a Forbush decrease in our data. An X1.4 class solar flare occurred on July 13, 2012. NASA recorded the velocity of the coronal mass ejection at 850 miles per second (3,060,000 miles per hour). Given that the sun is 93 million miles away, it took the CME about 1.3 days to get here. NASA predicted it to arrive around 9:00 UTC on July 14 +/- 7 hours. There is a plot for this data shown in Figure 1. Another solar flare, M7.7 class, occurred on July 19, 2012. The SOHO satellite recorded the velocity of the coronal mass ejection at greater than 2 million miles per hour. This tells us that it took about 1.9375 days for us to see the effect on earth. There is a plot for this data shown in Figure 2. A Forbush decrease can be clearly seen in these plots.

Some things that can be done to expand on this summers work are finishing the gamma ray burst analysis as well as looking at the Forbush decrease problem and doing more. The gamma ray burst analysis is very formidable if the time problem can be figured out. If provided the opportunity to work on it again, I will definitely try to figure it out. Also, it would be a very good idea to expand on the Forbush decrease study. It would be a good idea to compare our data with Oulu's neutron monitor and see how fast the data falls and how slowly it recovers. The change in the average direction of the muons, which is an effect caused by the magnetic field that bends it, would be something interesting to look at.

Figure 1:

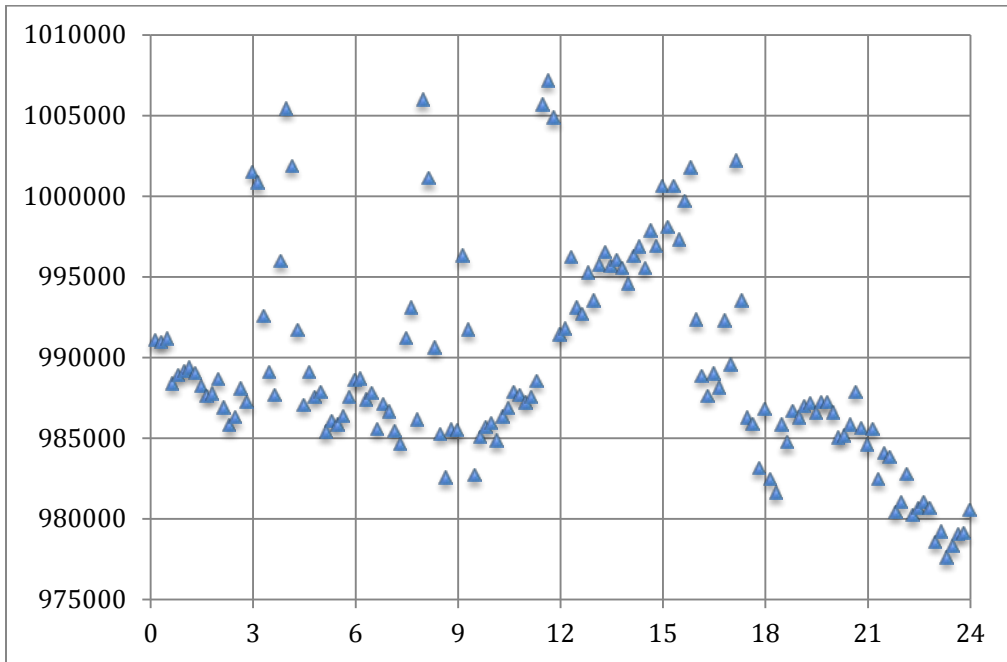
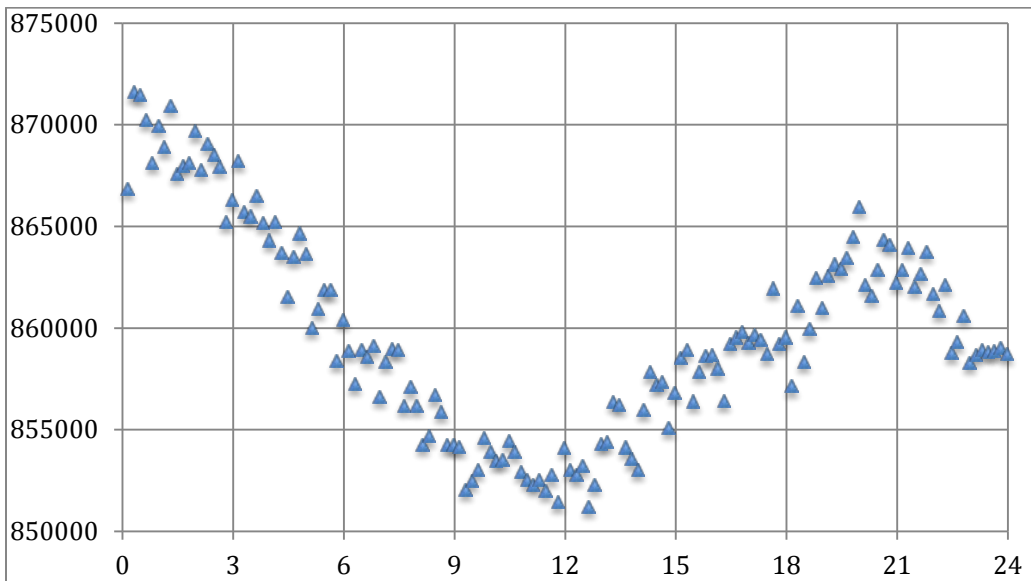


Figure 2:



References

Catanach, Tom. "Atmospheric Corrections and Periodic Variations at Project GRAND."

Scientia. Vol. 3. Spring 2012.

Fox, Karen. "The Sun Erupts: Natural Hazards." NASA Earth Observatory. July, 14,

2012. <http://earthobservatory.nasa.gov/NaturalHazards/view.php?id=78540>

nd.edu/~grand/

Poirier, John. "Status Report on Project GRAND." *32nd International Cosmic Ray*

Conference, Beijing 2011.

Small-Angle Neutron Scattering (SANS) Studies of Superconducting UPt₃'s Vortice Lattice

Joseph Hlevyack

2012 NSF/REU Program

Physics Department, University of Notre Dame

Advisor:

Morten R. Eskildsen, Ph.D.

Graduate Student Collaborators:

William Gannon

Catherine Rastovski

Pinaki Das, Ph.D.

Abstract

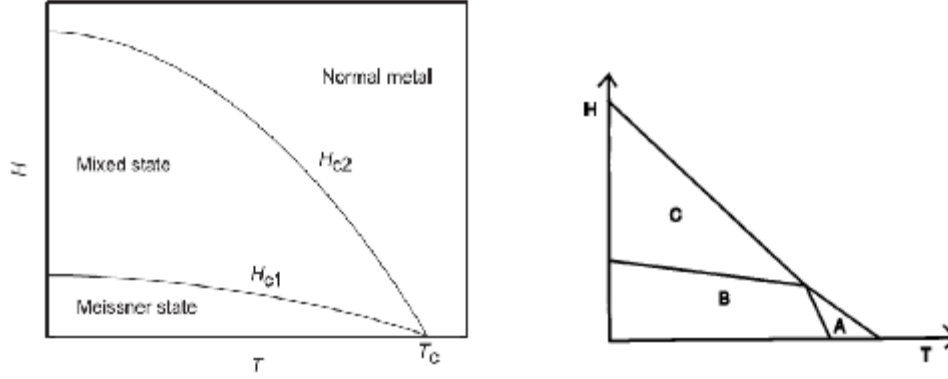
UPt₃ is a type-II, heavy-fermion superconductor characterized by a mixed state threaded with vortices that each carry quantized magnetic flux. Using Small-Angle Neutron Scattering (SANS) experiments, the vortex lattice (VL) was analyzed at various applied magnetic fields and temperatures, including settings in the C and A phases of the $H-T$ diagram. In particular, the temperature dependence of the form factor—the Fourier transform of the magnetic flux modulation—was closely analyzed, and comparisons between two experiments indicate that the form-factor results were reproducible. The experiments also resolved a question about the existence of a new superconducting state existing in the multi-phase $H-T$ diagram.

1 Introduction

Superconductors are materials that have a virtually zero electrical resistance below some critical temperature,¹ which can range from a few mK to over 100 K. Since zero electrical resistance means no energy dissipation via heat, superconductors are promising technologically in electrical circuits. Yet, our understanding of superconductors is far from complete, and studying superconductors with low critical temperatures is important to better understand the superconducting state.

Superconductors are divided into two classes: type-I and type-II. Type-I superconductors are exclusively characterized by the Meissner effect, where below a critical temperature T_c and applied magnetic field H_{c1} , the superconductor completely expels the applied field. Type-II superconductors, on the other hand, are characterized by two states: the Meissner state and the “mixed” state. The mixed state is bounded by two critical magnetic fields H_{c1} and H_{c2} , below which the Meissner state exists and above which the normal state appears. See Fig. 1(a). The mixed state’s hallmarks are the penetration of the bulk by flux-lines or vortices—whirlpools of supercurrents—that each carry quantized magnetic flux. One quantum of magnetic flux is $\phi_0 = 2070 \text{ T}\cdot\text{nm}^2$.

¹Once this critical temperature is reached, there is also some critical applied magnetic field below which the superconducting state can exist.



(a) For a general type-II superconductor [1].

(b) For UPt_3 [2].

Figure 1: Schematic $H - T$ (Applied Magnetic Field Versus Temperature) state diagrams.

UPt_3 is a heavy-fermion superconductor characterized by three superconducting phases termed A , B , and C ; these three phases meet at a *tetracritical* point in the $H - T$ phase diagram as in Fig. 1(b). Huxley et.al. [3] studied how UPt_3 's flux-line lattice is oriented with increasing temperature. Additionally, Kleiman et.al. [4] observed that, besides having “conventional quantization,” UPt_3 's VL exhibits distorted hexagonal symmetry; their study predicts that Fermi-surface and gap anisotropies—meaning that measurements are directionally dependent—could explain UPt_3 's anisotropy. Finally, according to Joynt and Taillefer [2], the coupling between magnetism and superconductivity is the weakest point in any theory about UPt_3 . In this respect, all of these studies reveal why UPt_3 is an interesting superconductor.

This particular study used SANS experiments to analyze the UPt_3 's VL. The principle behind this experiment arises from quantum mechanics. Since the neutron has a spin, it has a magnetic moment. Because of a varying magnetic potential energy in the VL, the neutrons are diffracted. Moreover, a neutron has a characteristic wavelength related to its momentum. When neutrons encounter the VL, they scatter in a manner akin to crystal X-ray diffraction. In its elementary form, the Bragg condition for lattice scattering is given

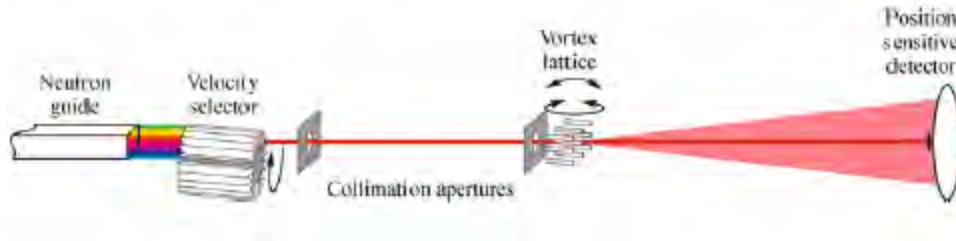


Figure 2: Diagram of a typical SANS experiment [5].

by

$$\lambda = 2d \sin \theta, \quad (1)$$

where θ is half of the scattering angle, λ the neutron's wavelength, and d the VL spacing. Because a neutron's de Broglie wavelength is perhaps on the order of 10 \AA while the VL spacing is 1000 \AA , SANS is an ideal technique to analyze the VL. That is, it is ideal because the scattering angle is small; the order-of-magnitude estimates show that $\sin \theta \approx \theta = \lambda/(2d) = 10/2000 = 5 * 10^{-3}$.

The SANS setup is summarized in Fig. 2. The neutrons go through a velocity selector that regulates which neutrons pass through the instrument and are then collimated. They interact with the sample, and the scattered neutrons fall upon a detector while the unscattered neutrons are absorbed by a beamstop [5]. To satisfy the Bragg conditions for scattering from the VL planes, the sample and magnets are tilted together at small angles. If the scattering intensity is plotted versus the tilt angle, a “rocking” curve is generated. More details about this curve appear in the studies considered below.

2 The Experiments

The two SANS studies were conducted at the Paul Scherrer Institute (PSI) in Villigen, Switzerland. One study in August 2011 was conducted with *SANS-I* while the other was

done with *SANS-II* in May 2012. Parts of each experiment were devoted to understanding UPt₃'s $H - T$ phase diagram. Since the symmetry of the lattice is well-documented, only two diffraction spots were imaged to save time. The applied field was set parallel to the crystal's a^* axis for the parts of the experiments discussed below.

2.1 SANS-I Experiment: August 2011

For the SANS-I experiment, the sample was cooled down to a temperature as low as 43 mK using a dilution refrigerator. The applied magnetic field H was ramped up to about 3.0 T—well above the critical-field H_{c2} transition. Then the field was dropped down and oscillated about the desired setting to set up the VL. The neutrons' wavelength was set at 6 Å, and the detector distance was 16.0002 m.

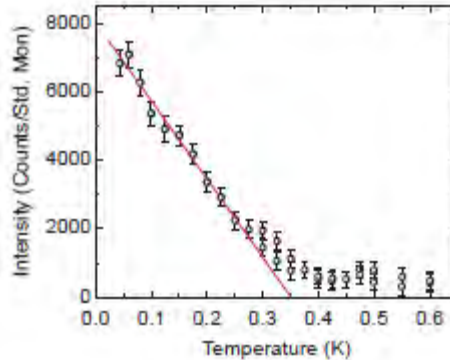
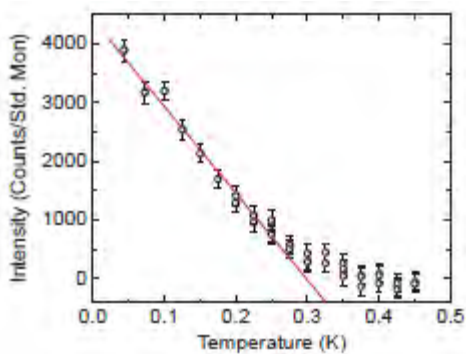
Rocking-curve data was collected at multiple field and temperature settings. During the analysis, the data were fitted with Gaussian and Lorentzian curves, and the Full-Width-Half-Maximum (FWHM) of each curve was determined from the fit. Nonetheless, all of the rocking curves did not necessarily have good resolution. The limited resolution arises from the sample size as well as the instrument itself.

With the applied field constant, some others were taken at various temperatures to check if the rocking curves were broadening as the temperature increased.²

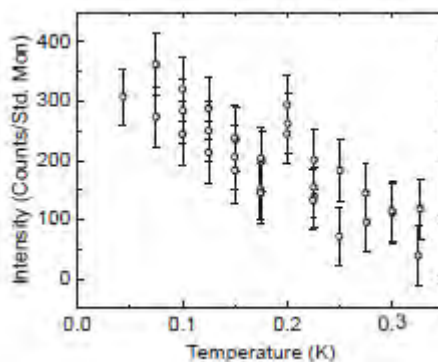
Two scans of the temperature dependence of the peak's intensity were done for a 0.4-T setting; this explored the transition through the tetracritical point. Fig. 3(a) shows one of the 0.4-T temperature scans. Notice the linearity in the plot at low temperatures (up until about 300 mK or so) and the positive curvature as the VL transitions from the B phase into the normal state in Fig. 3(a).

Fig. 3(b) shows the temperature dependence for $H = 0.2$ T, and it represents a transition

²This was done since it was assumed that the rocking curve's FWHM was constant for a peak's form-factor analysis; this issue will be explored.



(a) $H = 0.4$ T. A linear fit is drawn for the low- (b) $H = 0.2$ T. Note the slight “bump” in the temperature dependence. plot between 450 and 500 mK.



(c) $H = 0.75$ T. Due to low peak intensity and low count rates, there is evidently more noise in this data.

Figure 3: Temperature dependence of the average peak intensity for three different field settings (SANS-I).

from the B to A phases and then into the normal state. Observe that the linear relationship between the peak’s intensity and temperature still occurs at lower temperatures (i.e., while UPt_3 is in the B phase); positive curvature also appears as it did for the 0.4-T scan.

Nonetheless, there is a difference between Figs. 3(a) and 3(b). Notice the “bump” in the plot at higher temperatures (starting around 450 mK) for the temperature dependence in Fig. 3(b); it is absent in Fig. 3(a). This raised the question of whether a new phase had been discovered, and it motivated the SANS-II experiment.

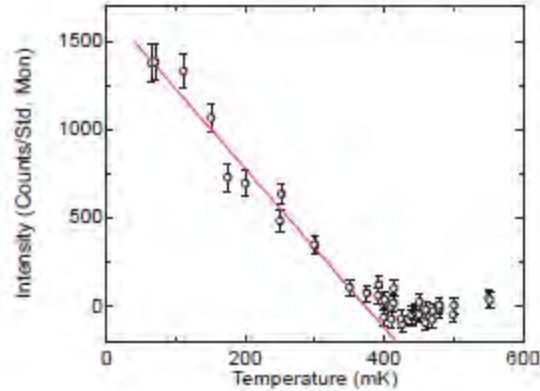


Figure 4: Plot of average peak intensity versus temperature for $H = 0.2$ T (SANS-II).

A final temperature scan was done at 0.75 -T—well into the C phase. Fig. 3(c) shows the resulting temperature analysis. Because of poor signal-to-noise readings, more measurements with higher count rates will be needed in the future to explore this field-temperature regime. Nonetheless, measurements in this high-field regime were unprecedented.

2.2 SANS-II: May 2012

For the SANS-II experiment, the sample was cooled with a dilution refrigerator. In some cases, the temperature was as low as 65 mK. To prepare the VL, the applied magnetic field was ramped up well above the H_{c2} transition, then dropped down and oscillated about the final field setting. The detector’s distance was 6.2 m, and the neutrons’ wavelength was about 8 \AA .

One of the experiment’s aims was to expand upon the SANS-I’s VL study, which showed a “bump” in the 0.2 -T temperature dependence. The sample’s temperature was lowered to 65 mK and then increased while the applied field was kept constant at 0.2 T. Fig. 4 displays the resulting temperature scan. More data was collected in the higher-temperature regime, and it is concluded that the “bump” that characterized the curve in the 0.2 -T scan from SANS-I disappeared with better statistics.

Unfortunately, background noise is prominent at higher temperatures for this experiment. Background subtraction often resulted in a small negative intensity. Nothing could be done to eliminate this problem.

2.3 Form-Factor Comparisons

By comparing the temperature dependence of the form factors, we can see how reproducible the results are between the two experiments. Recall that the form factor is the Fourier transform of the magnetic-flux modulation. In theory and practice, both experiments should yield similar temperature dependences in the form factors at a particular field setting—0.2 T in this case. Generally, the form factor can be found by manipulating the following relationship:

$$R = \frac{2\pi\gamma^2\lambda_n^2 t}{16\phi_0^2 q \cos \eta_Q} |\mathbf{h}(\mathbf{Q})|^2, \quad (2)$$

where R is the peak’s reflectance—the peak’s integrated intensity divided by the direct beam’s intensity, $\gamma = 1.91$ the neutron’s gyromagnetic ratio, the neutrons’ wavelength λ_n , the form factor $\mathbf{h}(\mathbf{Q})$, the Lorentz correction $\cos \eta_Q$,³ the scattering vector q , the sample thickness t , and ϕ_0 the flux quantum (2070 T*nm²).

Briefly, to do a form-factor analysis, rocking-curve data must have been collected for the field setting considered. During a temperature scan, multiple rocking curves are taken at a few temperatures to check if the rocking curves are broadening as the temperature increased. This is done because during the analysis, it would be assumed that the Full-Width-Half-Maximum (FWHM) was constant throughout the temperature scan.

When choosing an FWHM, it is customary to look at the “base”-temperature rocking curve and use its FWHM for the analysis. For any rocking curve, the FWHM can be obtained

³ η_Q can be obtained from angular measurements in the diffraction pattern. In this case, it can be thought of as a “spot” angle.

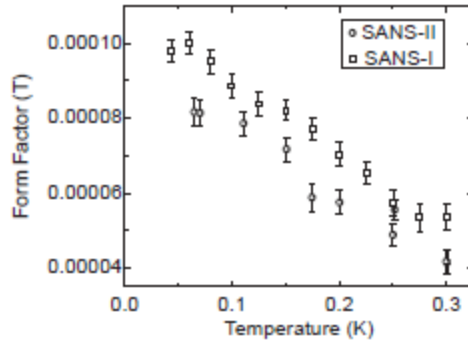


Figure 5: Temperature dependence of the form factor (at “low” temperatures) for both the SANS-I and SANS-II experiments at $H = 0.2$ T.

from a fit to the curve. This requires another assumption—the kind of curve fit, for rocking curves can be fitted with a Gaussian, Lorentzian, or Voigt (the best-fit) curve. For simplicity, a Gaussian fit was assumed. At a particular temperature, by knowing the FWHM and a scattering peak’s maximum intensity, the integrated intensity of each scattering peak can be generated. From this, the reflectance R can be determined once the direct beam’s intensity is known. Assuming that all other quantities have been analyzed, the form factor can be determined.

Fig. 5 shows the temperature dependence of the form factor from both experiments. Notice that there is some difference between the form factors, but in general, it seems that the form factors from each experiment have a linear dependence with temperature. Differences probably arise based upon detector calibration as well as any errors in the assumption. Moreover, the rocking curve used for the SANS-II analysis had large error bars, causing some more differences to arise.

3 Summary

This study investigated UPt_3 's VL via SANS experiments, focusing upon the characteristics of the VL at various points in the $H - T$ diagram. These experiments looked at multiple state transitions. In particular, the VL was analyzed at an unprecedented applied field setting of 0.75 T-well within the superconducting C phase. Additionally, the SANS-II experiment resolved any question about the possible existence of another superconducting state; statistics from this experiment seem to suggest that there is not another state.

References

- [1] M. R. Eskildsen, “Small Angle Neutron Scattering Studies of the Flux Line Lattices in the Borocarbide Superconductors,” Ph.D. Thesis, Risø National Laboratory and University of Copenhagen, 1998.
- [2] R. Joynt and L. Taillefer, “The superconducting phases of UPt_3 ,” *Rev. Mod. Phys.* **74**, 235 (2002).
- [3] A. Huxley, P. Rodière, D. Paul, N. van Dijk, R. Cubitt, and J. Flouquet, “Realignment of the flux-line lattice by a change in the symmetry of superconductivity in UPt_3 ,” *Nature* **406**, 160 (2000).
- [4] R. N. Kleiman, C. Broholm, G. Aeppli, E. Bucher, N. Stücheli, D. J. Bishop, K. N. Clausen, K. Mortensen, J. S. Pedersen, and B. Howard, “Neutron Diffraction from the Vortex Lattice in the Heavy-Fermion Superconductor UPt_3 ,” *Phys. Rev. Lett.* **69**, 3120 (1992).
- [5] M. R. Eskildsen, “Vortex lattices in type-II superconductors studied by small-angle neutron scattering,” *Front. Phys.* **6**, 398 (2011).

**Study of Cataclysmic Variable B7 in NGC 6791:
From the Ground and from Space**

K. C. Magno

College of Science, University of Notre Dame, Notre Dame, 46556

kmagno@nd.edu

and

P. M. Garnavich

Department of Physics, University of Notre Dame, Notre Dame, 46556

pgarnavi@nd.edu

Received _____; accepted _____

comment

ABSTRACT

We present a study of one of three cataclysmic variables found in NGC 6791, one of the oldest and most metal-rich open clusters. Spectroscopic and photometric evidence show that the cluster's metallicity is a factor of 2-3 times the solar value. Comparing B7 with other CVs may allow a better understanding of the affect of metal abundance on the accretion process. Prior studies established the variable as either a dwarf nova or nova-like. Thus, 30-min cadence of Kepler observations, which allowed for near-continuous coverage, taken over a year and B7 spectra taken by the Large Binocular Telescope (LBT) are used to determine the orbital period and class of the variable. Light curves and power spectra reveal an orbital period of 0.158 days (3.8 hours) and the spectrum strongly indicates that B7 is a nova-like cataclysmic variable. The stars full light curve has a mean magnitude of 17.8 over a year with a typical deviation of 0.6 mag and is absent of outburst activity. The latter is not unusual for nova-like variables. Further study will include comparing the light curve with that of other CV to determine more of how the high metallicity affects the binary system.

1. Introduction

Cataclysmic variables are binary stars that are periodically flooded with energy and mass, causing a variability in magnitude, including short, irregular, and rapid changes as well as dramatic outbursts. Most systems consist of a white dwarf as a primary star and a secondary star that donates mass and energy, thus forming an accretion disk around the dwarf, which mostly emits UV radiation. The variables can be studied through their exhibition of irregular light variability and spectral lines mainly located in the blue and

ultraviolet region. X-ray observations are also helpful in that they reflect hot regions of interaction between the accretion disc and the primary star. B7 is a variable located in the globular cluster NGC 6791 and has been previously studied by J. Kaluzny et al (1997) and B. J. Mochejska and K.Z. Stanek (2003). Indeed, the total mass of observed stars exceeds $8.0 \cdot 10^{33}$ kg. NGC 6791 is one of the oldest open clusters with an approximate age of 8 billion years and located in the constellation Lyra. Spectroscopic and photometric evidence show that the cluster's metallicity is a factor of 2-3 times the solar value. This characteristic can affect many other aspects of the system, including the magnetic coupling between the stars, the cooling rate and availability of electrons, and the opacity of the surrounding gas. The cluster is also special in that it contains a group of hot subdwarfs.

2. Cataclysmic Variable B7

Previous studies have provided some information on B7, including data that shows a high mass-transfer rate with occasional dips to quiescence. It has been noted that while in its high state the star would be difficult to identify as a cataclysmic variable using the two most popular methods: Searching for photometric variability and selecting objects with strong emission in the Balmer lines. Indeed, past spectra of B7 presents only weak emissions and an absence of higher lines in the Balmer series.

3. Observations

Kepler data from 539.4702 to 905.9265 Kepler Barycentric Julian Days (BKJD=BJD+2454833.0) taken with a 30-minute cadence was utilized in this study, as it provides the best rise-times information that has ever obtained for a thermonuclear supernova. The use of unit BKJD alters the data and corrects so that the arrival times are

at the barycenter of the Solar System. The flux located in the optimal aperture in electrons per second and generated by the Pre-search Data Conditioning pipeline module, titled PDCSAP FLUX, provided the y values for the light curves. The negative log base 10 of the PDCSAP FLUX multiplied by 2.5 and added to 25 provided magnitude. This magnitude is then smoothed in IDL over a value of 100, which is then divided into the original magnitude value. This quotient is then used to find the mean, which is then subtracted from the smoothed magnitude values. This smoothing and subtracting of the mean improves the signal to noise ratio. Thus, the light curve plots magnitude versus time (BKJD) (Figure 1).

A drop of approximately 3 mag over 10 days was observed in Kaluzny's study of B7. Though this is characteristic of dwarf nova proceeding outburst, classifying the variable was still indeterminable due to lack of further substantial reasoning. This study utilizes 30-min cadence of Kepler observations taken for an entire year, providing near-continuous coverage of the variable and 16,261 data points. It is absent of outburst activity and deviates from the mean magnitude, 17.8, by typically 0.6 mag, with a minimum value of 18.6 mag and a maximum value of 17.2 mag. This variation is small compared to a dwarf nova, but significantly large for a nova-like CV. Indeed, dwarf nova usually have a lower luminosity, as seen in the light curve (Figure 2) of B8, the second CV found in NGC 6791. There is an outburst that occurs over a period of approximately 10 days, another characteristic of dwarf nova. Thus, in order to classify B7, a spectrum was taken using the Large Binocular Telescope (LBT) (Figure 3). The data shows the consistent presence of absorption lines, except for H α , indicating an optically thick accretion disk. As this is characteristic of the class, there is strong indication that the variable is nova-like. Indeed, dwarf novae primarily give off emission lines after an outburst and have relatively thin disks.

In order to determine the orbital period of the star, power spectra in the low, medium, and high frequency ranges were created. The first plotted frequencies from 0.01 to 2.0

cycles/day (Figure 4) shows a small spike at 0.10 cycles/day and some noise at the beginning of the data set. The log of the x axis was taken in order to view all the values for the frequency range and not just some, making the smaller spikes are easier to view. The medium frequency power spectrum spans from 2.0 to 8.0 cycles/day (Figure 5) and the log of y axis was taken, thus enabling all spikes at different frequencies to be seen. It is within this plot that the significant spike at approximately 6.3105 cycles/day is presented. Thus, we suspect the orbital period to be 0.15847 days (3.8031 hours). The final power spectrum plots frequencies from 2.0 to 46.0 cycles/day (Figure 6). Here, the large spike is dominant and reaches a relative power of approximately $2.7 \cdot 10^{-9}$. An alias spike can also be seen at 42 cycles/day, which is a beat frequency due to the sampling rate and the value of the orbital frequency ($48-6.3105$). A phase plot (Figure 7) was created using the period, 0.15847 days, and time of the Kepler observations. These phase values were then sorted into 10 separate bins. The median of each bin was then determined in order to cut major outliers and make the sinusoidal trend more prominent. Thus, the plot is smoothed magnitude versus phase. It has an extremely small amplitude of approximately $1.4 \cdot 10^{-4}$, making near-continuous coverage for an entire year necessary in order to study the CV.

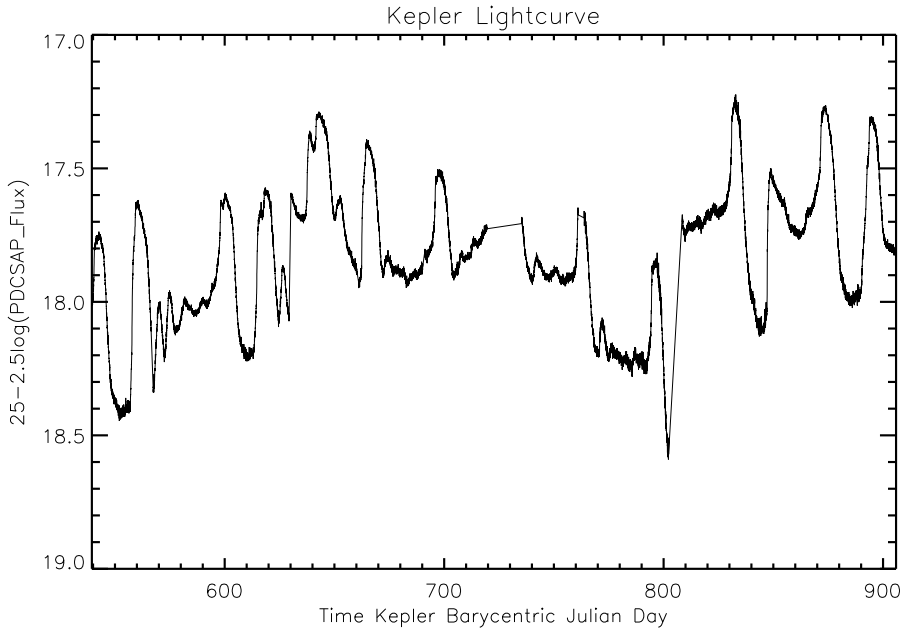


Fig. 1.— Light curve of B7. Minimum and maximum magnitude of 18.6 and 17.2 mag, respectively. There is no outburst activity, with a typical deviation of 0.6 mag from the mean of 17.8 mag.

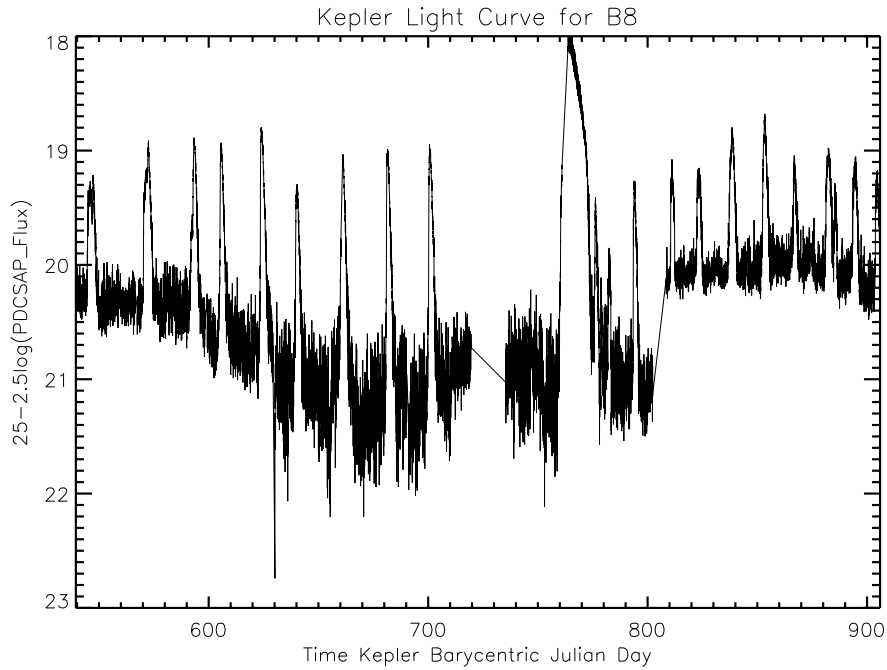


Fig. 2.— Light curve of B8. Generally low magnitude and outburst activity over a period of 10 days. Suspected to be a dwarf nova CV.

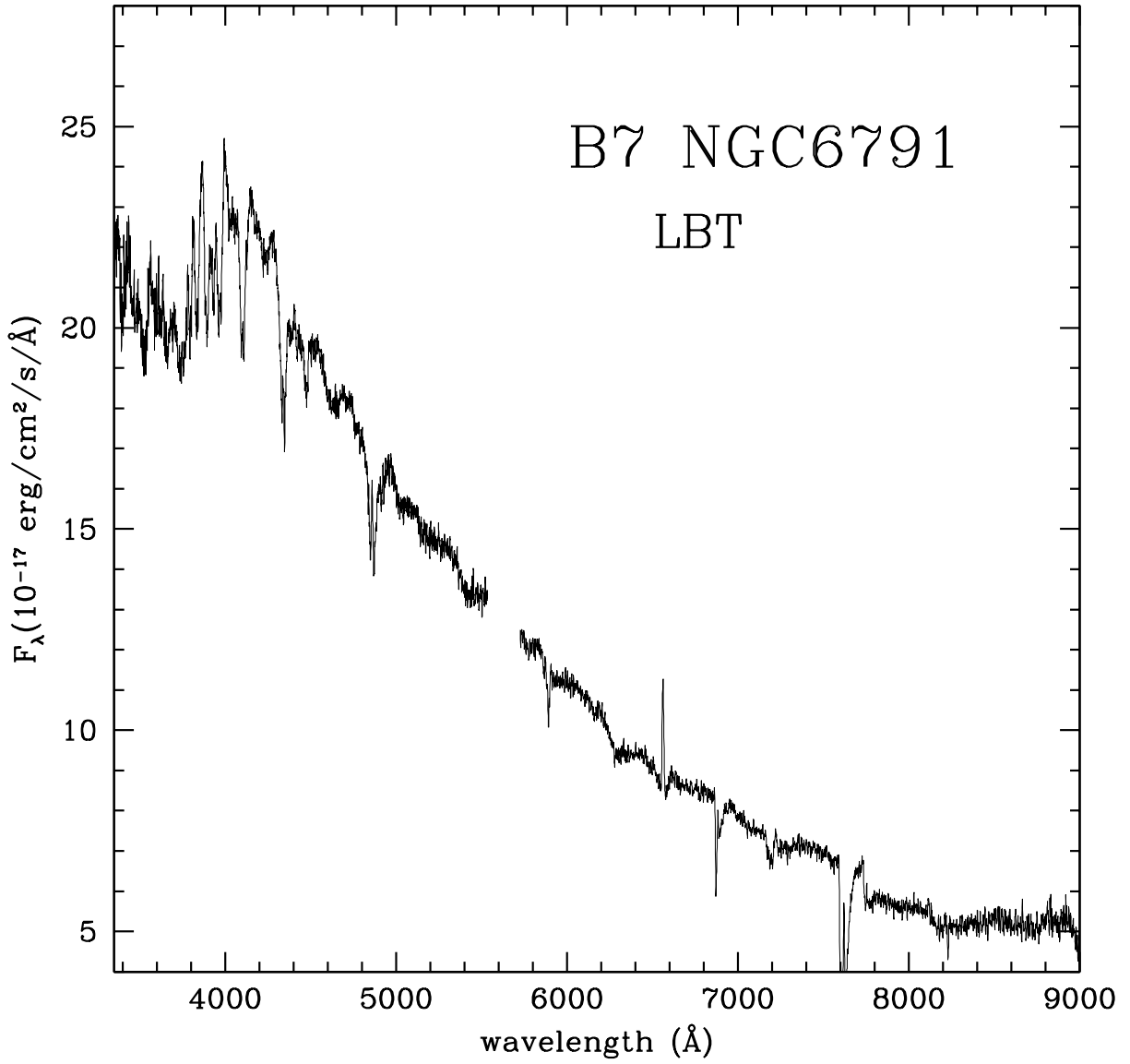


Fig. 3.— Spectrum of B7. Dominant absorption lines represents a thick accretion disk, indicating B7 is nova-like.

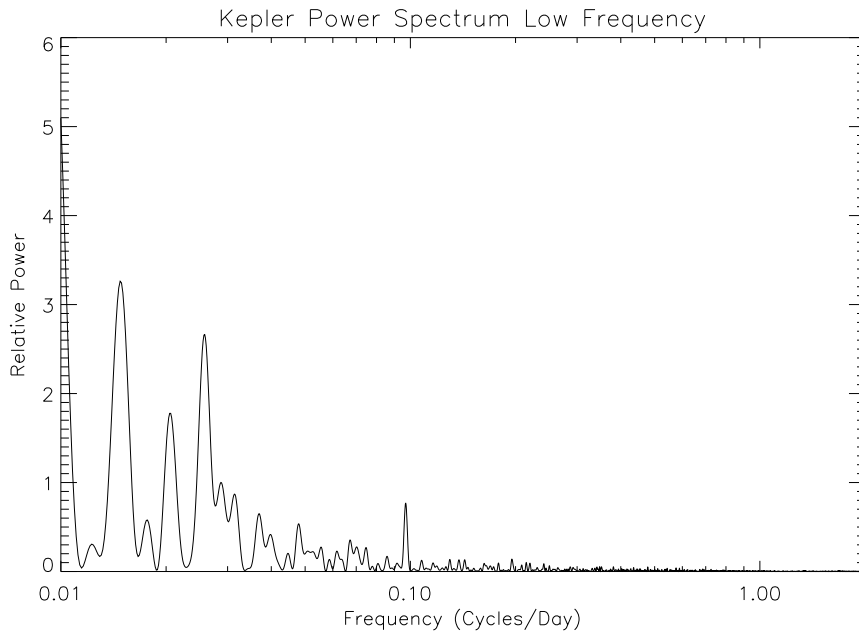


Fig. 3.— Low Frequency (0.01-2.0 cycles/day) Power Spectrum for B7. There is noise at the lower frequencies, with a small, but less meaningful spike at 0.10 cycles day.

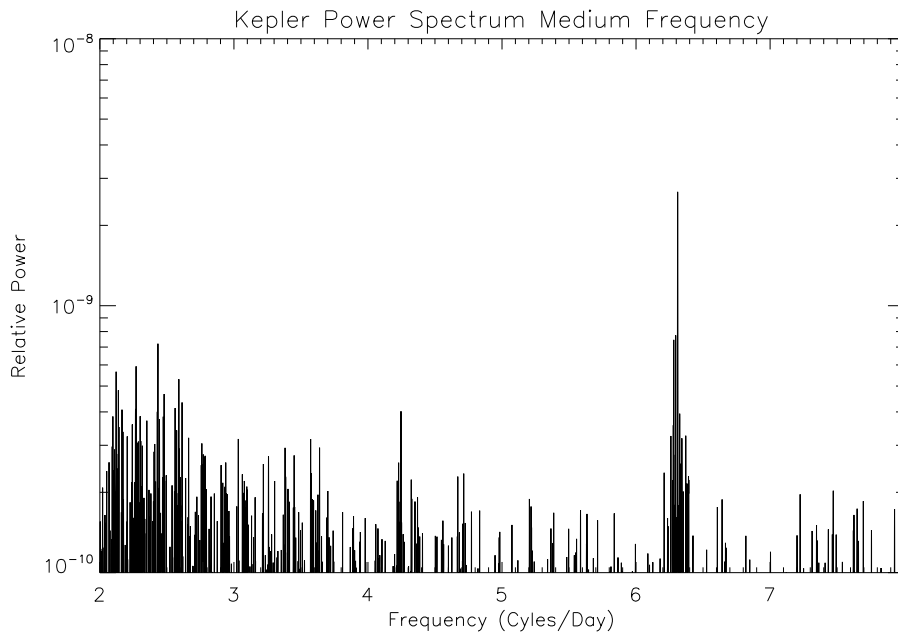


Fig. 4.— Medium Frequency (2.0-8.0 cycles/day) Power Spectrum for B7. Large spike at 6.3105 cycles/day, resulting in an orbital period of 0.15847 days (3.803 hours).

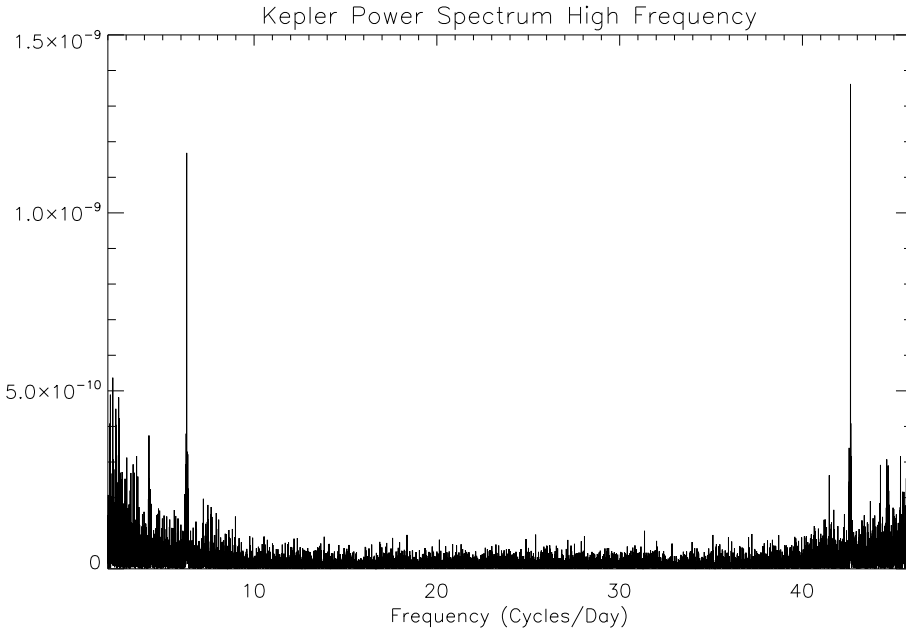


Fig. 5.— High Frequency (2.0-46.0 cycles/day) Power Spectrum for B7. Large spike at a frequency of 6.3105 can be seen along with the taller alias spike at approximately 42 cycles/day. This spike is the beat frequency due to the fact that the sampling is taken every 30 minutes and the orbital frequency (48-6.3105).

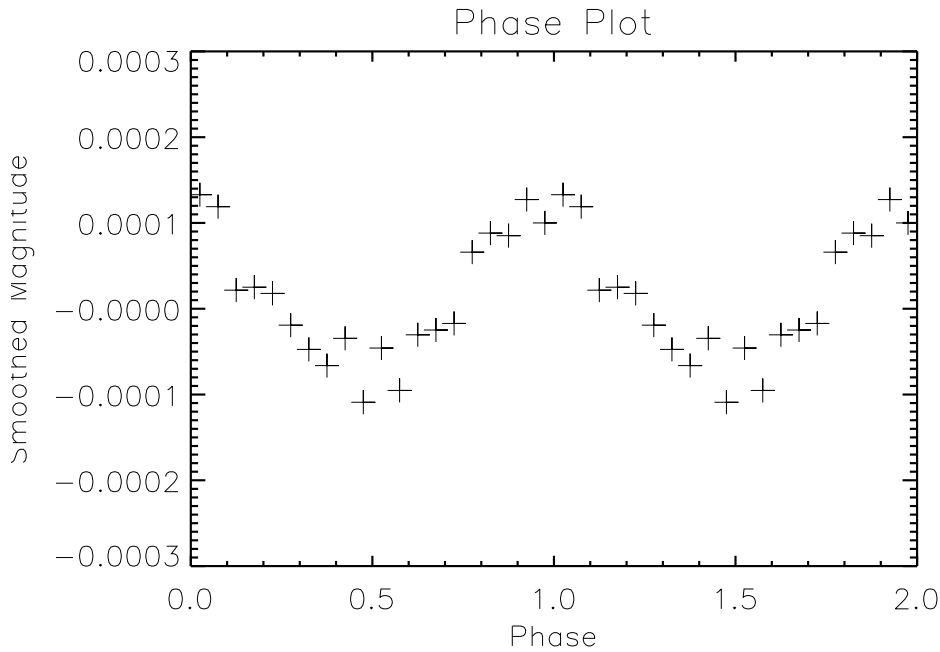


Fig. 6.— Phase Plot for B7. Extremely small amplitude of approximately 0.00014 emphasizes the need for near-continuous coverage taken over an entire year by Kepler.

4. Conclusion

Based on the near-continuous coverage Kepler observations and the spectrum of B7 taken with the Large Binocular telescope, there is strong indication that the binary is a nova-like cataclysmic variable. Furthermore, we suspect the orbital period is 0.15847 days (3.8031 hours), which is normal for CV. Unlike the light curve presented in Kaluzny et al, B7 did not exhibit any outburst activity during the entire year. Indeed, it deviates from the mean magnitude, 17.8 mag, by typically 0.6 and has a minimum and maximum value of 18.6 and 17.2 mag, respectively. The phase plot shows an extreme small amplitude of approximately 0.00014. Without the near-continuous coverage from Kepler for an entire year, any variations would have nearly impossible to detect. Future studies will include comparing the full light curve of B7 with that of other CV in order to better understand how the metal abundance of NGC 6791 affects the accretion process of the variable.

5. References

Sources:

1. Kaluzny et al (1997)
2. B. J. Mochejska and K.Z. Stanek (2003)

St. George Recoil Mass Separator Time of
Flight and Position Sensitive Detector

Luis Alfredo Morales

NSF/REU Program

Physics Department, University of Notre Dame

Advisor: Manoel Couder

Abstract

The St. George recoil mass separator at the University of Notre Dame will be used to study (α, γ) reactions of astrophysical interest. A detection system being developed for St. George at Indiana University South Bend and Notre Dame will utilize energy, time-of-flight, and position to separate reaction products from residual unreacted beam particles. Two designs for the timing detectors have been investigated – an electrostatic mirror design and a combination of electrostatic plates with magnetic deflection. Both designs deflect secondary electrons produced by the passage of an ion through a thin carbon foil onto a microchannel plate (MCP) detector, which registers timing and position measurements. A detailed analysis of position and timing resolution for the two designs was conducted using the ion optics simulation software SIMION, in order to identify the configuration best suited for the challenges presented by these low energy and low count rate experiments. SIMION was also used to study an electrostatic deflector that will be used to test the angular acceptance of St. George.

Introduction

Notre Dame's Nuclear Science Lab (NSL) is the bridge between nuclear physics and astrophysics. Nuclear Astrophysics at Notre Dame is focused in measurements of nuclear reaction rates and decay processes and extrapolates those to stellar temperatures[2]. The cross-sections drop exponentially at stellar energies and so become difficult to separate from background. The

three main background components are natural radiation, cosmic rays, and beam induced radiation.

The Strong Gradient Electromagnetic Online Recoil separator for capture Gamma Ray Experiment (St. George) was specially designed for low energy (α, γ) reactions. The St. George consists of a helium gas jet target, six dipole magnets, 11 quadrupole magnets, a Wien filter, and a detection system [1]. St. George is divided up in three sections: Section 1 consists of the helium gas target where the reaction occurs; Section 2 consists of several bending magnets to reject particles of the wrong charge, along with the Wien filter, which is the mass selector; Section 3 provides additional background reduction while at the same time bending the desired particles to the detection system. The detection system separates the background from the reaction product. The background consists of mainly unreacted beam and possibly other particles that entered the beam line due to the beam colliding with the inside of the separator. This is where a detection system that measures time of flight and energy deposited becomes a great asset in discerning particles of interest from background.

In order to explore the various detection set-ups we did simulations using an ion optics program called SIMION. Our main goal was to determine the limits to the position and timing resolution imposed by the geometry. To keep our results consistent for multiple design options we standardized the particle attributes. To simplify things we excluded the ion and simply focused on the electrons being emitted at the surface. Using SIMION's built-in functions we generated 30 electrons for each passing ion with a half angle of 45

degrees with respect to the normal of the carbon foil with a Gaussian energy distribution around 30 eV (FWHM=10 eV). For each electron we recorded it's initial and final timing as well as the position. We used the ROOT data analysis framework [3] to analyze the data and extract the timing and position resolution.

Electrostatic Mirror

The electrostatic mirror design consists mainly of three different electrodes (Fig. 1). The first electrode consists of a self-supporting thin carbon foil at a negative potential. This is where the ion begins its journey through the detection system, depositing some energy in the foil and ejecting electrons from the carbon foil. The electrons are then accelerated toward the entrance grid where they enter electrode number 2. Electrode number 2 is also known as the faraday cage portion, which consists of the microchannel plate (MCP), three plates arranged in a right triangle with two of those plates containing grids with wires of thickness of $20 \mu\text{m}$. Once the electrons enter the faraday cage they essentially experience no force until they pass through the exit grid. After they pass the plane created by the exit grid they come to the third electrode also known as the mirror grid. This is where the electrons are deflected back into the faraday cage in the direction of the MCP where they will be detected.

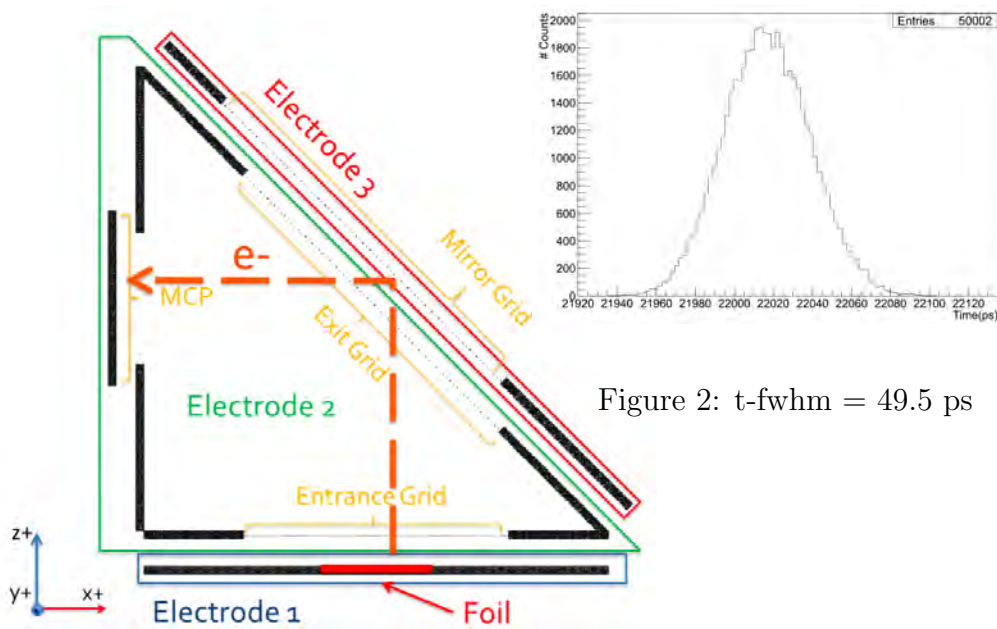


Figure 2: $t\text{-fwhm} = 49.5 \text{ ps}$

Figure 1: Electrostatic Mirror

Analysis

Last summer, in research at Indiana University South Bend on the electrostatic error using the same techniques it was found that the timing resolution was 49.5 ps (Fig. 2) and the position resolution was 2.25 mm \hat{y} (Fig. 3) and 2.16 mm in \hat{z} (Fig. 4). It was also recognized that the grids presented a problems because we had 3 grids and there were chances of one of the ions of interest being stopped.

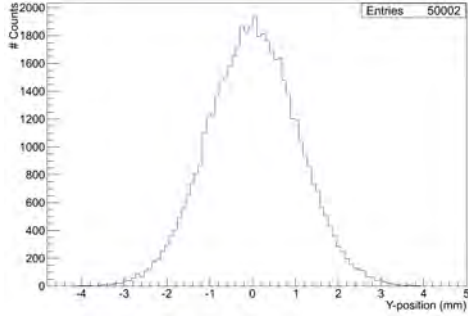


Figure 3: y-fwhm = 2.25 mm

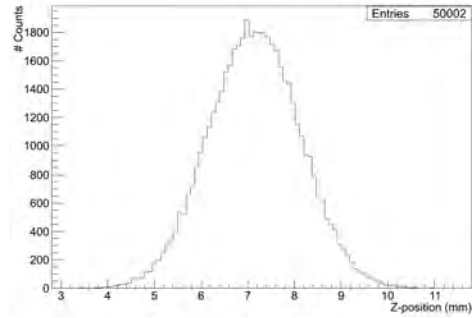


Figure 4: z-fwhm = 2.16 mm

Magnetic Deflection

The magnetic deflection design consists of a foil, four electrodes, an MCP, and a magnetic field perpendicular to the direction of electron emission. As the ions pass through the carbon foil electrons are emitted from the surface of the Carbon foil and are then accelerated away from the carbon foil which is at a negative potential toward electrode 1 which is at ground potential (Fig. 5). At any given point the particle experiences a force, which can be described with the formula.

$$F = Q(E + (v \times B)) \quad (1)$$

The Lorentz force is responsible for turning the electrons is such that the electrons accelerate until they reach in-between last two electrodes and then magnetic field starts to dominate. Hence, they experience a net force towards the MCP. While moving towards MCP, electrons are decelerated due to electric field. The MCP is set at a lower potential than the foil to ensure that the electrons don't lose all their energy before being detected. The MCP

then records the timing and position of the electron cloud that is produced.

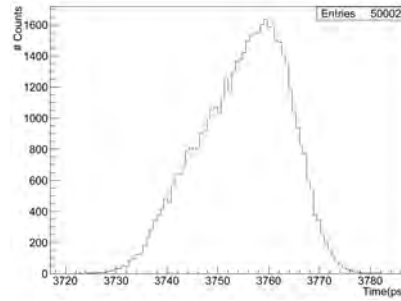
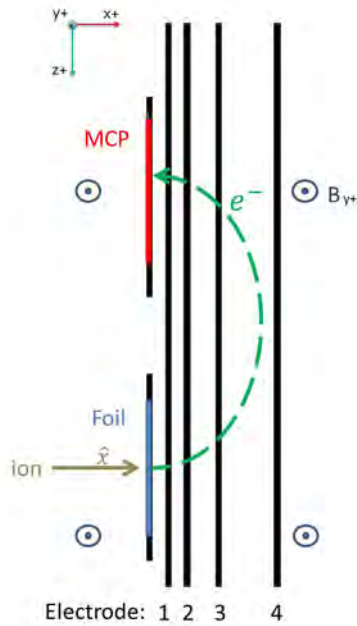


Figure 6: t-fwhm = 19.6 ps

Figure 5: Magnetic Deflection

Analysis

Using the standard particles to test the magnetic deflection set-up results found that timing resolution was on the order of 19.6 ps and our position resolution was 0.33 mm in \hat{z} but much poorer in the \hat{y} direction (1.68 mm) due to the fact that there is no focusing effect. We decided to make the magnetic deflection officially the detector of choice. The selection of the magnetic deflection design was mainly because allows us to reduce the number of wire grids introduced in the path of the beam line.

We have given up the large number of grids by deciding on this design, but

with this design come new challenges, the most significant is creating a large enough good magnetic field region in the limited space available inside the detector chamber.

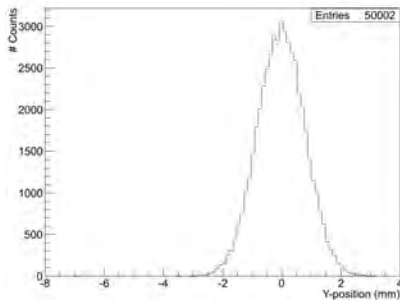


Figure 7: y -fwhm = 1.68 mm

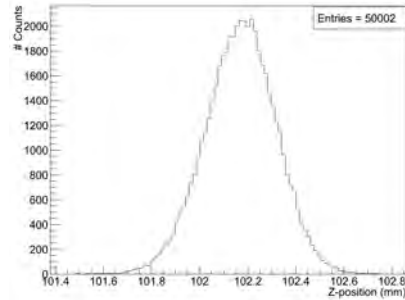


Figure 8: z -fwhm = 0.33 mm

Electrostatic Deflection

On a final note, a few steps were also taken into designing and simulating an electrostatic deflection device that will be used in commissioning the St. George by checking to see if it meets its design capability of 40 mrad acceptance angle. To test the electrostatic deflection a 3 mm diameter +1-charge Neon beam with a kinetic energy 5 MeV was simulated in SIMION. Checking only in two dimensions, the goal was to see what it would take to deflect the particle by 40 mrad. So, two plates were made and put at opposite potentials. This electrostatic deflector would temporarily have to take the place of the gas jet target, so there were size limitations. The only removable section was about 11.5 inches but that only really left a realistic length of 9 inches for the electrodes. Another design limitation was that we wanted to make sure that the particles that were being deflected had a trajectory that could be traced

back to a single plane, that plane ideally being the location of the gas jet target. The plates at 14 mm apart created very distorted fringe fields for a 3 mm beam, which distorted the shape of the beam into a triangle. Increasing the plates to a distance of 40 mm apart with an extremely unrealistic voltage of 225 keV, indeed fixed our issue. Scaling down to 6 cm and a voltage of 50 keV, the distortion was present but acceptable. It is unworkable to place the large voltages that are required to bend a Ne 20 charge 1 with 5 MeV, but one can lower the energy of the beam and increase the charge state to decrease the potentials to levels that would not spark. We get a spark at about 3 kV/mm but we would like to stay at 1 kV/mm. In order to improve the design it will be necessary to see how close the plates can be brought together at the edges without exceeding the 1 kV/mm that has been set as a safety measure.

Conclusion

A prototype of the magnetic deflection set-up is currently being built at the University of Notre Dame machine shop. Designs to mount the new detector chamber to St. George are also being developed. Furthermore, the project to develop a stand inside the detector chamber for the magnetic deflection system is still ongoing. Designs for the electrostatic deflector to check acceptance angle of St. George are also ongoing. Moreover, the St. George is a continuing project with work being done to create a beam line that will link it to the new 5 MeV accelerator.

References

- [1] M. Couder et al. Design of the recoil mass separator St. George. Science Direct. (2007): 35-45. Print
- [2] <http://physics.nd.edu/research/research-groups/nuclear-physics-group/>
- [3] <http://root.cern.ch/drupal/>

Identification of Naturally Occurring Radioactive Material in Sand

Michael Pope

2012 NSF/REU Program

Physics Department, University of Notre Dame

Advisors: Dr. Ed Stech, Dr. Michael Wiescher

Abstract

Radionuclides that occur in the environment through natural means, known as Naturally Occurring Radioactive Materials (NORM), are mostly by-products of the Thorium and Uranium nuclear decay chains. These are naturally occurring substances that emit gamma rays before reaching their ground state. For this reason we used a high purity germanium detector, to perform a gamma spectroscopy analysis on the samples of sand from the Southeastern shores of Lake Michigan, Notre Dame and Germany. It was determined that Germany rock had the highest levels of NORM when compared to the other samples.

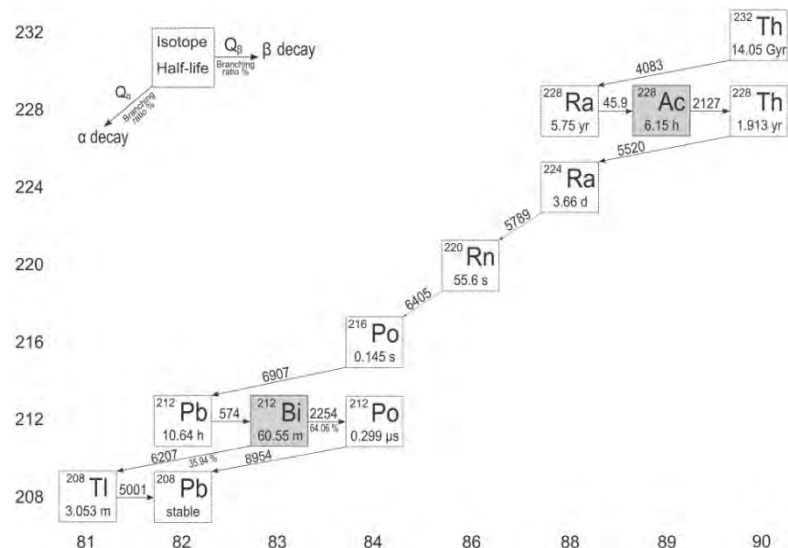
Introduction

The radionuclides that occur in nature can be broken down into two groups. The first group is the primordial group which means that the half-life of the nuclide is comparable to the life of the earth on the order of 10^9 years. The second group is the secondary nuclides, which have gained existence through the decay of the primordial nuclides. There are three decay chains that are the most common and are all headed by different nuclides. The Thorium decay begins with the Th-232 and the

Uranium decay begins with U-238[4].

The process of these decays go through one of three modes of decay to become a daughter nuclide; alpha, beta minus and beta plus. Alpha

decay occurs largely in elements with atomic numbers greater than 83. During this process an



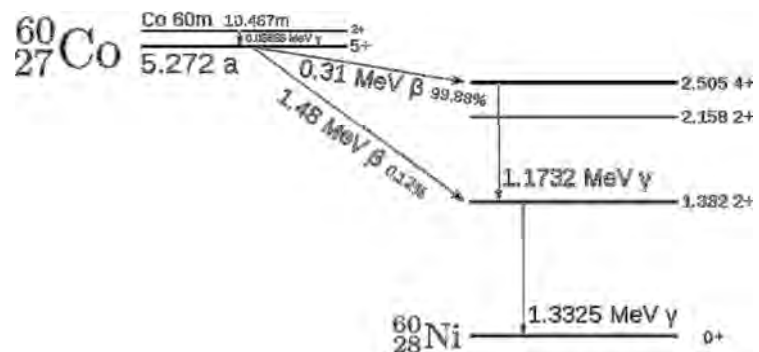
alpha particle is emitted which changes the atomic number of the parent nuclide because an alpha particle is a He nucleus. The alpha mode of decay can be seen as: ${}^A_Z X \rightarrow {}^{A-4}_{Z-2} Y + {}^4_2 He$

The other two modes of decay are very similar because they are both beta decay but have different products. Beta minus decay yields a beta particle which is an electron and comes from the process of a neutron converting to a proton and emitting an electron, it is characterized by: ${}^1_0 n \rightarrow {}^1_1 p + {}^0_{-1} e + {}^0_0 \bar{\nu}_e$

The beta plus decay goes through a similar process but its product is different from the beta minus, it begins with a proton and converts it into a neutron while emitting a positron during the process, which can be seen as: ${}^1_1 p \rightarrow n + {}^0_{+1} e + {}^0_0 \nu_e$

Both decay modes emit a neutrino, antineutrino for beta minus and a neutrino for beta plus, this is done to conserve angular momentum and energy [1].

During the process of nuclear decay there is a possibility that when the parent nuclide decays to the daughter nuclide that the daughter nuclide will be in an excited state or a ground state. If it is in the ground state it will continue on the decay chain unless it is stable. If it is in an excited state then it will get to the ground state by other means, which is through the emission of gamma rays. In some cases a nucleus will emit a single gamma ray and then drop to the ground state energy. More commonly the nucleus will emit a cascade of gamma rays to drop to the ground state. Once in the ground state the nucleus no longer emits gamma rays but it may undergo nuclear decay if it is unstable [4].



The detection system for low count environmental radioactivity experiments is

commonly a coaxial high purity germanium detector. These detectors are used because of their superior energy resolution. When performing low count experiments the background needs to be minimized so that the detector is recording data from the sample and not the background environment. This is especially important when collecting gamma spectra because the building materials that may surround the detector could have nuclides that are gamma emitting. The best example of this is the Potassium-40 that is in all concrete, if this is not taken into account then the Potassium-40 line on the spectra will be much higher than it should be, this is also true for the Uranium, Cesium and Thorium lines. In order to minimize this, shielding must be placed to prevent gamma rays from getting through to the detector. Lead is the ideal shielding material because of its high density. With the use of lead there is a chance that the emitted gamma rays will excite an electron in the lead and the lead K-lines will be visible in the spectra, these K-lines can be minimized by adding another layer of shielding which is usually a copper layer [1].

Experimental Setup

The samples from Lake Michigan were collected over a single day in April 2012, and were taken from a 50-mile stretch of lake shore ranging from Gary, Indiana, to New Buffalo, Michigan. The sand was taken from the surface and collected in amounts of approximately 4 to 5 pounds. The sand was collected in airtight bags and was stored for two months before the experiment started. In order to optimize the data collected, the sand samples were placed in a vacuum oven and baked at 100 °C to remove any moisture contained in the sand. Once the sample had cooled it was then put through a filtering screen to remove any rocks and vegetation that it contained, to ensure the homogeneity of the sample. The samples were stored in airtight bags until ready for use. Then they were placed in a Marinelli and sealed for use.

The detector that is used is an HPGe, which is cooled to liquid nitrogen temperature and

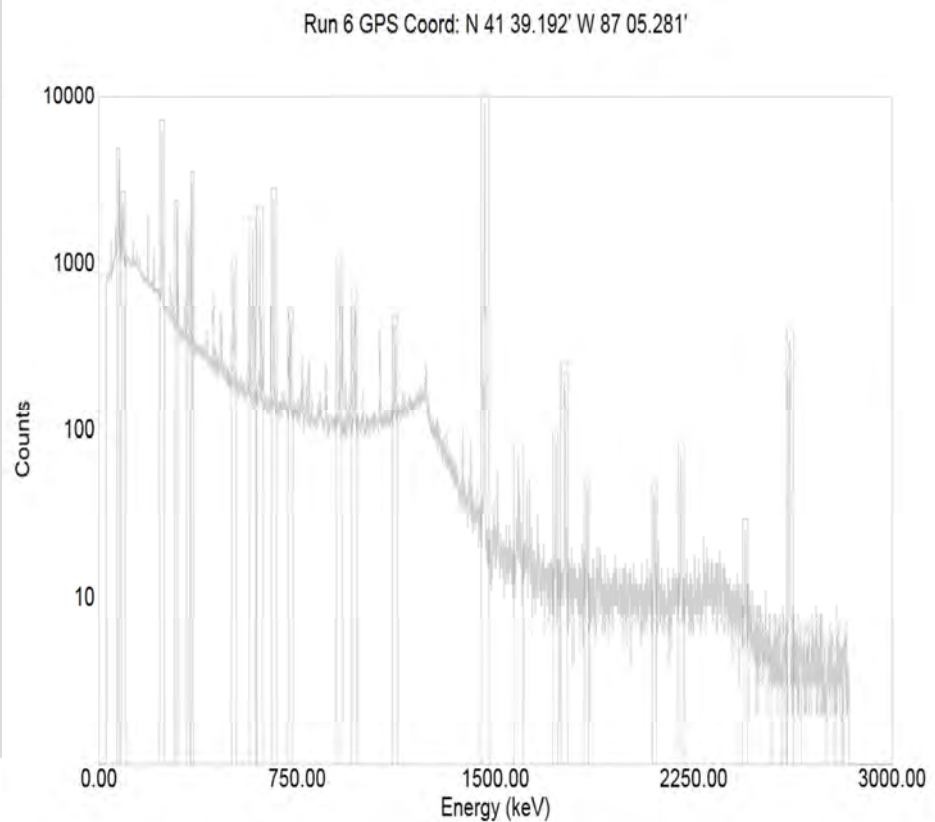
biased up to -4000V. The detector is encased in a 10 cm thick lead castle which is lined with .2 cm copper plates, to reduce background and the x-ray fluorescence from the lead castle. The detector was calibrated using a 10.00 μC Co-60 source, with the characteristic gamma lines at 1173.2keV and 1332.5keV. Because drifting can occur, the calibration was checked before each sample ran. Before the sand was analyzed, a background was collected for 172,800 seconds and was used for comparisons with each sample spectrum. Once the samples were ready for use the beaker was massed and placed on the detector where it ran for 172,800 seconds to be consistent with the background run time. The spectrums were recorded using the Maestro MCA which used the Ortec Amplifier and converted the signal from the detector to the spectrums seen.



Results

With the spectra for each run collected, a series of regions of interest (ROIs) were placed on peaks that were produced from NORM [1], [2], [3] which can be seen in the following figure:

CENTROID (keV)	nuclide
77.47	Pb and Bi
93.37	K lines
239.12	Pb-212 (Th)
295.67	Pb-214 (U)
338.71	Ac-228 (Th)
352.31	Pb-214 (U)
511.05	e-e+
583.34	Tl-208 (Th)
609.42	Bi-214 (U)
661.7	Cs-137
722.88	Ac-228 (Th)
910.94	Ac-228 (Th)
968.7	Ac-228 (Th)
1119.87	Bi-214 (U)
1459.92	K-40
1586.91	Ac-228 (Th)
1728.54	Bi-214 (U)
1763.23	Bi-214 (U)
1846.02	Bi-214 (U)
2101.94	SEP (Tl-208)
2202.37	Bi-214 (U)
2445.79	Bi-214 (U)
2612.25	Tl-208 (Th)



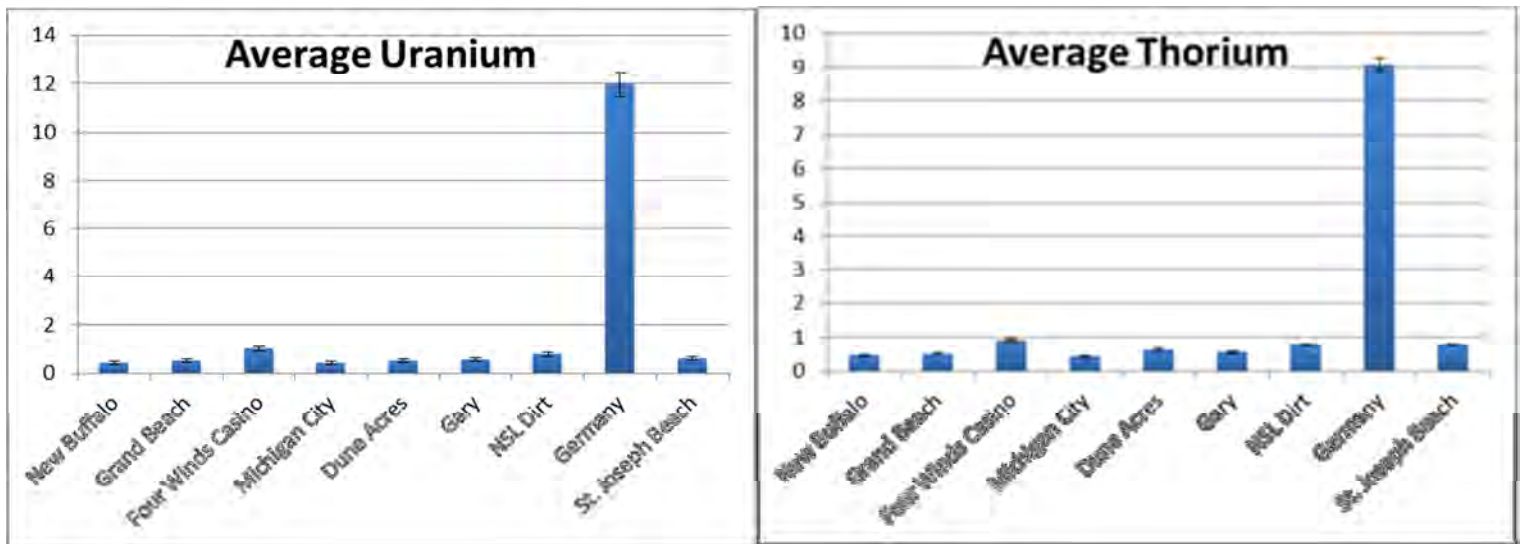
The same ROIs are used for each run, where the net number of counts and the centroid energy are the most important pieces of information from the ROIs. The ROIs are also used to look at the spectra from the background as well. In some runs the centroid energy would shift, which would take a closer look to resolve problems, sometimes this would occur because a previously unseen peak would record significant counts and displace the centroid peak. This was corrected by focusing the ROI on the targeted peak. The previously unseen peaks could be of interest for future research.

Analysis

Once the ROIs were identified for all the runs, including the background spectrum, the comparisons between samples were achieved by first subtracting the background counts from the sample spectra. This was simple to do because the background and sample collection times were the same and no scaling factor was used to subtract the background counts. The subtracted

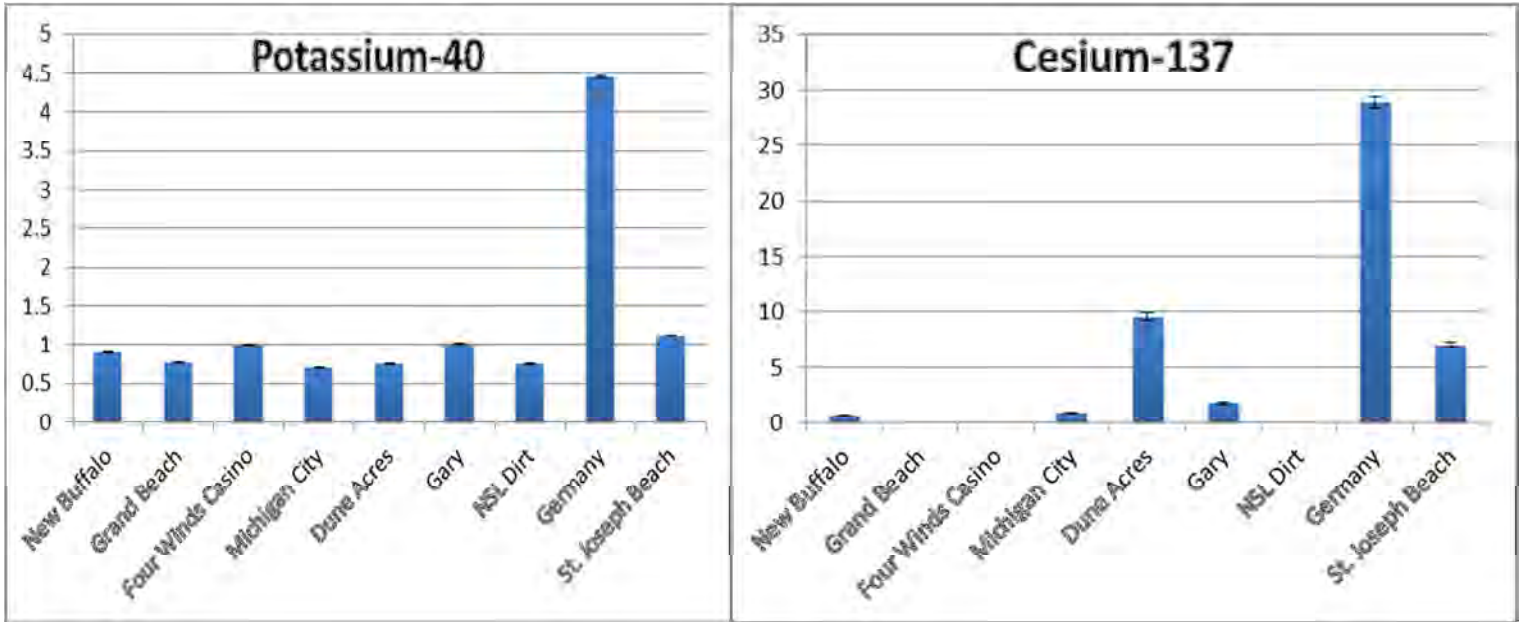
spectrums still looked similar to the unsubtracted but the significant part was that counts in certain areas changed. In order to make comparisons between samples there must be a constant that all samples could be compared to, and for this project the 5th sample spectrum was chosen for that purpose. The normalization of the spectra data was key to looking at the amount of counts in an ROI and comparing the data to other spectra. However, there were differences in the amount of sample material between runs so the normalized data was then scaled by mass to either increase or decrease the counts dependent on the mass ratio to the 5th spectrum.

Since the data had been both normalized and scaled they were easily comparable for individual peaks, but the goal was to find out whether a sample had more Uranium, Thorium, Cesium or Potassium than any other samples. For Cesium and Potassium this is simple because there is only one peak that corresponds to Cesium and Potassium. When looking at Uranium and Thorium it is more difficult because the decay chains corresponding to Uranium and Thorium have multiple daughter products, which means there is more than one line associated with Uranium and Thorium. To address this, multiple peaks corresponding to Uranium and Thorium



were taken and averaged to give the amount of Uranium and Thorium when compared to the normalization run.

The same was done for the amount of Potassium-40 and Cesium-137.



Conclusion

After performing the analysis it was clear that the most active source overall was the run consisting of rock taken from Germany. This result was expected because the rock in Germany is known to be mostly granite, which is more radioactive than other sand [1]. The second most active was a sample from New Buffalo, which had the second highest amount of Thorium and Uranium, but no Cesium and an average amount of Potassium. An interesting result was that the St. Joseph beach sand registered normal levels for all nuclides except Cesium for which it had a larger amount.

The ability to identify the entire NORM in the data spectra is important to figuring out the amount of Uranium, Thorium, Cesium and Potassium, however the results only extend to this experiment because the normalization was a run done during the experiment. The future project

could be to determine the activity of all the nuclides and figure out exactly how much is in a sample. With that known the next thing would be to determine the dosage rate a person can get by being near the beach and the corresponding NORM.

References

- [1] Malin, D., 2011, ‘Measurements of NORM in Beach Sand Samples along the Andaman Coast of Thailand after the 2004 Tsunami’
- [2] Santawamaitre, T., et al., 2010. “Study of natural radioactivity in riverbank soils along the Chao Phray river basin in Thailand” *Nuclear Instruments and Methods in Physics Research A*
- [3] Bossew, P., 2004, “A very long-term HPGe-background gamma spectrum” *Applied Radiation and Isotopes*
- [4] Eisenbud, M. and Gesell T., 1997 *Environmental Radioactivity from Natural, Industrial, and Military Sources*

Exploring the Neutron Channel of Carbon Burning
at Stellar Energies

Terri Poxon-Pearson

2012 NSF/REU Program

Physics Department, University of Notre Dame

Advisor: Xiao-Dong Tang

Abstract

The $^{12}\text{C}(^{12}\text{C},\text{n})^{23}\text{Mg}$ fusion reaction could be an important neutron donor to the weak s-process which is the stellar process responsible for forming most of the elements between iron and strontium. Carbon burning in this scenario occurs at low energies, between 2.6 MeV and 3.2 MeV in the center of mass reference frame, where the nuclear reaction cross section is both small and difficult to predict. Recently, an experiment was conducted at University of Notre Dame using direct neutron detection in order to determine the cross section at the lowest energy ever measured. This June, we used an independent experimental method which involved the detection of β^+ particles from ^{23}Mg decay in order to validate the results from the previous experiment. Results from this experiment show overall agreement, but indicated that a newly discovered resonance at 3.4 MeV may not have been as strong as originally thought. Along with these results, I will discuss possibilities and limitations for future investigations of carbon burning at astrophysically relevant energies.

1 Introduction

The weak s-process, also known as the slow neutron capture process, is responsible for forming about half of the elements heavier than iron[1]. The s-process occurs in massive stars ($>8M_{\odot}$) and its products are ejected into space after these stars end their lives in supernova explosions. The reaction believed to act as the primary neutron donor for the s-process is the $^{22}\text{Ne}(\alpha,\text{n})^{25}\text{Mg}$ reaction which occurs in both helium burning and carbon burning shells[3].

Stellar models, however, are often incomplete and oversimplified. It is possible that the neutron contribution from the $^{12}\text{C}(^{12}\text{C},\text{n})^{23}\text{Mg}$ carbon fusion reaction that was once considered negligible, may be a significant neutron source. Core carbon burning will not make an important contribution to the s-process because, after a supernova explosion, most of the core will not be ejecting but, instead, form the basis for a neutron star or black hole, depending upon the original star's mass [2]. Therefore, the only possible site for the $^{12}\text{C}(^{12}\text{C},\text{n})^{23}\text{Mg}$ reaction to play a role is in the carbon burning shell. The typical temperature is between 1 and 1.2 GK, which define the important astrophysical energy range as above the threshold value of 2.6 MeV and below 3.2 MeV in the center of mass frame[4].

The nuclear reaction cross section for the neutron channel of carbon burning is not well known at astrophysically relevant energy levels that lie below the coulomb barrier. Below about 5.6 MeV in the center of mass system, these heavy ions do not have enough energy to overcome the coulomb repulsion from the positively charged nuclei [4]. At lower energies, reactions occur as a result of quantum tunneling effects. This greatly reduces the cross section of the reaction and makes it very difficult to measure experimentally[5]. Even the lowest experimental results stop at 3.7 MeV, well above the astrophysical energy range corresponding to

carbon shell burning. This experiment seeks to further explore carbon fusion at low energies and, once the cross section is better known, the results provide an opportunity to test and improve current stellar models.

2 Experimental Methods

2.1 Neutron Counting

Recently, an experiment was performed at the University of Notre Dame to determine the low energy cross section of the $^{12}\text{C}(^{12}\text{C},n)^{23}\text{Mg}$ nuclear reaction. This experiment used a ^3He neutron counter array to determine the ^{23}Mg yield. This detection method used 20 ^3He proportional counters arranged in concentric circles within a high density polyethylene. A ^{12}C beam was aimed at a thick, highly ordered pyrolytic graphite target (HOPG). HOPG is a graphite target containing primarily natural carbon, with a structure that minimized many contaminants such as H_2O and D_2O . The target was placed in the center of the polyethylene block. The neutrons produced by the nuclear reaction were slowed down by the polyethylene and detected by the surrounding counters. The detector had an efficiency above 40% according to a GEANT4 simulation and the basic experimental setup can be seen in Figure 1.

Using this method, it is impossible to discriminate between neutrons produced from the desired carbon fusion reaction and those produced in other contaminant reactions. The neutron contribution from the $\text{D}(^{12}\text{C},n)^{13}\text{N}$ reaction was minimized by using the HOPG target instead of an ordinary graphite target, but there was still a sizeable contribution from the ^{12}C beam fusing with ^{13}C that makes up 1.1% of the target, by mass. In order to minimize this contaminant, a ^{13}C beam bombarded the thick HOPG target. In this setup, the $^{12}\text{C}(^{13}\text{C},n)^{24}\text{Mg}$ reaction was assumed to dominate neutron production. The absolute neutron yield determined by this scan could then be subtracted from the results of the original neutron scan. The corrected neutron yield was then converted to the nuclear reaction cross section for the $^{12}\text{C}(^{12}\text{C},n)^{23}\text{Mg}$ reaction.

This experimental method allowed for measurements to the lowest energies ever achieved. The new results discovered a predicted resonance around 3.4 MeV and agreed with past cross section measurements. Results from this experiment are summarized in Figure 2.

2.2 Beta Counting

This summer, we conducted another low energy scan using an independent experimental method in order to validate the results obtained in April's experiment. Instead of directly measuring the neutron production from the $^{12}\text{C}(^{12}\text{C},n)^{23}\text{Mg}$ reaction, we measured the decay products of the radioactive ^{23}Mg which is produced

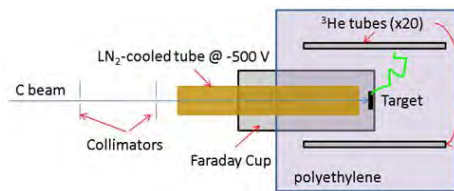


Figure 1: Neutron Detection Setup

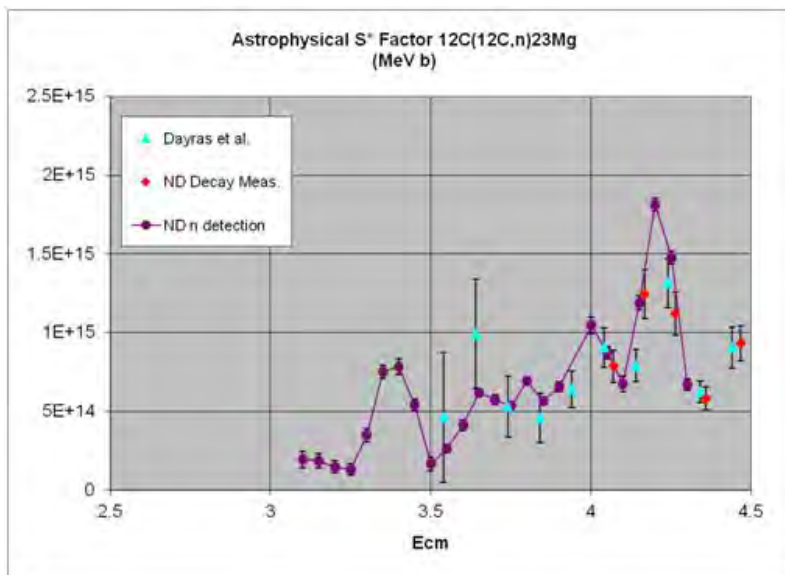


Figure 2: Neutron Detection Experimental Results

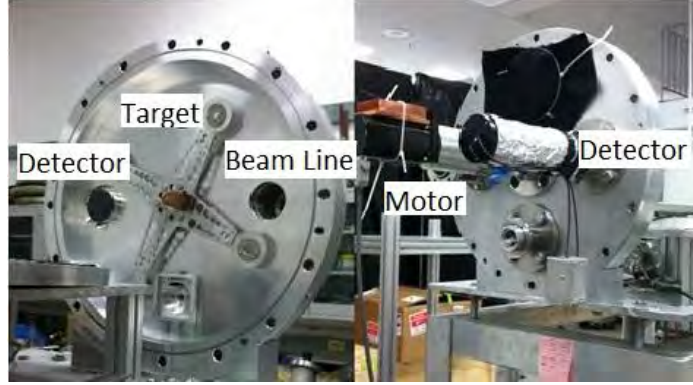


Figure 3: Beta Counting Experimental Setup

during carbon fusion. ^{23}Mg has a half life of 11.32 seconds. When it decays via β^+ decay, it produces ^{23}Na and a positron. In this experiment, we measured the β^+ particles using a plastic scintillator.

Like the neutron counting experiment, we used a beam of ^{12}C ions and a thick HOPG target. HOPG was still preferable to graphite because, although the neutrons produced in the $\text{D}(^{12}\text{C},\text{n})^{13}\text{N}$ reaction are no longer problematic, the ^{13}N produced by $\text{p}(^{12}\text{C},\gamma)^{13}\text{N}$ and $\text{d}(^{12}\text{C},^{13}\text{N})\text{n}$ decays via β^+ decay with a half life of about 10 minutes. The $^{12}\text{C}(^{13}\text{C},\text{n})^{24}\text{Mg}$ contaminant channel, however, is not problematic using a β^+ detection method. The experimental setup included a wheel with rotating arms controlled by a motor. The target was attached to one arm on the wheel and was positioned in the beam line. After the target was irradiated for 30 seconds, the wheel turned and the target was moved away from the beam and positioned in front of the scintillator detector. The DAQ activated and collected data from the detector. After 30 seconds, the DAQ shut off, the wheel span to position the target in the beam line, and the process began again. The cycle was repeated until there were a sufficient number of β^+ particles detected. The $^{12}\text{C}(^{12}\text{C},\text{n})^{23}\text{Mg}$ reaction was studied in the energy range of 3.1 to 4.3 MeV in the center of mass reference frame. Figure 3 shows an image of the apparatus.

3 Analysis

3.1 Determining the Best Analysis Method

I considered two basic methods for analyzing the data acquired from the β^+ decay experiment. Both analysis methods used ROOT, an analysis program developed by CERN for high energy physics. The first method involved using a fit line for the exponential decay of ^{23}Mg . This method assumes that the decays detected by the scintillator come from the exponential decay of ^{23}Mg sitting on top of a flat background. The fit lines

created by this method conformed to the data fairly well, giving reduced χ^2 values that range from 0.87 to 1.34 with the average value being 1.06.

The second possible method disregarded the shape of the exponential decay and, instead, only attempted to count the total number of decays from ^{23}Mg within the counting period. To do this, I determined a background rate and subtracted it from the total number of β^+ particles detected. I calculated the background by integrating over the last third of the counting period and scaling these counts to the first two thirds of the period. I then integrated over the first two thirds and subtracted the scaled background measurement. Because ^{23}Mg has a short, 11 second half-life, the ^{23}Mg population has undergone almost 2 complete half-lives, by the time two thirds of the counting period has passed, leaving only about 25% of the original yield. In the last third of the cycle, only about half of that 25% is expected to decay. These decays, however must be accounted for in order to compare the yields determined by both methods. To do this, the yields determined by this method must be scaled by a factor that represents the ratio of the decays in the last third to the decays in the first two thirds of the counting period. In this case, that ratio is 0.6

I then scaled the fit line used in the first method to the first two thirds of the counting period so that I could directly compare the results for ^{23}Mg yield obtained from the two methods. The results from that comparison can be seen in Table 1. The deviations were calculated using Equation 1. The two methods are within one σ of one another for almost every energy level and this indicates that there is good agreement between the methods.

$$\sigma = \frac{|Yield_1 - Yield_2|}{\sqrt{\delta_1^2 - \delta_2^2}} \quad (1)$$

Because of the low statistics at the lowest energy level, there was a possibility that the fit line generated by ROOT could be one of many possible fit lines and would not be a good indicator of the actual yield. The agreement between the two analysis methods indicates that the fit lines were, in fact, valid and I could continue using them for the remainder of my analysis.

3.2 Determining Absolute Yield and Comparing with Past Data

In order to convert between the measured ^{23}Mg yield and the absolute yield, a few things have to be taken into consideration. First, the data must be normalized to account for the strength of the beam current and the time of the run. Additionally, a correction must be made for the efficiency of the detector which was estimated to be about 48.6% based on past experimental results. The calculation for absolute yield should also take into account decays that occurred during the periods when the wheel was moving between the end of radiation and the beginning of data acquisition. Finally, corrections must consider the ^{23}Mg

Table 1: Comparing Analysis Methods

Energy	Fit Line (Method 1)		Integration(Method 2)		Comparison
Ecm (MeV)	23Mg Yield	Error	23Mg Yield	Error	Deviation
3.1	67.03	419.87	481.67	408.25	0.70
3.3	849.83	553.61	2040	529.14	1.55
3.4	668.17	325.31	905	311.72	0.53
3.5	722.20	244.69	1023.33	229.76	0.90
3.6	688.74	193.56	588.33	183.25	0.38
3.7	617.01	120.10	478.33	114.01	0.84
3.9	701.49	113.66	845	100.37	0.95
4.1	1297.25	129.74	1418.33	110.37	0.71
4.3	1049.69	106.72	1271.67	89.46	1.59

on the target that continued to decay, even after the 30 second count period ended, causing contributions from previous cycles during each counting period. Although this contribution is nearly negligible, I included possible contributions from the past two cycles in my absolute yield calculation. Equation 2 takes all of these factors into account and was used to determine the absolute yield. I could then directly compare this data with the yields determined from the previous neutron counting experiment.

$$Y_{abs} = \frac{Dt_1 2e}{Q\eta\tau} \frac{1}{(e^{t_1/\tau} - 1)(e^{-t_2/\tau} - e^{-t_3/\tau})(1 + e^{-t_4/\tau} + e^{2t_4/\tau})} \quad (2)$$

where

$$t_0 - t_1 = \text{Irradiation} \quad t_1 - t_2 = \text{Motion}$$

$$t_2 - t_3 = \text{Counting} \quad t_3 - t_4 = \text{Motion}$$

$$D = \text{DetectedDecays} \quad Q = \text{TotalCharge} \quad \eta = \text{DetectorEfficiency} \quad \tau = \text{MeanLife}$$

The data sets from the two experiments are plotted in Figure 4. As the figure demonstrates, the two data sets agree very well and most points agree within their error bars. Additionally the deviation between the two data sets is small and, in most cases, less than one. The reduced χ^2 value for the two data sets is 1.93. The data used to compare the absolute yields can be found in Table 2. The χ^2 value is the sum of the deviations and the reduced χ^2 value divides the χ^2 value by the number of degrees of freedom.

The data from the β^+ experiment produces some interesting results. First, the yield calculated from the β^+ method is consistently higher than the yield resulting from the neutron counting method. One possible explanation for this would be a flaw in the correction for the $^{12}\text{C}+^{13}\text{C}$ reaction in the neutron experiment. It is possible that the contamination from this source was overestimated, particularly at lower energies, leading to an over subtraction of neutrons. This may offer some insight as to why the yield at 3.3 MeV is significantly higher in the β^+ yield. If contaminant neutrons were being over subtracted, particularly at lower energies,

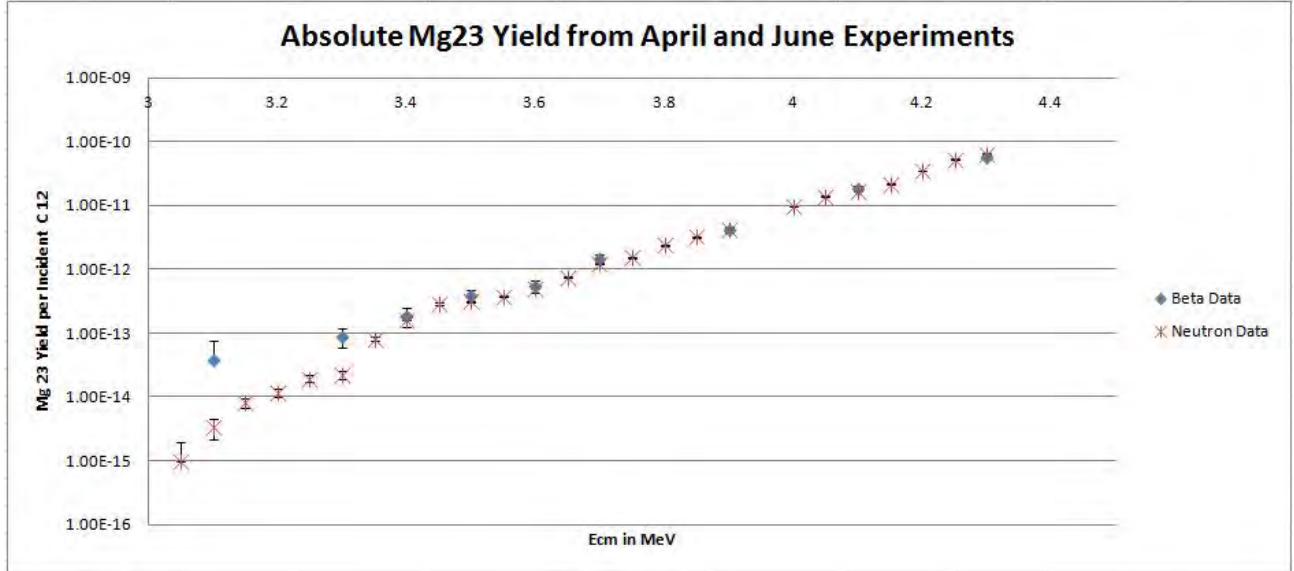


Figure 4: Comparison of 23Mg Yield

Table 2: Comparing Absolute Yields

Energy Ecm (MeV)	Beta Experiment		Neutron Experiment		Comparison Between Methods			
	Yield	Error	Yield	Error	Difference	Deviation	Chi 2	Reduced Chi 2
3.1	3.70E-14	3.96E-14	3.28E-15	1.13E-15	-3.37E-14	0.726	13.50	1.93
3.3	8.81E-14	2.78E-14	2.25E-14	3.10E-15	-6.56E-14	5.48		
3.4	1.85E-13	5.80E-14	1.61E-13	6.02E-15	-2.35E-14	0.16		
3.5	3.85E-13	8.22E-14	3.17E-13	8.28E-15	-6.79E-14	0.68		
3.6	5.42E-13	1.22E-13	5.01E-13	1.25E-14	-4.19E-14	0.11		
3.7	1.46E-12	2.23E-13	1.23E-12	1.94E-14	-2.31E-13	1.06		
3.9	4.21E-12	3.95E-13	4.22E-12	5.32E-14	8.53E-15	0.00		
4.1	1.86E-11	1.27E-12	1.67E-11	3.47E-13	-1.93E-12	2.14		
4.3	5.80E-11	3.45E-12	6.42E-11	6.49E-13	6.23E-12	3.18		

this would exaggerate the resonance discovered in the neutron experiment.

4 Conclusions and Limitations

In general, there is good agreement between the ^{23}Mg yield determined by this experiment and the yield previously determined by the neutron experiment. The discrepancy at 3.3 MeV indicates that the newly discovered resonance at 3.4 MeV may not be as strong as was originally thought. Still, the new data indicates that there is a resonance at this energy level. Finally, the yield from the neutron counting experiment is consistently lower than the yield determined by the β^+ method. One possible explanation for this trend is that neutrons were over subtracted when correcting for the $^{12}\text{C}(^{13}\text{C},n)^{24}\text{Mg}$ contamination.

Although these experiments have probed the lowest energies ever measured, there are many factors that

limit our ability to explore all the way down to astrophysically relevant energy levels. At low energies, the cross section is so low that the experiment must run for a long time, still creating few events. A higher beam current, like that expected from the new accelerator at Notre Dame, should help increase the number of decays observed at low energy and serve to decrease the error bars during analysis. Secondly, the photomultiplier tube used in the current detector has intrinsic noise, even when the beam is not running. These false signals are impossible to differentiate from β^+ decays. Additionally, cosmic rays are a source of background noise in the detector. These two effects, combined, dictate the energy level where background noise dominates actual β^+ decays and, therefore, the lower limit for experimental measurement.

References

- [1] B Bucher, J Browne, S Almaraz-Calderon, A Alongi, A D Ayangeakaa, A Best, M Couder, J DeBoer, X Fang, W Lu, M Notani, D Patel, N Paul, A Roberts, R Talwar, W Tan, X D Tang, A Villano. The Role of $^{12}\text{C}(^{12}\text{C},n)$ in the Astrophysical S-Process.
- [2] Dayras, R., Z. E. Switkowski, and S. E. Woosley. "Neutron Branching in the Reaction $^{12}\text{C}+^{12}\text{C}$." Nuclear Physics A279 (1977): 70-84.
- [3] Pignatari, M., R. Gallino, M. Heil, M. Wiescher, F. Kappeler, F. Herwig, and S. Bisterzo. "The Weak S-Process in Massive Stars and Its Dependence on the Neutron Capture Cross Sections." The Astrophysical Journal 710 (2010): 1557-577.
- [4] Patterson, J. R., H. Winkler, and C. S. Zaidins. "Experimental Investigation of the Stellar Nuclear Reaction $^{12}\text{C} + ^{12}\text{C}$ at Low Energies." The Astrophysical Journal 157 (1969): 367-73.
- [5] C.A. Barnes, S. Trentalange, and S.C. Wu. Heavy ion reactions in Nuclear Astrophysics." Treatise on Heavy-ion Science, edited by D.A. Bromley, Vol. 6, p.3 (Plenum, New York, 1985).

ASIC Data Acquisition System; Implementation of HINP16C on SAND

Michael Robbe

2012 REU Program

Physics Department, University of Notre Dame

Advisors: Dr. Wanpeng Tan

Dr. Ani Aprahamian

ABSTRACT

Silicon-based particle detectors can be made to be highly segmented with a large surface area, allowing the detector to produce vast amounts of information in the form of energy and timing signals. In order to process so much information, high density signal processing is required. The signals emitted from the particle detector must be amplified and shaped before they can be converted for use by a computer. The traditional readout setup for particle detectors requires separate modules to accomplish the tasks of amplifying, shaping, and converting the signal, and a single channel on a detector requires each of these modules. If highly segmented silicon arrays are being used in an experiment, the traditional setup can be incredibly expensive and impractical. The Application Specific Integrated Circuit (ASIC) system, in comparison to the traditional setup, is far more cost-efficient when used in experiments that require highly segmented silicon arrays. The ASIC system at the University of Notre Dame allows researchers to use up to 512 channels to process the energy and timing signals produced by the detector, all within a box of approximately 40 x 15 x 10 cm in volume. We tested linearity, resolution, and quality of the chips (HINP 16C) used in the ASIC system. This system will be used with a new silicon detector array (SAND), developed at Notre Dame.

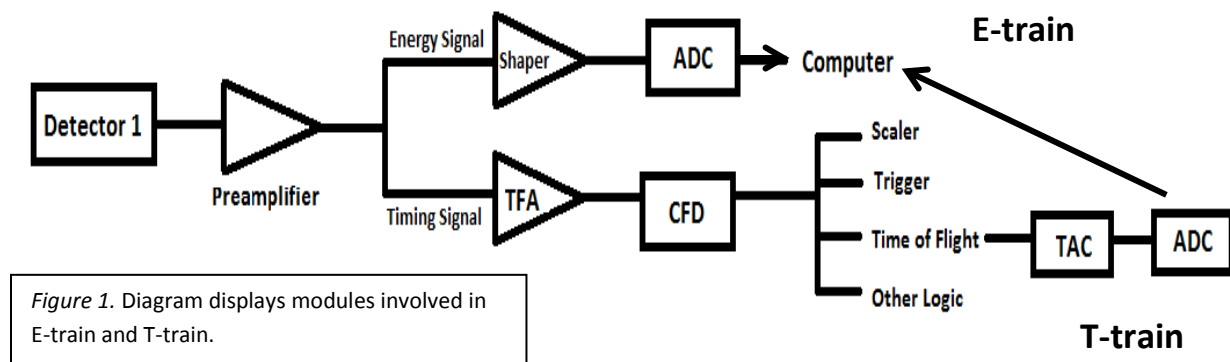
1 Background Information

1.1 The Particle Detection System

When a charged particle strikes a semiconductor-based particle detector, electrons in the detector are displaced and the structure of the material is disturbed. This event results in a flow of charge along a narrow strip made up of a conducting

material (aluminum is often used), and the charge is measured by a sensitive electronic readout channel at the end of strip³. The signal is amplified, shaped, and converted to a digital format by a series of modules and then interpreted by a computer to determine certain characteristics of the particle. Such characteristics include the kinetic energy, momentum, and velocity of the particle, and the time when the event occurred.

A signal produced by a collision with the detector must be processed by a series of modules before it can be interpreted by a computer. First, the signal is extracted from the detector by the preamplifier. This must be done without significantly degrading the signal-to-noise ratio (SNR), so the preamplifier is located as close as possible to the detector. From the preamplifier, the information is relayed in the form of energy and timing signals. The energy signal feeds the E-train branch for processing, while the timing signal feeds the T-train branch².



The energy signal is first slowly shaped into a peak with attributes that can easily be interpreted to have physical implications (i.e. amplitude, FWHM, area, centroid). The amplitude of the peak is digitized by the Analog-to-Digital-Converter (ADC) for computer display. The timing signal, on the other hand, is first amplified by the Timing Filter

Amplifier (TFA) until the threshold is reached. This will trigger a square wave signal in the CFD module. The time-of-flight information inherent in the signal is then relayed to two separate converters, the TAC and the ADC, which together effectively act as a time-to-digital converter¹. This signal is now digitized for computer display.

1.2 Germanium and Silicon Particle Detectors

In the traditional setup for particle detection systems, every channel on a silicon- or germanium-based particle detector requires each of the modules previously discussed in order to process the information sent from the detector. The traditional setup works well for experiments that require extremely high energy resolution of the generated peaks. This is because the noise level is inherently low in this setup, so the SNR can be kept above 1.0 when used with either a silicon- or germanium-based detector. High-purity germanium detectors are able to produce better energy resolution (displayed as FWHM) than silicon detectors, but also generally produce more unwanted noise. Consequently, the noise of the signal-processing setup must be at an inherently low level in order for the SNR of a high-resolution germanium detector to be kept above 1.0. High-purity germanium detectors are commonly used for experiments involving gamma-ray spectroscopy, as the natural range for γ -rays emitted by nuclei is 0.1-20 MeV, and high resolution is necessary.

Silicon-based particle detectors are able to determine the position of particles within 10 μm and have a time response of 25 ns. Silicon detectors can be made to be highly segmented into several narrow strips, and arranged in an array of the desired geometry. Each strip on the detector corresponds to several channels; the channel processes the electric signals delivered by the conducting strip after a particle collides with the detector. A silicon detector's capacity for high segmentation allows for very accurate measurements of a particle's position.

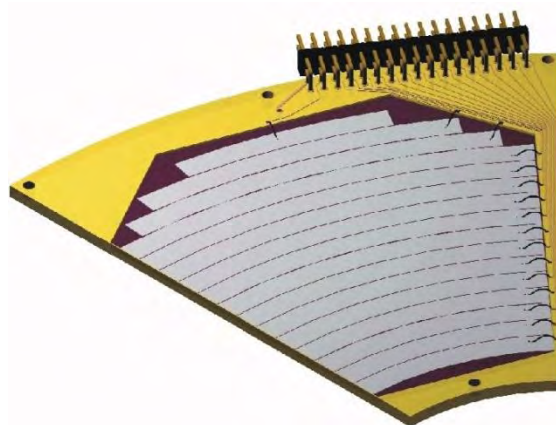


Figure 2. Silicon Detector (YY1) Manufactured by Micron Semiconductor, Ltd. Notice there are 16 distinct single-sided silicon strip detectors arranged radially. Six of these units can be placed in a “lampshade” arrangement to cover a large angular range.

Each individual silicon detector (e.g., YY1 shown in Figure 2) may possess a relatively large surface area, and multiple detectors can be used in an array to span a large angular range within a chamber. This setup is useful for tracking a particle's trajectory after a collision event⁴. The use of multiple detectors, however, means there are often several hundreds of channels producing signals. These signals must somehow be amplified, shaped, and converted to a digital format before they can be interpreted.

1.3 The ASIC System and its Benefits

The University of Notre Dame has been working in collaboration with Indiana University to develop a silicon detector array of its own, known as SAND (Silicon Array at Notre Dame). SAND will be used for experiments examining phenomena such as carbon

burning, the ap process, and CNO breakout. SAND requires a readout of 240 channels that the ND ASIC system will provide².

Typically, the cost per channel of a commercial ADC is in the range of \$150¹. When running experiments that require data from several hundreds of channels, ADCs and TDCs become very expensive. So expensive, in fact, those experiments – when run in the traditional electronic readout setup – are not viable options for laboratories on a modest budget. An experiment run with SAND, for example, would cost the university upwards of \$200,000.

The Application Specific Integrated Circuit (ASIC) setup for silicon detector arrays was

#Channels	ASIC	Conventional (other cost not included)
512	\$18.77k + <10k	\$444.8k
256	\$15.17k + <10k	\$222.4k
160	\$13.82k + <10k	\$139k

Figure 3. Chart compares costs of the conventional readout setup to the Integrated Circuit setup.

developed in 2005 and is a much cheaper alternative to the conventional readout setup. The ASIC system is also far more compact and requires fewer cables and modules. This system is

currently being used by schools like MSU, IU, LSU, and TAMU.

The chip that will be used in the ASIC system for SAND is HINP16C. Each of the 16 channels of HINP16C consists of a charge-sensitive amplifier (CSA). The CSA output is split to feed energy and timing branches, both of which produce sparsified pulses that undergo off-chip digitation through a pipeline ADC¹. A central common channel on HINP16C provides the bias for the 16 processing channels, contains the readout electronics, and contains the circuits used for configuring the 16 channels. In this way, signals from multiple channels can be processed by a single ADC unit.

The ASIC system at the University of Notre Dame implements a motherboard that has the capacity for 16 chipboards. There are 2 HINP16C chips per chipboard, and each chip contains 16 processing channels. In total, the ASIC system at Notre Dame allows researchers to use up to 512 channels to process the energy and timing signals produced by the detector, all within a box of approximately 40 x 15 x 10 cm in volume. A drawback to the ASIC setup is that the inherent noise level of the entire system is increased. This doesn't present a significant problem for silicon detector arrays, but it does mean that the ASIC setup can't currently be used with high-resolution germanium detectors because the SNR could not feasibly be kept above 1.0 for an extended period of time.

2 Testing

2.1 Testing Linearity of HINP16C Preamplifiers

This summer we ran a variety of tests to determine certain attributes of the ASIC system. We examined the linearity of the HINP16C Preamplifiers by using the GUI and SpecTCL software while varying pulse [v] within the range of 0.025v to 3.6v. Centroids of the resulting peaks were measured using Xamine software. We recorded runs for all channels; 32 channels

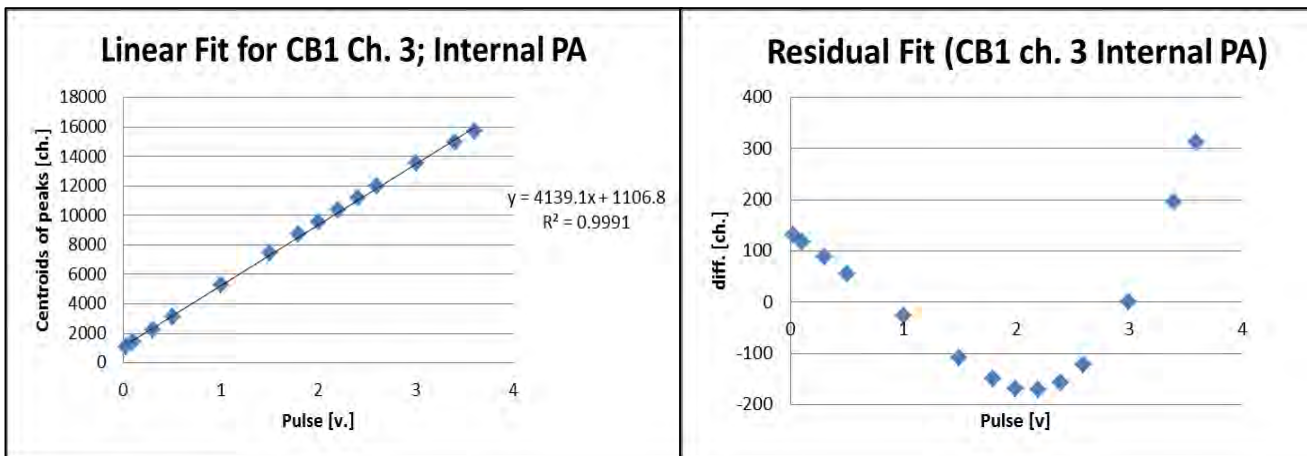
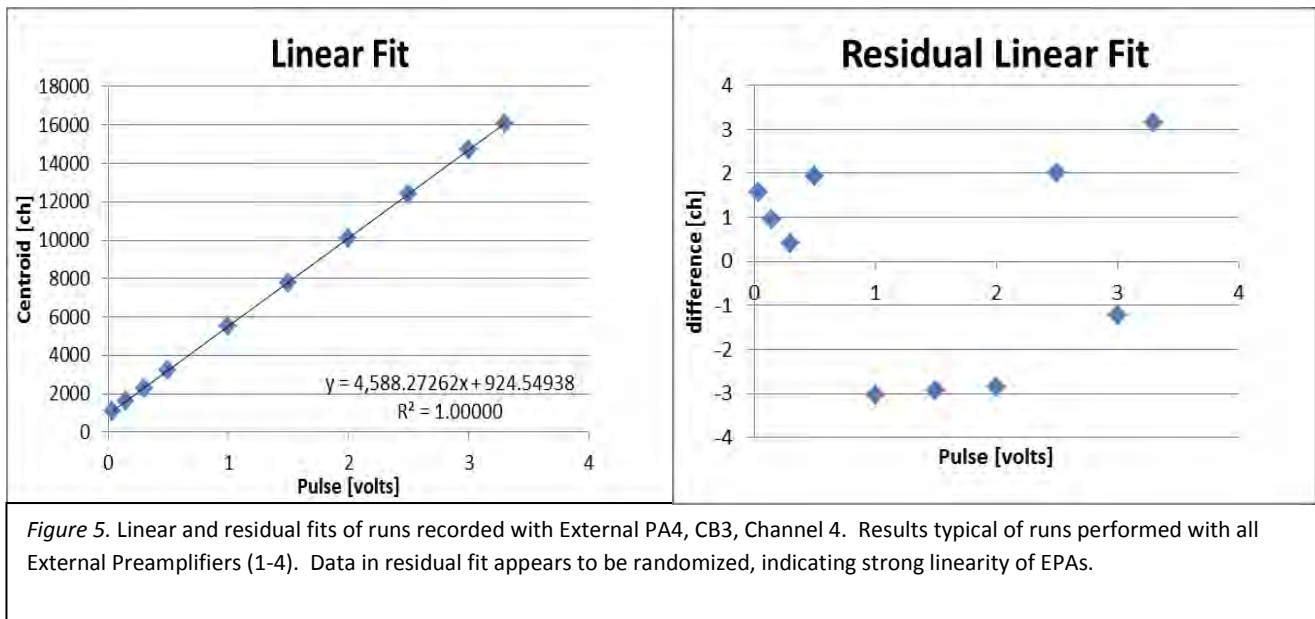


Figure 4. Linear and residual fits of runs recorded with Internal Preamplifier (IPA), Chipboard 1 (CB1), Channel 3. Results typical of all runs performed with IPA. Notice that residual fit is not randomized, but instead data follows a distinct curve.

per chipboard, chipboards 1-8. When the internal pre-amplifier of HINP16C was used, the runs produced data that showed poor linearity. This is shown by the residual fit of the data in Figure 4, which followed a distinct curve instead of being randomized.

The runs performed with the external preamplifiers, however, showed much stronger linearity. The pulse [v] was varied within the range of 0.04v to 3.3v, and the centroids [ch.] of the generated peaks were measured. As shown in Figure 5, the randomized residual fit and R^2 value of 1.00000 for this run indicate very strong linearity for the EPAs. A particle detection system with strong linearity can be calibrated using only 2 test points from an alpha source, whereas a system that is more accurately described by a polynomial fit, for example, requires far more test points to calibrate.



2.2 Energy Resolution of HINP16C

We recorded runs for 16 channels on CB3 for all external PAs, using ^{148}Gd and ^{241}Am as alpha sources. The resulting peaks were analyzed and the Centroid, FWHM, and Area were

recorded. Figure 6 shows a typical run for this setup. The peaks shown in Figure 6 possessed

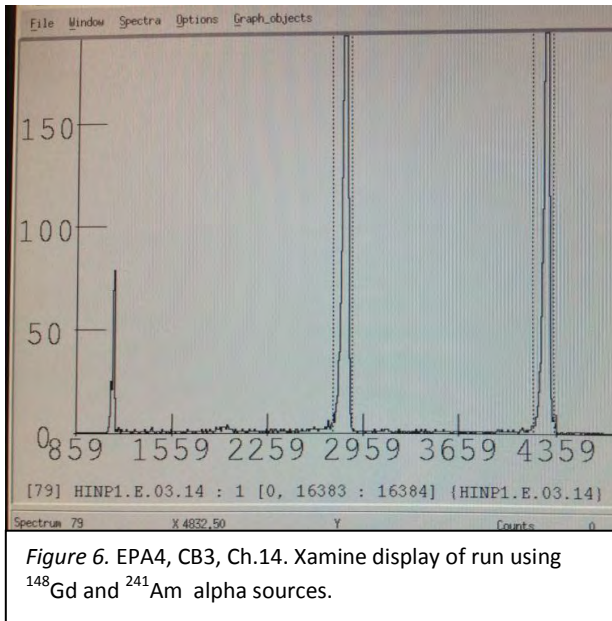


Figure 6. EPA4, CB3, Ch.14. Xamine display of run using ^{148}Gd and ^{241}Am alpha sources.

FWHMs of 49.277 channels and 47.685 channels (left to right). The standard definition for energy resolution is:

$$R = \text{FWHM} / \text{Position of Peak}$$

The energy resolutions of the peaks are 1.747% and 1.111%, respectively. The FWHM can be

converted to energy (keV) by using the linear calibration of the channel. The resolutions of the

peaks derived from the external preamplifiers were determined to be less than 30 keV⁸.

2.3 Threshold Levels at Varying Discriminants

HINP16C threshold voltages were measured for chipboards 1-8 on channel 0. Channel 0 produced results typical of all channels. Discriminants were varied and results for each

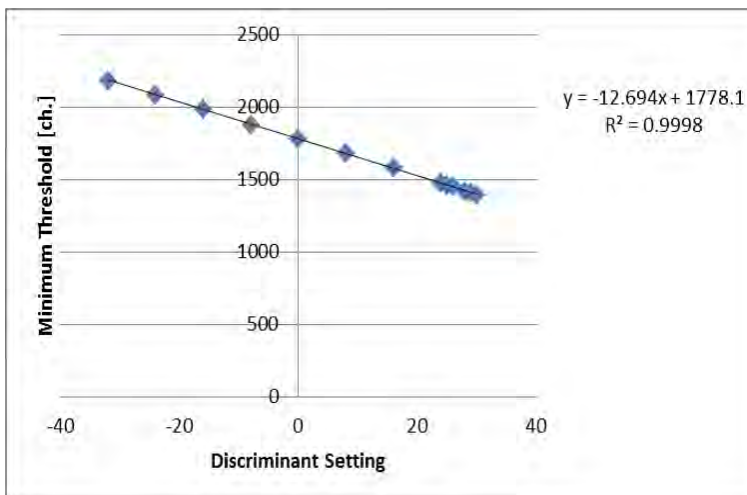


Figure 7. Minimum threshold levels at varying discriminants. Showed high linearity. Results typical of all chipboards.

discriminant were recorded. Minimum threshold levels for HINP16C varied linearly with the discriminant setting on the Motherboard. Discriminants were adjusted in increments until noise levels became greater than the minimum threshold voltage. At this point the SpectCl readout software

would overload due to noise. The threshold at which this occurs allows one to determine noise levels inherent in the system for every chipboard that was tested.

3 Conclusion

Linearity, resolution, and quality of HINP16C in the ASIC system were tested. We have concluded that the internal preamplifier in HINP16C did not show strong linear character. The external preamplifiers, however, demonstrated strong linearity, with a typical R^2 value of 0.99999 for a linear fit. The external PAs will therefore be used with the ASIC system in future experiments.

Inherent noise levels varied by chipboard, but were found to be as low as 0.1986v (CB6, Ch.0, Discriminant set at -22). These results helped us to choose which type of cable would be connected to the silicon detector inside the particle chamber. There were two options: the stiff and expensive, but well shielded, coaxial cables, or the cheaper and more flexible option. We determined that the noise levels of the cheap and flexible cables were comparable to the coaxial cables, so they will be the ones used in future experiments.

4 References

- [1] Engel, G., et al. "A multi-channel integrated circuit for use in low- and intermediate-energy nuclear physics—HINP16C". *Science Direct*. Nuclear Instruments and Methods in Physics Research A 573 (2007). 418-426
- [2] Tan, W. "The New ASIC Data Acquisition System at Notre Dame". University of Notre Dame. Web. 31 July 2012.
<https://www.nd.edu/~nucstruc/documents/DAQ%20Electronics/asic_data_acq_update.pdf>.
- [3] Montañó, L. "Silicon microstrip detectors". University of Michigan. Web. 30 July 2012.
<<http://www.ifm.umich.mx/vwillanu/XWORKSHOPPAGE/LuisMMontano.pdf>>.
- [4] Hartmut, F., et al. "Applications of Silicon Detectors". *IEEE Transactions on Nuclear Science* (2001). Vol 48, No. 4, 933-940.

Magnetic Properties of GaAs/Fe Radial Heterostructured Nanowires

Lindsay I. Sonderhouse*

2012 NSF/REU Program,

Physics Department,

University of Notre Dame

(Dated: August 3, 2012)

ADVISORS: Jacek Furdyna and Margaret Dobrowolska, and Xinyu Liu

ABSTRACT

In this research we study the magnetic properties of GaAs/Fe radial heterostructured nanowires grown on GaAs substrates by Molecular Beam Epitaxy (MBE). By comparing the Ferromagnetic Resonance (FMR) response from a series of nanowire samples grown in different orientations, we can identify which parts of the signal correspond to the nanowire contribution. Since there is no direct theory for our nanowire samples, we provide a phenomenological argument for our results. We find that the resonant field of the nanowires is lowest when the applied magnetic field is along the wires and highest when it is perpendicular to the nanowires. This suggests that the preferred direction for magnetization in the nanowires lies along the longitudinal axis, while the hard axis is radial.

INTRODUCTION

Magnetic nanostructure research has recently received a great deal of interest due to the opportunities for spin-based electronics [1] and high density memory storage [2] applications. The vapor-liquid-solid growth process [3] for growing semiconductor nanowires by molecular beam epitaxy (MBE) allows for the realization and study of new magnetic nanostructures. The GaAs/Fe core/shell nanowire structure used in this research is obtained by growing GaAs nanowires on a GaAs substrate using MBE, coating the nanowires with Fe by Atomic Layer Epitaxy (ALE), and then capping Fe with Au to prevent oxidation using ALE. This process results in a GaAs core surrounded by a magnetic Fe cylindrical shell.

This research seeks to understand the magnetization of single-domain nanowires through the response of Ferromagnetic Resonance (FMR), an extremely precise and contactless ensemble measurement. We perform FMR on samples with various morphologies. Our results for (111B) GaAs do not display a signal from the nanowires due to the overlap of easy axes and hard axes among the thin film and the nanowires. To resolve this issue, we grow obliquely oriented nanowires. This removes the overlap of easy and hard axes and should largely produce independent signals between the thin film and the nanowires.

EXPERIMENTAL METHODS

Growth

Our samples are grown using Molecular Beam Epitaxy (MBE) at The University of Notre Dame. The MBE machine consists of an ultrahigh-vacuum chamber that has a base pressure around 1×10^{-9} torr [4] along with separate chambers that hold isolated growth elements. The growth process works as follows. First a few monoatomic layers of Au are deposited by Atomic Layer Epitaxy (ALE). Then the Au is annealed at approximately 55° C for 60 minutes under an As rich environment. This produces Au nanodroplets with an average diameter of (60 ± 20) nm. Next GaAs is grown with a substrate temperature of 600° C. These Au droplets behave as a catalyst for growth. The Au attracts GaAs and nanowires grow directly underneath and up from the Au. The nanowires grow with a radius equal to the radius of the Au droplet and a length determined by how long GaAs is grown. Using ALE, our nanowires are then coated with Fe and capped with Au to prevent oxidation. Our samples have the following amounts of Fe. Sample C was exposed to Fe for 20 minutes, while samples A and B were exposed for 40 minutes. For more information on MBE, including the machine and the growth process, see Kritsanu Tivakornsasithorn's PhD thesis [4].

Ferromagnetic Resonance

When an applied magnetic field is incident on an electron, its magnetic moment precesses about its equilibrium orientation. However, if the total field is at an angle, the field produces a torque on the moment, tending to align the moment with the magnetic field. Therefore, given time, the magnetic moment will precess about the total magnetic field. Inside a material, this total magnetic field is called the effective field, and is composed of many parts, including the applied magnetic field and any geometrically dependent internal fields within the material such as the demagnetization field. For a single-domain ferromagnetic material, all of the magnetic moments are in the same direction due to the strong exchange force between moments. Thus we can treat all the individual moments as a collective moment,

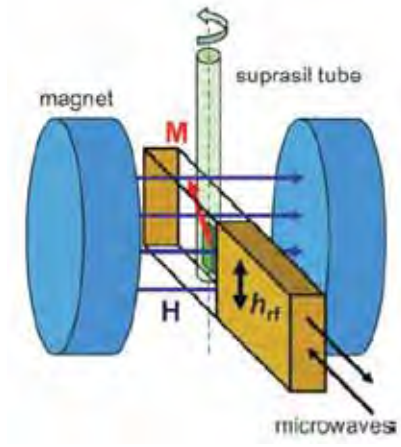


FIG. 1: Schematic diagram of a portion of the experimental setup. Shown here are two Helmholtz coils, the quartz tube containing the sample, and the orientations of the microwave fields.

called the magnetization. The equation of motion that governs the system is:

$$\dot{\vec{M}} = \gamma \left(\vec{M} \times \vec{H}_{eff} \right), \quad (1)$$

where \vec{M} is the magnetization and $\gamma \approx 2$ is the gyromagnetic ratio.

Let us pick our coordinate system such that the effective field lies in the z-direction and assume a general form for \vec{M} given this orientation: $\vec{M} = (m_x \hat{x} + m_y \hat{y}) e^{i\omega t} + M_s \hat{z}$, where m_x and m_y are constants, M_s is the saturation magnetization, and ω is the frequency at which the magnetization precesses. Plugging \vec{M} and \vec{H}_{eff} into Equation 1 gives us

$$\frac{d}{dt} \begin{pmatrix} M_x \\ M_y \end{pmatrix} = \gamma \begin{pmatrix} 0 & H_{eff} \\ H_{eff} & 0 \end{pmatrix} \begin{pmatrix} M_x \\ M_y \end{pmatrix}, \quad (2)$$

where $M_x = m_x e^{i\omega t}$ and $M_y = m_y e^{i\omega t}$ are the x and y components of magnetization, respectively. Finding the eigenvalues of this equation gives us the following condition:

$$\omega = \gamma H_{eff}. \quad (3)$$

Equation 3 is the FMR condition for resonance. It can be shown that this equation is equivalent to the condition that $\omega = \omega_{rf}$, where ω_{rf} is the microwave frequency. Since the

microwave frequency is a known value, determining where resonance occurs provides important information about H_{eff} and thus about the internal magnetic fields inside the material.

In FMR measurements, a ferromagnetic sample is subject to an applied dc magnetic field (which is swept over a large range) and a constant microwave at a specific frequency. Angular dependence is taken by rotating the sample to vary the angle at which the field is applied to the material. Establishing at what field resonance occurs for numerous angles allows us to probe into the various internal fields within the material.

Our experimental system consists of a Bruker EMX EPR console, a WINEPR data acquisition program, 2 Helmholtz coils, a microwave bridge, and an EPR microwave cavity. The cavity is tuned by the console and data acquisition software to resonate with the 9.47 GHz microwave frequency, so that at the resonant frequency of the cavity, no microwaves are reflected back [5]. When the sample absorbs the microwave, the quality factor inside the cavity decreases. This briefly detunes the cavity, resulting in a microwave reflected back to the microwave bridge. This reflection is detected, and signifies a resonance. An illustration of the experimental setup is shown in Fig. 1 [4]. It is important to note that to improve the sensitivity in FMR, the derivative of the absorption peak is measured.

RESULTS AND ANALYSIS

Morphological Study

An SEM image of sample A is shown in Fig. 2. This image indicates that nanowires grown on (111B) GaAs grow perpendicular to the film. This figure also displays that the radius of the nanowires is the size of the Au droplet, seen on top of the nanowires. SEM images of samples B and C grown on (110) GaAs are shown in Fig. 3. From these images, we conclude that sample B has [111B] nanowires and sample C has both [111B] and [112] nanowires. These nanowires are at angles 55° and 32.9° from the film, respectively. It can also be noted that [111B] and [112] nanowires have distinct shapes. These differences in the nanowires indicate that the nanowire growth is strongly dependent on the crystal structure on which they are deposited.

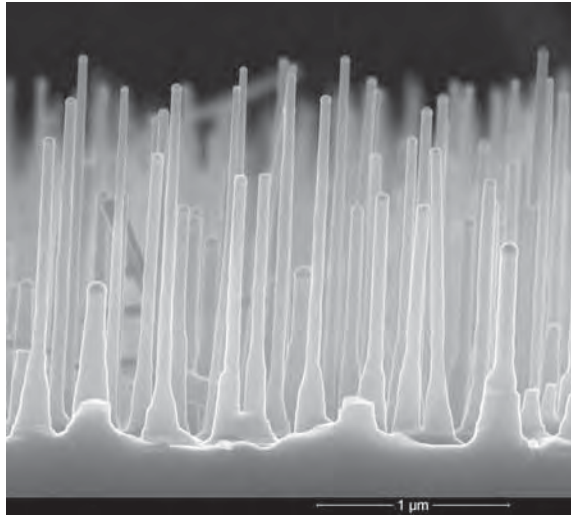


FIG. 2: SEM image of sample A, which is grown on a (111B) GaAs substrate.

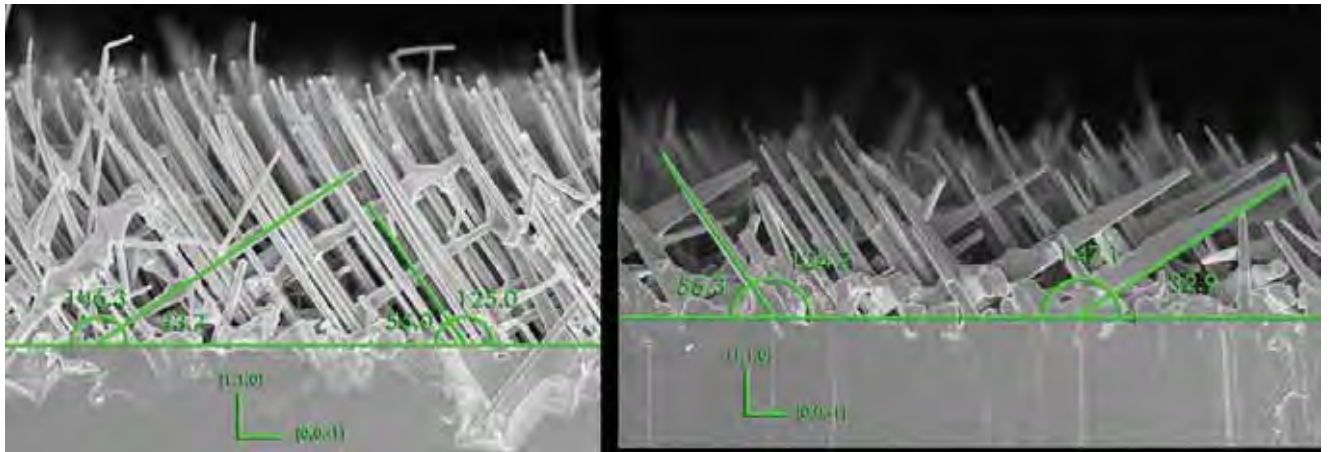


FIG. 3: On the left: SEM image of a cross section of sample B displayed with the associated angles of the nanowires and the crystal directions. This image also includes the angles of the rare anomalous wires, oriented along the [112] direction. On the right: Cross section SEM image of sample C shown with the corresponding nanowire angles and crystal directions.

FMR Results

All our measurements have H_{appl} range from 50G-12,000G except the out of plane measurement for sample B, where the field range is 50G-5,000G. Out of plane and in plane measurements were performed on sample A. From these results, individual resonance peaks are tracked and recorded. An illustration of this process is shown in Fig. 4. Here, 0° is normal to the substrate.

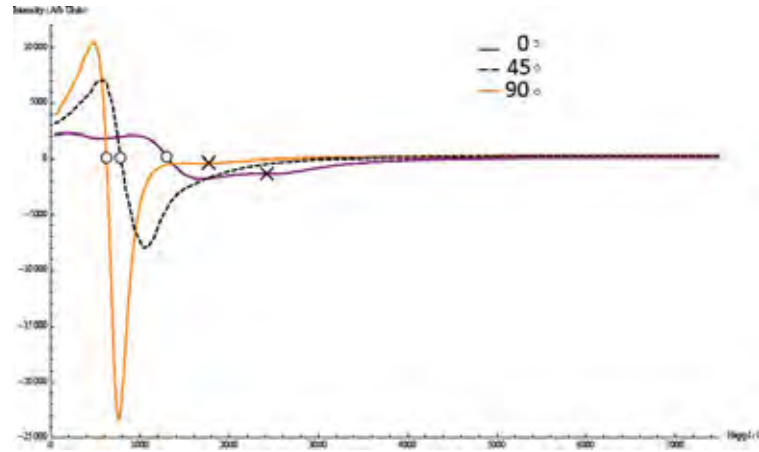


FIG. 4: An illustration of three FMR spectra taken at different angles, with their corresponding resonance peaks. Here, 0° is perpendicular to the film and 90° is parallel to the film. The unmarked peak around 400G at 0° is background.

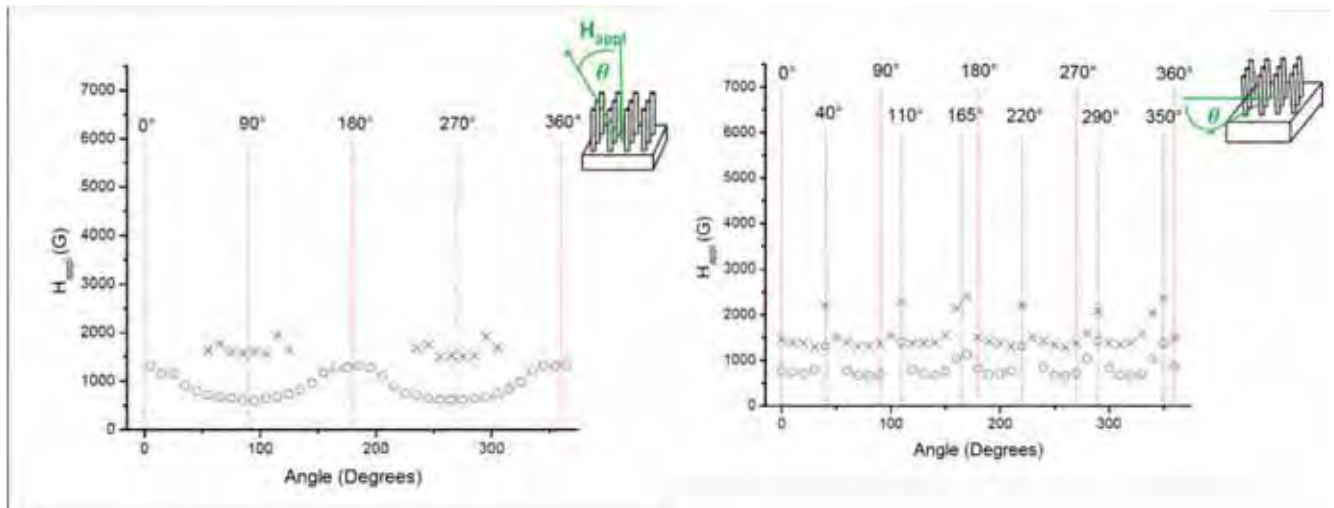


FIG. 5: Angular dependence of the resonance peaks for sample A. Each type of data point corresponds to a particular resonance peak, which is tracked as it moves with the angle. Left: angular dependence for the out of plane measurements. Right: angular dependence for the in plane measurements.

The in plane and out of plane angular dependence of the resonance peaks for sample A are shown in Fig. 5. The out of plane data displays two sets of peaks. Since the minimum occurs when we are in the plane of the thin film and the maximum when we are directly perpendicular to the film, we expect the lower set of data points for the out of plane measurement to correspond to the thin film. These minima and maxima correspond to the easy and hard axes of the film, respectively. The second set of peaks cannot be attributed to the nanowires since there is little signal along the nanowires. The absence of a nanowire

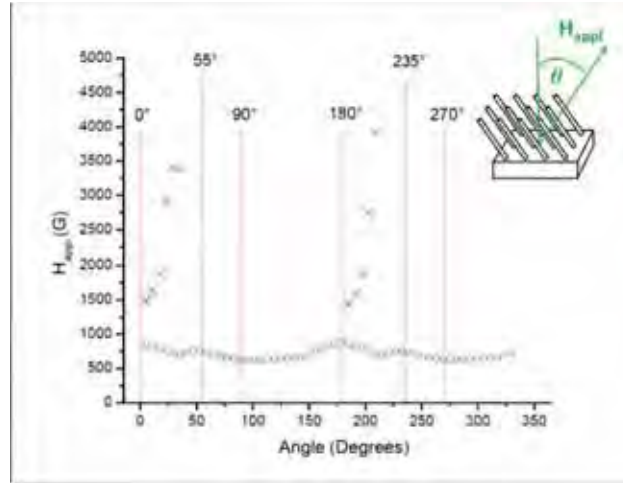


FIG. 6: Angular dependence of the resonance peaks for sample B. This graph displays signals from the thin film, and potential signals from the nanowires. It is important to note that 0° is with respect to the normal of the film.

signal can be interpreted as interference of the nanowire and film's easy/hard axes. That is, because the nanowires lie along the hard axis of the film and perpendicular to the nanowires corresponds to the easy axis of the film, it is highly plausible that the thin film signal covers up the nanowire signal. The in plane measurement displays an approximate 6-fold symmetry, which is in agreement with the 6-fold anisotropy of the Fe film grown on (111B) GaAs. The error in this graph can be attributed to error in rotating the sample inside the quartz tube.

A plot of the angular dependence for sample B is shown in Fig. 6. We see the expected FMR from the thin film, which occurs at maximum field for the orientation perpendicular to the film and minimum field in plane. However, we also see a series of peaks which seem to reach an asymptotic value around 55° from the normal. This degree is perpendicular to the nanowires. This suggests that this second FMR signal is from the nanowires, and that the asymptotic value of 55° corresponds with the hard axis of the nanowires. However, we need more data points in order to be certain that this signal is from the nanowires and not from the film.

Fig. 7 displays the full spectra of resonance lines and the angular dependence of the resonant peaks for the out of plane measurements of sample C. As can be seen from the figure on the right, we see a peak with a maximum at 55° and a minimum at 145° . This

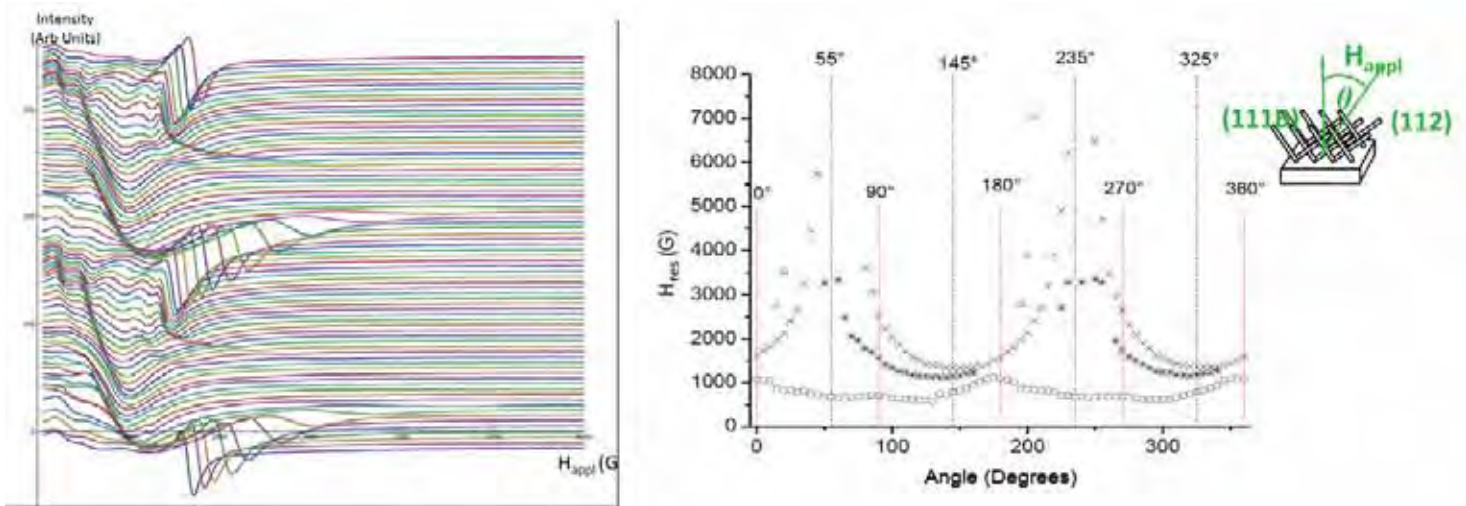


FIG. 7: On the left: EPR spectra at every angle for sample C, out of plane. Spectra are stacked upon each other, and the y values are scaled such that the maximum approximately corresponds with the angle the sample is rotated during measurement. The magnetic field is cut off at 6,000G to more clearly depict the features at lower H. On the right: Angular dependence of the resonance peaks for the out of plane measurements of sample C. A clear peak centers around the angle of the [111B] nanowire.

peak is not centered along the thin film hard or easy axis, which is a clear indication that we are seeing a peak due to the nanowires, not due to the thin film. Since the asymptotic value of this peak is at 55° (i.e. perpendicular to the [111B] nanowires), we conclude that the hard axis is radial to the nanowires. Similarly, since 145° is along the [111B] nanowires, it is evident that the easy axis and the preferred direction for magnetization is along the nanowires. Additionally, we note that the nanowire peak has uniaxial symmetry. It is not clear that we see a peak from the [112] nanowires. This could be due to the fact that this type of nanowire has a smaller signal, or that the [111B] and [112] nanowires are coupling, since they are approximately 90° apart.

CONCLUSIONS

We imaged multiple samples using Scanning Electron Microscopy (SEM) and performed Ferromagnetic Resonance (FMR) measurements on samples with varying morphologies. The in plane measurements for sample A showed a 6-fold symmetry present in the crystal. This

comparison was not exact; however, the error can easily be attributed to the error in sample rotation during the measurements. Although the out of plane measurements for sample A did not display isolated signals from the nanowire and the thin film due to signal interference, sample B exhibited part of a peak which centered around the nanowires, and sample C illustrated a full peak centered around the [111B] nanowires. The data from Sample C imply that the preferred direction of magnetization lies in the longitudinal direction along the nanowires, and the hard axis is radial.

There are many extensions of this research. The first and most obvious extension is to also take in plane measurements for sample C. Another extension would be to grow a nanowire sample that has a stronger Fe signal for the nanowire/film orientation than sample B. This would produce a plot with a clear signal from the nanowires, and would remove the complex geometry associated with sample C. In the future, my group plans to extend these studies to microresonances that are also seen in the data.

ACKNOWLEDGEMENTS

Support for this research comes from NSF grants. Special thanks goes to my research group, particularly to my professors and Rich Pimpinella, who spent many hours explaining to me the complexities of condensed matter physics.

* lsonderh@reed.edu

- [1] S. A. Wolf, D. D. Awschalom, R. A. Buhrman, J. M. Daughton, S. von Molnar, M. L. Roukes, A. Y. Chtchelkanova, and M. Treger, *Science* **294**, 1488, (2001).
- [2] T. H. Gerrits, H. A. M. van der Berg, J. Hohlfeld, L. Bar, and Th. Rasing, *Nature (London)* **418**, 509 (2002).
- [3] M. T. Björk, B. J. Ohlsson, T. Sass, A. I. Persson, C. Thelander, M. H. Magnusson, K. Deppert, L. R. Wallenberg, and L. Samuelson, *Appl. Phys. Lett.* **80**, 1058 (2002).
- [4] K. Tivakornsasithorn, PhD thesis, (2012).
- [5] R. Webers, J. Jiang, and D. Barr, “Bruker EMX User’s Manual”, (EPR Divison Bruker Instruments Inc., Billerica, MA, 1998)

CONSTRUCTING A SCANNING TUNNELING MICROSCOPE FOR
THE STUDY OF SUPERCONDUCTIVITY

CHRISTOPHER STEINER

2012 NSF/REU Program
Physics Department, University of Notre Dame

Advisors:
DR. MORTEN ESKILDSEN
CORNELIUS GRIGGS

CONTENTS

1. Abstract
2. Principles of Scanning Tunneling Microscopy
 - 2.1 General Scanning Tunneling Microscope Design
 - 2.2 Imaging Methods
 - 2.2.1 Topography
 - 2.2.2 Spectroscopy
3. The Inertial Piezo Drive
4. Assembly
 - 4.1 Coarse Approach
 - 4.2 Fine Approach and Scanning
5. Conclusion
6. References

1. ABSTRACT

Scanning tunneling microscopes (STMs) are one of the primary tools used in the study of superconductors. A microscope is being constructed which, although it will only be tested in air at room temperature, should in principle provide atomic resolution in vacuum at temperatures as low as 300mK and in magnetic fields as high as 9T. Parts have been machined from unconventional materials and assembled with high precision so that reliable coarse approach and the stability necessary to achieve atomic-resolution topographical images can be achieved. As of time of writing, the STM in question is still under construction. The coarse approach mechanism has been shown to be reliable, but the fine approach and scanning mechanism is yet to be tested.

2. PRINCIPLES OF SCANNING TUNNELING MICROSCOPY

2.1 General STM Design

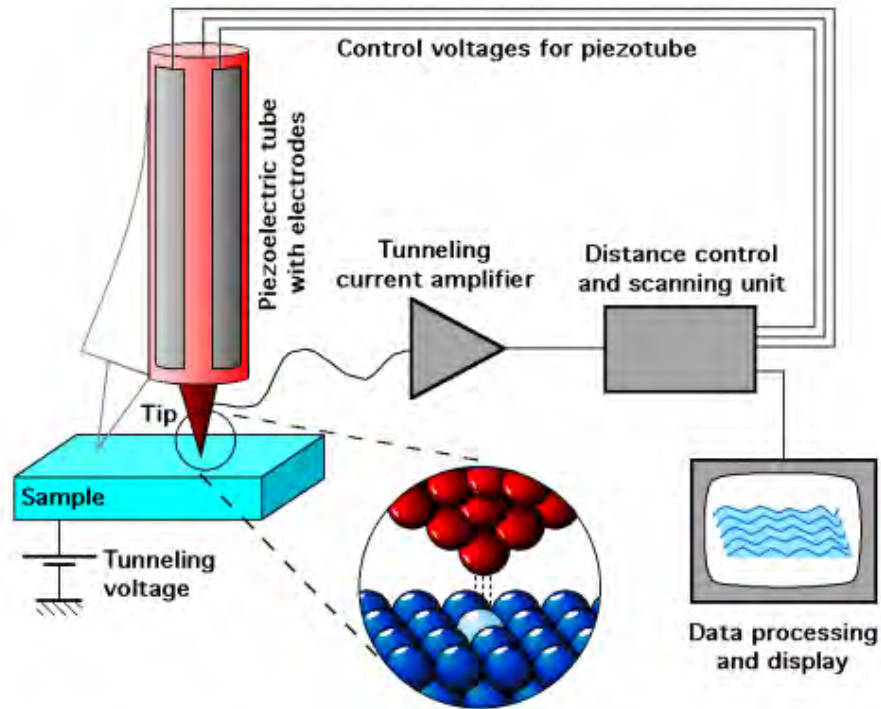


Figure 1: Diagram of an STM and control systems. Adapted from Michael Schmid, TU Wien. [1]

The key components of the STM are the atomically sharp tip, the piezoelectric tube scanner, and the sample. The tip is brought within angstroms of the sample, and a bias voltage between the tip and sample on the order of several-hundred millivolts applied. This allows electrons to tunnel from tip to sample (or sample to tip, depending on the bias voltage), and a feedback loop can be established to maintain a constant tunneling current by controlling the z-position of the piezo tube. The tip can then be scanned across the surface of the sample using the the piezo tube scanner, and the tunneling current measured via the transimpedance amplifier. This allows the user to collect data on the topography and electronic state of the sample at multiple locations.

2.2 Imaging Methods

2.2.1 Topography

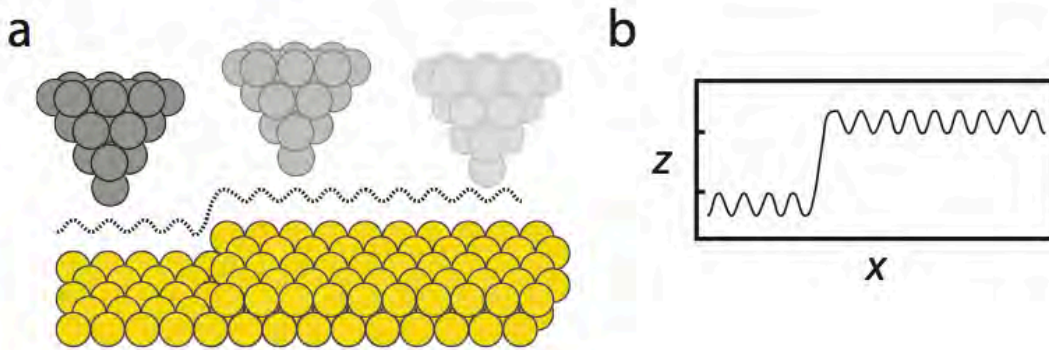


Figure 2: z-position is recorded as a function of x-position as the tip scans across the sample. Adapted from B. Drevniok [2].

Topography is the most common use of scanning tunneling microscopes. It allows the user to obtain an atomic-resolution image of the sample, in which the atomic lattice can be directly observed. A constant tunneling current is established as previously described, and then the tip is scanned across the surface. As the tip passes over atomic corrugations, the voltage controlling the z-position of the piezo tube must be adjusted to maintain a constant tunneling current (See Figure 2). By measuring z-voltage as a function of x-position, we obtain a series of line scans which can be combined into an image such as the one seen in Figure 3.

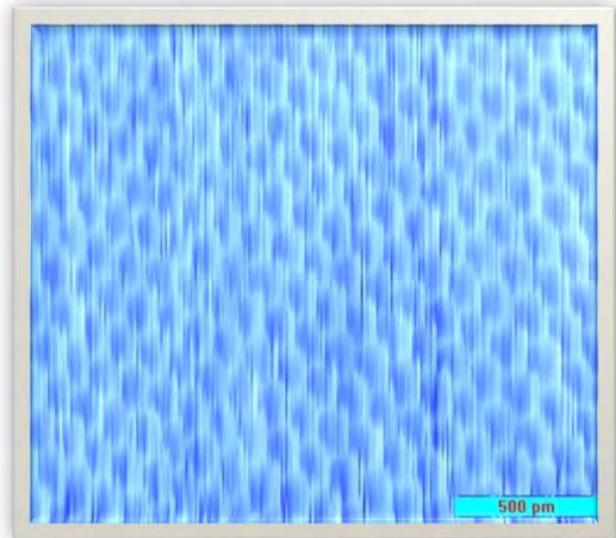


Figure 3: A topographical image of a graphite sheet produced by STM

2.2.2 Spectroscopy

Spectroscopy is used to study the density of electrons in a sample at a given energy. It is accomplished by achieving a tunneling current at a set bias voltage, and maintaining a constant z-position while varying the bias voltage. By measuring how the tunneling current changes with the varying voltage, we can construct a dI/dV curve, which represents the local density of states of the electrons in the sample [3]. Being able to measure these characteristics of a material is particularly relevant to the study of superconductors, the electrons in which exhibit a characteristic density of states. Figure 4 shows this characteristic density of states in superconducting NbSe_2 , which includes the energy gap and corresponding coherence peaks as observed through scanning tunneling spectroscopy.

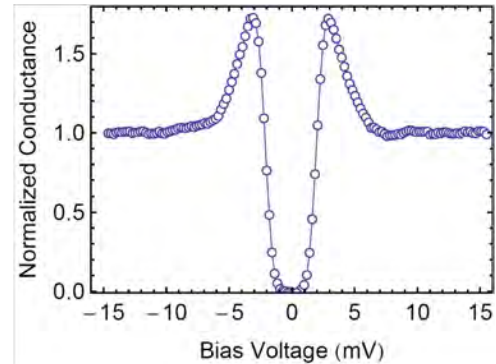


Figure 4: The superconducting spectrum of NbSe_2

3. THE INERTIAL PIEZO DRIVE

The differentiating factor in STM designs is the means by which coarse approach is handled.

Since the piezo tube has a range on the order of few micrometers, a secondary means of coarse motion is needed to move the tip close enough to the

sample that the piezo tube is within range, but

without crashing the tip into the sample. This is

accomplished using an inertial piezo drive. Shear

piezos (pictured in Figure 5) deform in the direction

of the chamfered corner when a positive voltage is applied to its surface. A sapphire prism

housing the tip and piezo tube scanner can be clamped between a series of these shear piezos,

and translated vertically by the intelligent application of voltage, as illustrated in figure 6.

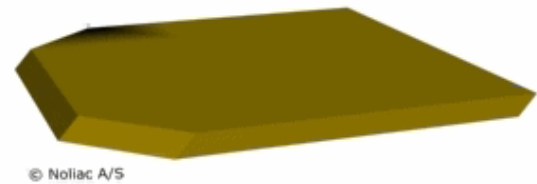
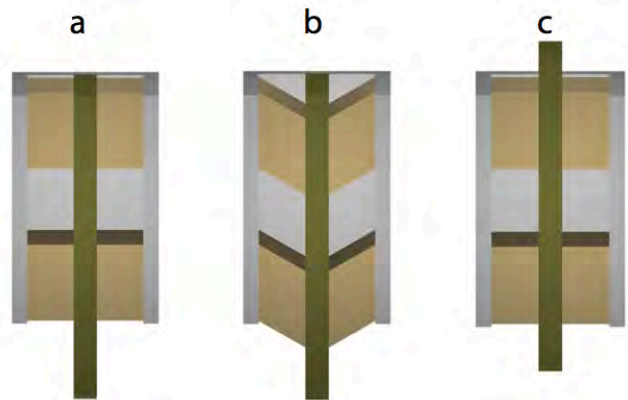


Figure 6: A Shear Piezo deforming away from its chamfered corner. [4]

Figure 6: A to B – Voltage is rapidly ramped across the shear piezos. The inertia of the rod causes the piezos to slip. B to C – the voltage across the piezos is slowly decreased, causing the rod to translate upwards without slipping. Adapted from Drevniok [2].



This allows the tip to be translated over a range of approximately 3mm, and since the shear

piezos deform approximately a micrometer at 200V [4], the step size can be made smaller than

the range of the piezo tube. This allows for a controlled approach of the sample, with minimal

risk of tip-sample collision.

4. ASSEMBLY

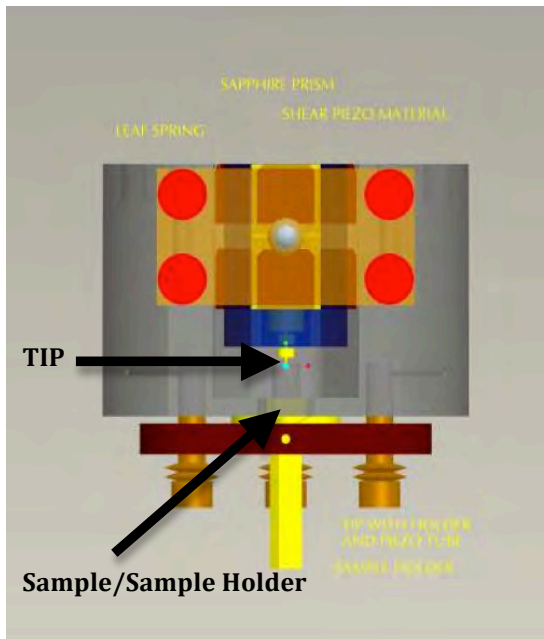


Figure 7: A front view of the STM design.

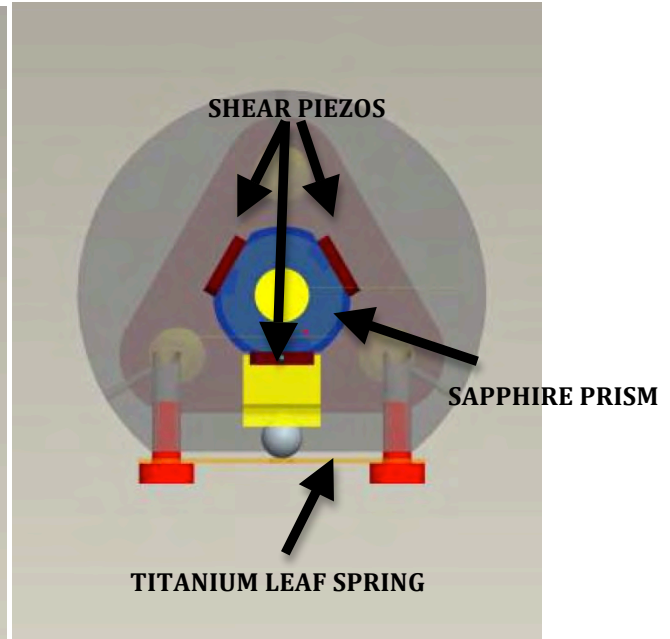


Figure 8: A top view of the STM Design

This STM is designed to function in ultra-high vacuum, at magnetic field as high as 9T, and at temperatures as low as 300mK. To cope with the challenges posed by these conditions, much of the STM has to be manufactured from novel materials. The body of the STM and other components which must be electrically insulating are machined from MACOR, a glass ceramic which behaves well under ultra high vacuum and has low thermal expansion coefficients. Other components, such as the leaf-spring assembly, are machined from titanium, which matches the thermal expansion characteristics of MACOR.

4.1 Coarse Approach

This STM design uses the same general principle as the inertial piezo drive described above, but each piezo stack is composed of two shear piezos in order to maximize the displacement achieved by each cycle of the piezo motor controller. This adds another degree of

complexity to the assembly. A voltage must be applied between the two piezos in each stack, while grounding the top and bottom. This is accomplished by assembling the piezo stacks in the following order (from bottom up):

- 1) A grounded copper electrode shared between two stacks
- 2) Shear Piezo
- 3) Copper electrode to which voltage will be applied
- 4) Shear piezo rotated 180°
- 5) Grounded copper electrode
- 6) Sapphire Plate



Figure 9: Fully assembled stack mounted to leaf spring apparatus

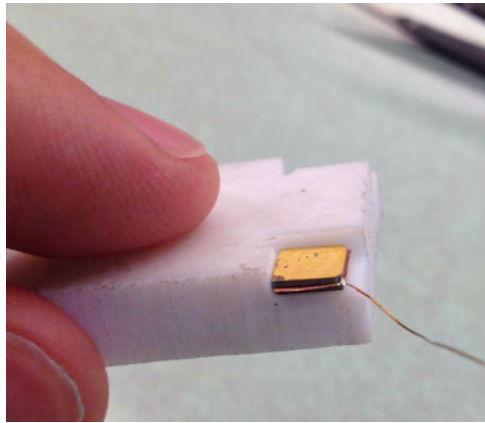


Figure 10: A partially assembled piezo stack



Figure 11: Fully assembled piezo stacks mounted and wired to STM body

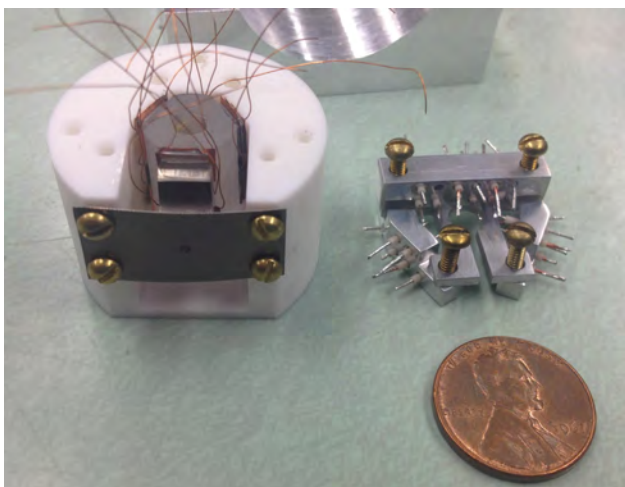


Figure 12: Partially assembled coarse approach

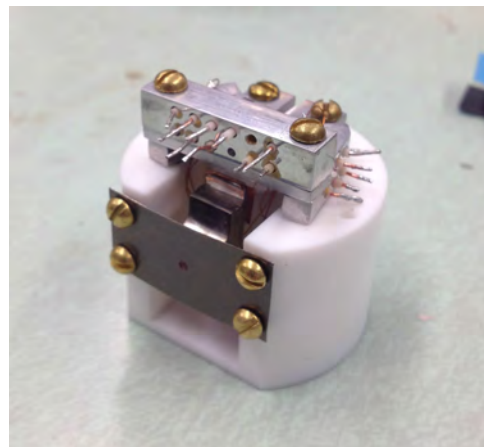


Figure 13: Fully assembled and wired coarse approach

Once the prism is in place, all piezo stacks are installed, and all electrical connections are confirmed to be reliable, the STM can be connected to the piezo motor controller. The controller will apply the proper voltages in the necessary pattern to operate the coarse approach system. Achieving reliable coarse approach can require significant amounts of trial and error. Finding the correct motor control settings and proper tightness of the titanium leaf spring is a non-trivial task. It has been discovered that the particular piezo motor controller being used for this setup may not have the power supply necessary to drive all 12 shear piezos. When the voltage was only applied across the top piezos of each stack, reliable coarse approach was achieved at 250V.

4.2 Fine Approach and Scanning

The fine approach and scanning mechanism in this STM design is accomplished by a piezoelectric tube scanner as described in previous sections. A MACOR bushing is glued inside of the piezo tube to attach the tip-holder to the piezo tube, and the piezo tube is glued to a MACOR bushing to attach the tube scanner to the sapphire prism. As of



Figure 14: Piezoelectric tube scanner and associated MACOR bushings

writing, this portion of the STM has not yet been tested. Due to the relatively small number of components, it is expected to behave as designed without issue.

5. CONCLUSION

An inertial piezo drive has been constructed to translate a sapphire prism containing the fine approach and scanning mechanism of a scanning tunneling microscope. Up to this point, non-permanent adhesives have been used in the construction. In the coming weeks, it will be demonstrated that this STM design can achieve an atomic-resolution topographical image. At this point, the STM will be dismantled and then reassembled using permanent epoxies.

6. REFERENCES

- [1] Schmid, Michael. "The Scanning Tunneling Microscope." *The IAP/TU Wien STM Gallery*. Institut für Angewandte Physik. <http://www.iap.tuwien.ac.at/www/surface/stm_gallery/stm_schematic>.
- [2] Drevniok, Benedict. *A Vertical Coarse Approach Scanning Tunneling Microscope*. MSc Thesis. Queen's University, Ontario. 2009.
- [3] Kuk, Young. "Metal Surfaces." 1993. *Scanning Tunneling Microscopy*. Ed. Joseph A. Stroscio and William J. Kaiser. Boston: Academic Press, INC, 1993. 277-305. Print. Vol. 27 of *Methods of Experimental Physics*.
- [4] *Shear Plate Actuators*. Noliac, n.d. Web. 02 Aug. 2012. <http://www.noliac.com/Shear_plate_actuators-7714.aspx>.

GALAXY OUTFLOW AND FILAMENTARY INTERACTION

Annie Stephenson

2012 NSF/REU Program
Physics Department, University of Notre Dame

Advisor: Professor Arielle Phillips

ABSTRACT

The modeling of interactions between galaxies in filamentary structures often sacrifices resolution and detail in order to efficiently represent the large-scale structure of filaments. This can cause large margins of error in model data. Techniques to better represent galaxies on a small scale, while still maximizing computer efficiency are extremely valuable to the accurate representation of filamentary structure and interaction between galaxies and filaments. Through coding methods that reduce the complexity of physical phenomena as described in small-scale models, a more accurate yet memory-efficient model is achieved. Analysis of collimated galaxy outflow and spherical galaxy outflow interactions with filamentary environment and galaxy gravitational force reveals varying projected gas particle location over time. Variations in column angle and initial velocity of gas outflows also reveal differences in projected gas particle location. This simulation calculates particle position based on forces acting on the particle through time-steps that can be changed based on the users desire to examine long-term motion or short-term motion. These models provide a basis for a new generation of large-scale models that provide more accurate information about filament-galaxy interaction.

I. INTRODUCTION

Recent observations reveal galaxies as having collimated outflows, where outflow velocity is inversely proportional to size of column angle of outflows. These collimated outflows indicate that enriched material will be dispersed in specific directions rather than in all directions as is modeled in large-scale simulations. This preferential direction of outflows can cause a great variance in how enriched material is distributed in filaments.

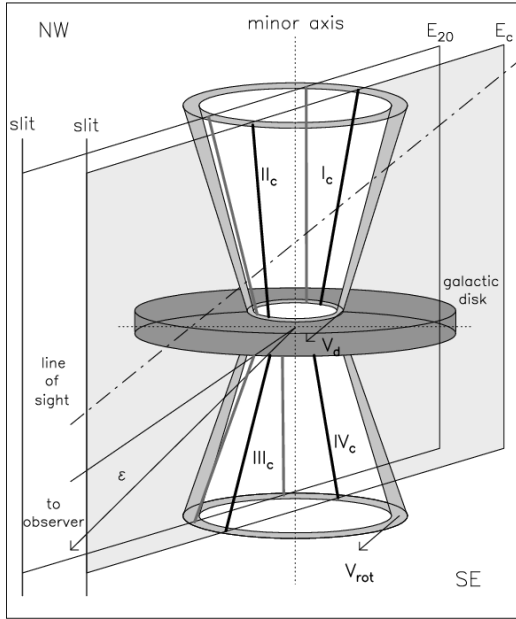


Fig 1: This figure illustrates the collimation of outflows as they are expelled from a disk galaxy.¹

The implementation of models that consider collimated outflow and preferential orientation could heavily influence models of the flow of enriched material. However, simplified methods of modeling this collimated outflow must first be created so that they can be efficiently integrated into the large-scale models.

II. SIMULATION MODEL

Large-scale models of filamentary structure often oversimplify the interactions between galaxies and the filament environment because galaxies are so miniscule in comparison to large cosmic structures. This model examines galaxy outflow by considering the outflowing gas to be an assortment of discrete elements, in effect particles. This method holds many of the fundamental characteristics of smoothed-particle hydrodynamics. These gas particles are modeled with a given reasonable mass and radius and initial velocity as they are expelled from the galaxy.

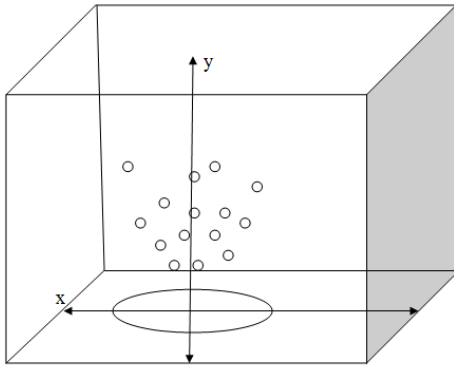


Fig 2: A simplified representation of the computer simulation to track gas particles as they exit a galaxy. We see the particles moving out from the galaxy. In this figure, the time evolutions are layered over one another, displaying the same particle at different times in order to show the path along which it has traveled.

III. CONSIDERED COMPONENTS OF FORCE

While numerous forces act on the gas particle, generalizations must be made in order to maximize computer efficiency for the purpose of using these models for future large-scale models in which an over-detailed analysis of galaxy behavior can utilize more computer memory than is practical and can interfere with other components of the program, causing large margins of error in the data. Hydrocode is known to be lengthy and complex and often must be turned off for portions of the runtime because it can interfere with parts of the code. Hydrocode is also very different in large and small scale models. To remedy this inconsistency, a simplification was made to mimic the basic functions of hydrodynamics. In its place, a drag force was implemented to incorporate the deceleration of the particles as they entered the filament without the complexities and memory use of hydrocode. In addition, the gravitational force of the galaxy on the gas particles was considered.

IV. COLLIMATION VERSUS SPHERICAL DISPERSION AND INITIAL VELOCITY VARIANCE

Parameters of the code that can be modified each runtime are angle of ejection, initial velocity, galaxy mass, and particle mass. Small changes in angle of ejection for the different particles represent a more collimated jet, whereas a large angle boundary represents a more spherical dispersion of particles. Increases in mass increase gravitational force, causing the particles to decelerate more rapidly and in some cases fall back down to the galaxy. Increases in initial velocity cause drag to be higher, but the particles are more likely to travel further. Different particle resolutions are can be used in the program to highlight different aspects of the data. A lower particle count provides easy viewing of individual particles, whereas a high particle count can help reveal data trends.

V. RESULTS AND DISCUSSION

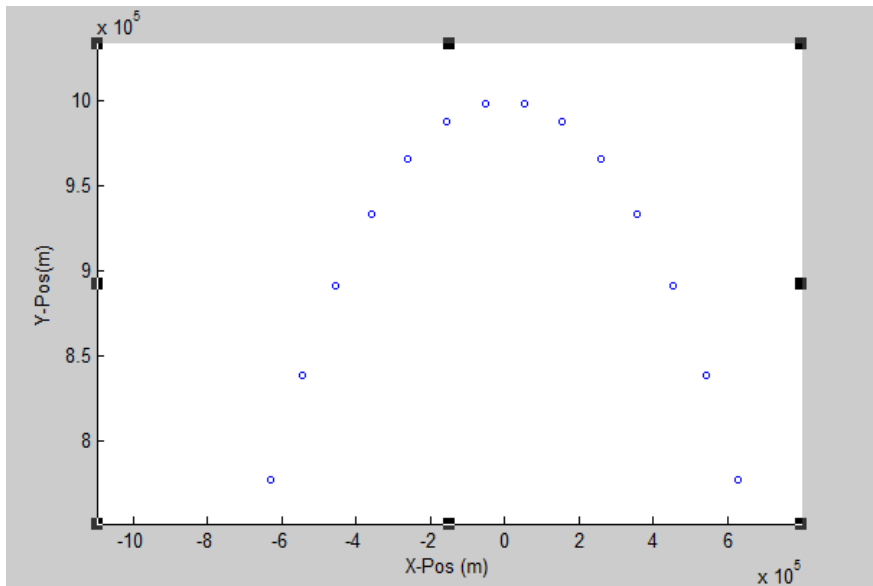


Fig. 3: This graph shows a relatively smooth curve representing one time-step of the particles emitted from a galaxy. The smoothness is due to a constant density distribution assumed within the filament and galaxy. The parabolic shape is due to the drag force being considerably larger than the gravitational force. $V_0=1000\text{km/s}$.

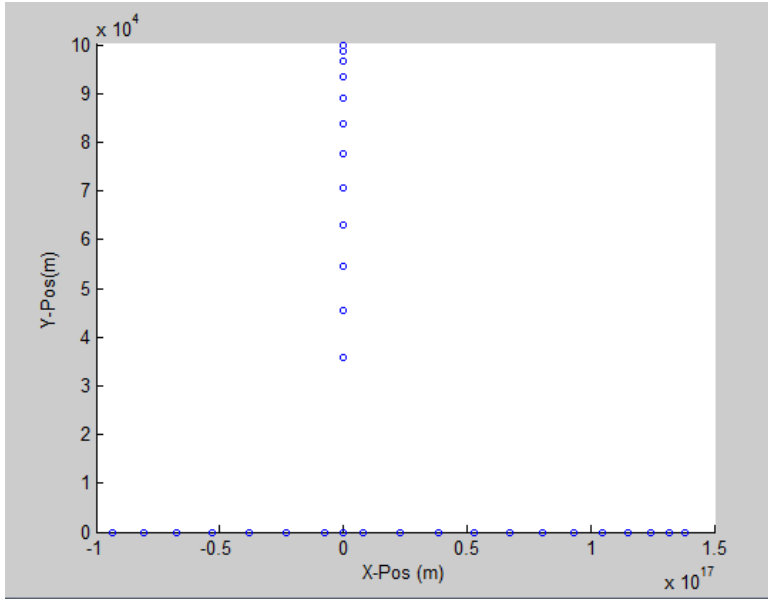


Fig. 4: This plot shows particles from outflows with $V_0=100\text{km/s}$. Because the velocity is much smaller, the particles do not travel as far, so the gravitational force decreases at a lower rate and eventually the gravitational force overcomes the drag force and some of the particles are pulled back down to the galaxy.

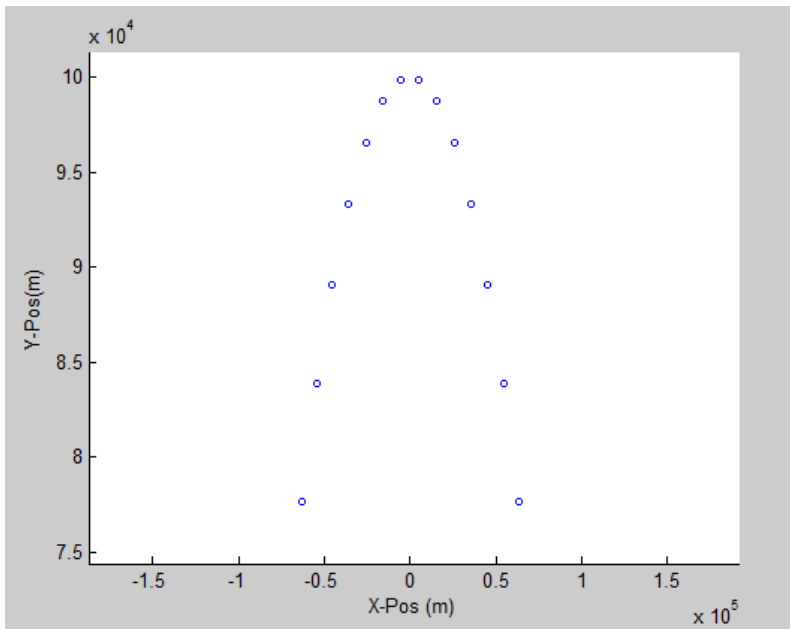


Fig. 5: A zoomed in view of figure 4. As you can see, the particles that appear to be in a straight line in fig. 4 really form a parabola due to the different angles at which they are ejected.

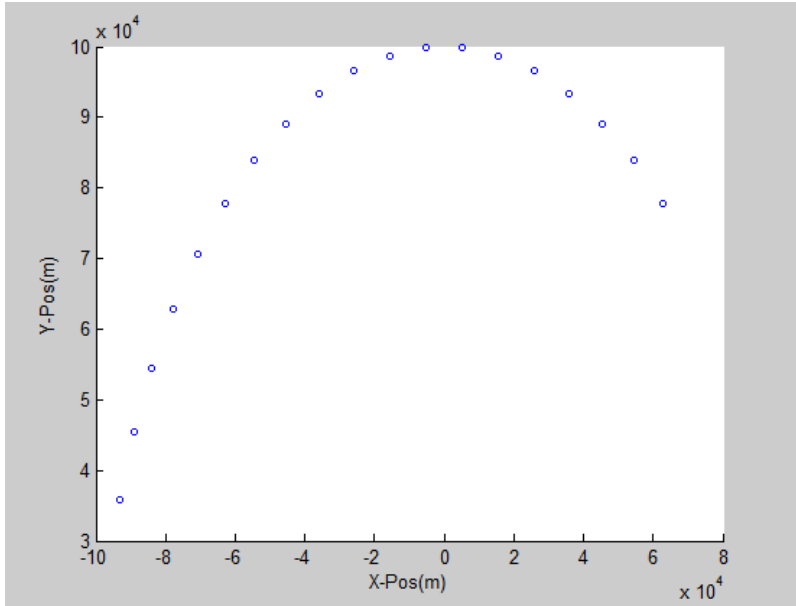


Fig. 6: Early time-step of figure 4. None of the particles have fallen back to the galaxy yet. There is a clear parabolic pattern. Note the tight zoom on the x-axis.

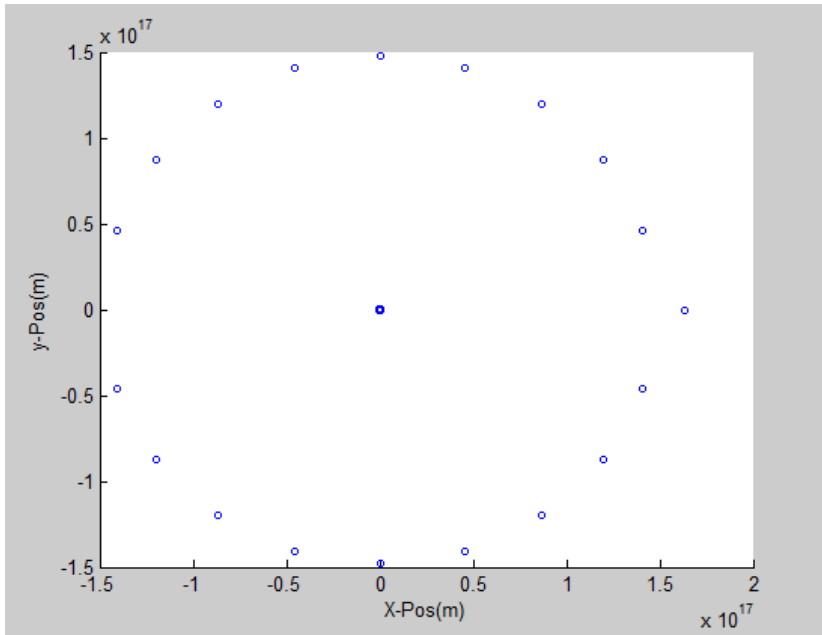


Fig. 7: In this plot, V_0 of the particles is 100km/s, and the angles vary by increments that eventually compose an entire circle. We see that there are some particles that have fallen back to the galaxy (which is located at 0,0 but is not pictorially represented on graph)

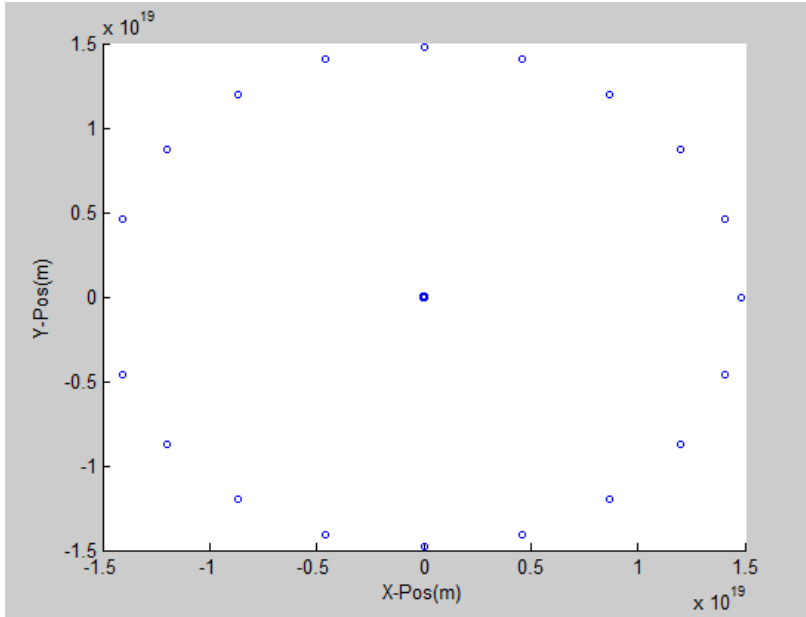


Fig. 8: In this plot, V_0 of the particles 1000km/s. The shape is similar to that of figure 7 because the angle constrictions are the same. However, the particles are further from the galaxy due to their higher initial velocity.

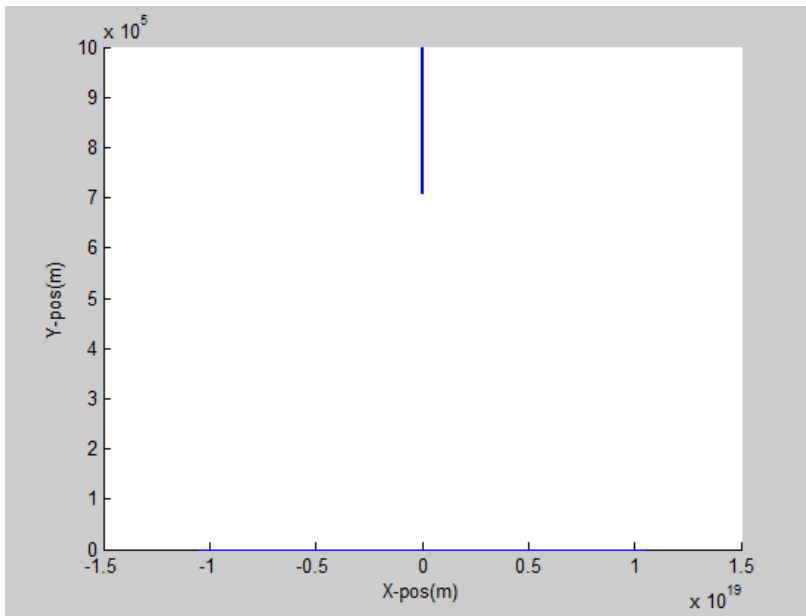


Fig 9: Here, particles from outflows of $V_0 = 100 \text{ km/s}$ are shown, as in Fig. 4. This plot, however, has a much higher resolution, 1000 particles as opposed to 20.

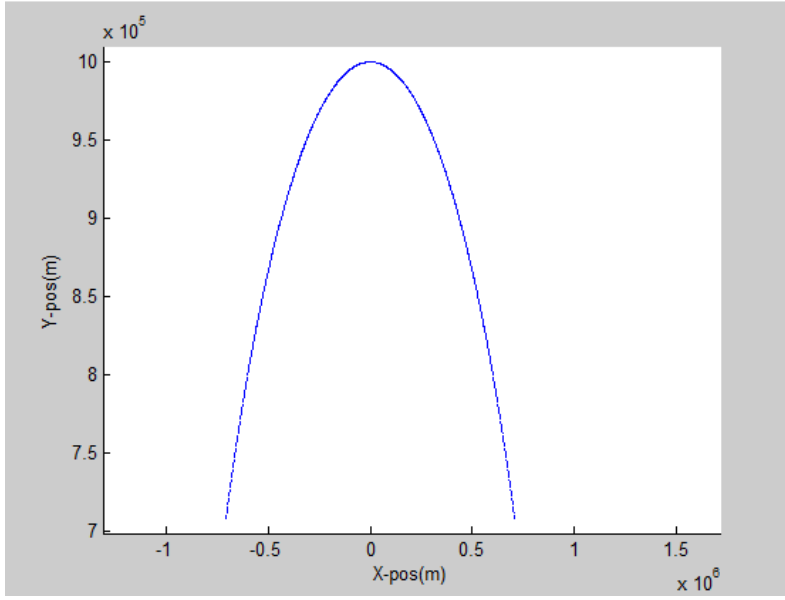


Fig. 10: A zoomed in version of Fig 9. Essentially the same plot as Fig 5, but with 1000 particle resolution as opposed to 20.

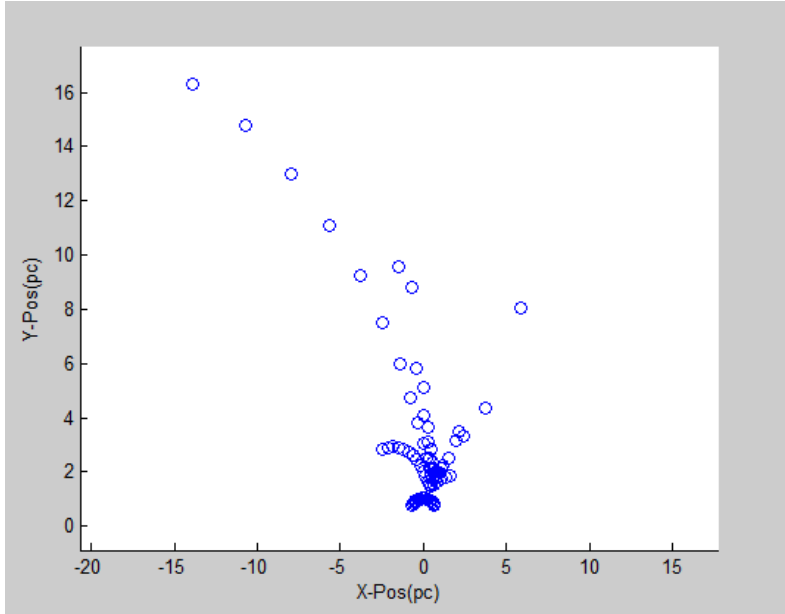


Fig 11: A plot after several code adjustments. These units are on a much larger scale (e.g. parsecs vs. kilometers). Also, 1000 year time steps are used as opposed to one second time steps. This graph shows a much larger time span, and very different particle trends.

This code successfully tracks particle movements in time. Certain changes in the parameters of the code cause the expected responses. Variation in angle of ejection for the different particles can vary amount of collimation of the jet, and a large angle boundary represents a more spherical dispersion of particles. Increases in initial velocity cause drag to be higher, but the particles are more likely to travel further over time, therefore lowering the gravitational force and allowing them to travel even further.

VI. ACKNOWLEDGEMENTS

Dr. Lara Arielle Phillips was instrumental in the completion of this research experience. As my advisor, she provided direction and guidance when needed. Ali Snedden, a graduate student under Dr. Phillips, also gave me counsel throughout my research. Dr. Umesh Garg, the University of Notre Dame REU coordinator was also extremely supportive throughout the summer, and my research experience would not have been possible without him. I would also like to express my gratitude to Heather Christensen, whose organization, help, and kindness helped make my research experience run smoothly.

VII. REFERENCES

1. Greve, A. 2004, A&A, 416,1
2. Martin, C.L., Shapley, A. E., Coil, A.L., Kornei, K.A., Bundy,K., Weiner, B.J., Noeske, K.G., & Schiminovich, D. 2012, arXiv:1206.5552v2